

# Emergent conformational and dynamical properties in active filamentous systems

INAUGURAL-DISSERTATION

zur

Erlangung des Doktorgrades  
der Mathematisch-Naturwissenschaftlichen Fakultät  
der Universität zu Köln



vorgelegt von

**Aitor Martin-Gomez**  
aus Barcelona, Spain

Köln 2020



Berichterstatter:           1. Prof. Dr. Gerhard Gompper  
                                  2. Prof. Dr. Andreas Schadschneider

Tag der letzten mündlichen Prüfung: **30. Juni 2020**



# Abstract

Active matter provides a wide spectrum of non-equilibrium emerging phenomena. In nature, active agents endure a vast number of propulsion mechanisms to generate directed motion. Examples range from the cytoskeleton, where actin filaments and microtubules are driven by molecular motors, or ATP-dependent enzymatic processes altering the dynamics of the cytoplasm, to kinesin motors going through microtubules, which generate nonequilibrium forces that affect the dynamics of the cytoskeleton, the transport, and the organization in the cell interior.

Following the physical nature of active elongated systems, we drive our investigations into the properties of active filamentous, polymer-like system in which activity is taken into account by independent site velocities, with orientations changing in a diffusive manner, and not tangential to the polymer contour. The intimate coupling of thermal and active noise, shear stress, hydrodynamic interactions, and polymer conformations implies the emergence of novel structural and dynamical features. First, we study analytically the conformational and rheological properties of active filaments/polymers exposed to shear flow. Using the continuous Gaussian semiflexible polymer model extended by the activity, yields a shear-induced deformation, alignment, and shear thinning behavior, similarly to the passive counterpart. Independent of stiffness, activity facilitates the swelling of polymers, and enhances alignment and shear thinning.

Next, we analyze the influence of hydrodynamic interactions (HI) on the properties of polymers and filaments exposed to activity. Activity is taken into account by independent site velocities, with orientations changing in a diffusive manner. We investigate the conformational and dynamical properties of active self-propelled filaments/polymers in solution by using Brownian dynamics simulations and analytical theory. At moderate activities, HI lead to a substantial shrinkage of semiflexible polymers; even flexible HI-polymers shrink, while active free-draining polymers swell monotonically. For large activities, flexible and semiflexible polymers undergo a reswelling. The polymer mean square displacement is enhanced, and an activity-determined ballistic regime appears. Similarly, we explore polymers in solution in the presence of external active noise. Now, the same description of the system is used, however, a

---

coupling between the activity and hydrodynamics in the equations of motion has been taken into account. That way, we can depict the activity as a correlated noise from the environment, which we describe by the colored noise, instead of being an intrinsic property of the polymers. In this case, HI lead to an enhanced swelling of flexible polymers with increasing activity, even for moderate values, differing substantially from the conformational properties of self-propelled polymers in presence (and absence) of HI.

To conclude, we introduce a particle-based mesoscale hydrodynamics simulation technique for both cases; polymers in presence of external active noise and self-propelled polymer. After comparing the new conformational properties with the Brownian dynamics simulations, we find quantitative and qualitative agreement. Attractively, the MPC method can allow the application of more complex geometries for active objects in confinement, in contrast to the hydrodynamic tensor approach simulations .

## Kurzzusammenfassung

Aktive Materie weist ein weites Spektrum an Nichtgleichgewichts-Phänomenen auf. In der Natur findet man eine Fülle solcher aktiven Systeme, die durch verschiedenste Fortbewegungsmechanismen gerichtete Bewegung erzeugen können. In den hier betrachteten Längenskalen reichen Beispiele aktiver Materie von Zytoskelett, wo Actinfilamente und Mikrotubuli von molekularen Motoren bewegt werden bis hin zu ATP-getriebenen, enzymatischen Prozessen, die die Dynamik des Cytoplasmas bestimmen.

Im Rahmen dieser Forschungsarbeit fokussieren wir uns auf die Eigenschaften von aktiven, filamentartigen, polymer-ähnlichen Systemen. Dabei wird, anders als bei tangential, entlang der Kontur getriebenen Filamenten, die Aktivität durch unabhängige Geschwindigkeiten entlang der Kontur des Filaments beschrieben, deren Orientierungsvektoren sich wie bei einem diffusiven Prozess verhalten. Die Kopplung von thermischen Fluktuationen mit der Aktivität, der Einfluss von Scherströmungen und hydrodynamischen Wechselwirkungen zeigen neue strukturelle und dynamische Eigenschaften auf.

Im ersten Teil beschreiben wir mittels analytischer Berechnungen die strukturellen und reologischen Eigenschaften von aktiven, semiflexiblen Filamenten unter dem Einfluss von Scherströmungen. Dabei verwenden wir das, um die Aktivität erweiterte, kontinuierliche Gauß'sche Polymermodell und zeigen dessen Scherungs-induzierte Deformation, Ausrichtung und Verdünnung. Unabhängig von der Steifheit des Polymers, steigert die Aktivität, im Vergleich zum passiven Polymer, dessen Schwellung, Auslenkung und Verdünnung.

Des Weiteren untersuchen wir die strukturellen und dynamischen Eigenschaften von aktiven, selbstgetriebenen Filamenten in Lösungen mittels Brownian Dynamics Simulations und mit Hilfe von analytischen Berechnungen. Bei moderater Aktivität des Systems führen die hydrodynamischen Wechselwirkungen zu einer signifikanten Schrumpfung der semiflexiblen Filamente; auch flexible Filamente schrumpfen mit zunehmender Aktivität, während sie ohne Einfluss von hydrodynamischen Wechselwirkungen monoton anschwellen. Bei sehr starker Aktivität schwellen die semiflexiblen und flexiblen Filamente auch unter Einfluss der Hydrodynamik wieder an. Die mittlere quadratische Verschiebung vergrößert sich mit zunehmender Aktivität und ein ballistisches Regime tritt ein.

---

Ähnlich zu den selbstgetriebenen Filamenten, untersuchen wir auch extern getriebene Filamente in Lösungen. Dabei tritt eine Kopplung der Hydrodynamik und der Aktivität auf. Dies wiederum führt zu einer stark gesteigerten Schwellung der flexiblen Filamente und das auch unter dem Einfluss von bloß moderater Aktivität. Dieses Verhalten unterscheidet sich substantziell vom Verhalten von selbstgetriebenen Filamenten sowohl in Lösungen, als auch ohne hydrodynamische Wechselwirkungen.

Wir stellen auch eine neue, Teilchen-basierte Mesoskalen-Hydrodynamik-Simulation für beide Fälle vor. Der Vergleich mit Brownian Dynamics Simulationen zeigt eine gute qualitative als auch quantitative Übereinstimmung. Ein großer Vorteil dieser neuen Methode, die auf MPC basiert, ist, dass sich damit sehr leicht die Untersuchung der oben vorgestellten Systeme auf eine größere Anzahl an Polymeren und komplexeren Geometrien hoch-skalieren lässt.

# Contents

<b>Introduction</b>	<b>13</b>
0.1 Active Matter . . . . .	13
0.1.1 Bacteria and bio-polymers . . . . .	15
0.1.2 Assembly of active colloids . . . . .	15
0.2 Hydrodynamics in active filamentous systems . . . . .	17
0.3 Summary . . . . .	18
<b>1 Theoretical background</b>	<b>21</b>
1.1 Stochastic dynamics . . . . .	21
1.1.1 Langevin dynamics . . . . .	21
1.1.2 Ornstein-Uhlenbeck process . . . . .	22
1.1.3 Fokker-Planck equation . . . . .	23
1.1.4 Itô calculus . . . . .	25
1.2 Hydrodynamics . . . . .	27
1.2.1 Navier-Stokes equations . . . . .	27
1.2.2 Hydrodynamic interactions . . . . .	29
1.2.3 Equations of motion of particles in fluid . . . . .	30
1.3 Simulations of systems with HI . . . . .	31
1.3.1 Ermak-McCammon scheme . . . . .	31
1.3.2 Multiparticle collision dynamics (MPC) . . . . .	32
1.4 Active systems . . . . .	35
1.4.1 Active Brownian particle (ABP) . . . . .	35
1.4.2 Active Brownian polymer (ABPO) . . . . .	37
1.4.3 Continuous gaussian active semiflexible polymer (GASFP) . . . . .	39
<b>2 Active polymer under shear flow</b>	<b>45</b>
2.1 Model . . . . .	45
2.1.1 Equation of motion . . . . .	45
2.1.2 Eigenfunction expansion . . . . .	47
2.1.3 Mode-amplitude correlation functions . . . . .	48
2.1.4 Inextensibility and stretching coefficient $\lambda$ . . . . .	49

## Contents

---

2.2	Dynamics and conformations . . . . .	52
2.2.1	Relaxation times . . . . .	52
2.2.2	Radius of gyration . . . . .	54
2.2.3	Alignment . . . . .	55
2.3	Rheology: Viscosity . . . . .	57
2.4	Discussion . . . . .	59
<b>3</b>	<b>Active Brownian polymer with hydrodynamic interactions</b>	<b>61</b>
3.1	Computer simulations . . . . .	62
3.1.1	Model: Equation of motion . . . . .	62
3.1.2	Conformations . . . . .	63
3.1.3	Dynamical properties . . . . .	65
3.2	Analytical model of active Brownian polymer in solution . . . . .	66
3.2.1	Equations of motion . . . . .	66
3.2.2	Solution of the equations of motion . . . . .	68
3.2.3	Stretching coefficient and relaxation times . . . . .	73
3.2.4	Conformational properties . . . . .	75
3.2.5	Dynamical properties . . . . .	78
3.3	Conclusions and discussion . . . . .	82
<b>4</b>	<b>Characteristics of active polymers in solution by external colored noise</b>	<b>85</b>
4.1	Computer simulations . . . . .	86
4.1.1	Model of active polymer . . . . .	86
4.1.2	Brownian dynamics with the RPY tensor . . . . .	86
4.1.3	Active polymer in MPC fluid . . . . .	87
4.2	Computer simulations: Results . . . . .	90
4.2.1	Conformational properties . . . . .	90
4.2.2	Dynamical properties . . . . .	92
4.3	Analytical approach . . . . .	93
4.3.1	Model and equations of motion . . . . .	94
4.3.2	Solution of the equations of motion . . . . .	95
4.3.3	Conformational properties . . . . .	103
4.4	Dynamical properties . . . . .	106
<b>5</b>	<b>Multiparticle collision dynamics approach with self-propelled polymers</b>	<b>111</b>
5.1	Self-propelled monomer in MPC fluid . . . . .	111
5.2	Fluid-polymer coupling . . . . .	112
5.3	Results: Comparison RPY with MPC . . . . .	113

6	Conclusions and outlook	115
	Appendix A Intermolecular distance	119
	Appendix B Mode-number dependence of Ossen tensor	121
	Appendix C Relaxation times	123
	Appendix D Asymptotic stretching coefficient	125
	Bibliography	127



# Introduction

Over the last decades, soft condensed matter physics has become a rapidly expanding branch of science and has attracted considerable interest from the biology, biophysics, and chemistry community. Its importance in the research and industry fields has exponentially increased, always promoted by the rampant development of experimental techniques. These state-of-the-art techniques are especially designed to provide a vast description of biological systems by exploring properties at smaller length and time scale, which ultimately offer a wide range of technological applications, from nanotechnology to health science, e.g., medicine, pharmacology, biotechnology.

The investigation of the properties of soft materials has brought the invention of new tools, as well as the improvement of optical microscopy, light scattering, and rheology techniques. Colloidal aggregates, emulsions, drops/droplets, polymer melts or microgels fit into the category of such materials. A major focus is on the mechanical properties and their relationship to the internal dynamics of the structures within the materials. The complexity of the studied systems has also favored the development of the theoretical and numerical methods applied, which became more demanding and sophisticated. In addition, the search for new ways to create materials with more attractive and exotic properties and high technological value is always concomitant.

In particular, activity and self-driven motion are paramount in living and artificial systems. This has motivated the new field of active matter in the last years, focusing on the physical features of propelled mechanisms and on the emergent behavior in a collective of a large number of identical active agents. Similar to biological microswimmers, various autonomous synthetic machines in the nano- and microscale have been also designed. Such agents provide the basis for multifunctional, highly responsive, intelligent (artificial) active materials, which manifest emergent behavior and the ability to perform tasks in response to external stimuli.

## 0.1 Active Matter

Active matter is a fascinating and relatively new field in soft matter physics. The perpetual conversion of either internal chemical energy, or pump energy from the

## Contents

---

environment, to generate directed motion is the key feature of active matter [1, 2]. Its associated out-of-equilibrium nature is the origin of intriguing emerging structural and dynamical properties. This field aims to understand how macroscopic properties of interacting particles emerge from properties of the constituent particles as well as their interactions. In presence of interaction, this ability to self-propel leads to fascinating collective phenomena such as activity-driven phase separation or large-scale collective motion [1–11], which are absent in their passive counterparts but largely observed in populations of active particles (both in living and man-made systems) across a broad range of scales: from vertebrates, e.g., flock of birds, school of fish (see Fig.1(a)) or human herds, down to motile bacteria (see Fig.1(b)) or intracellular filaments driven by molecular motors.

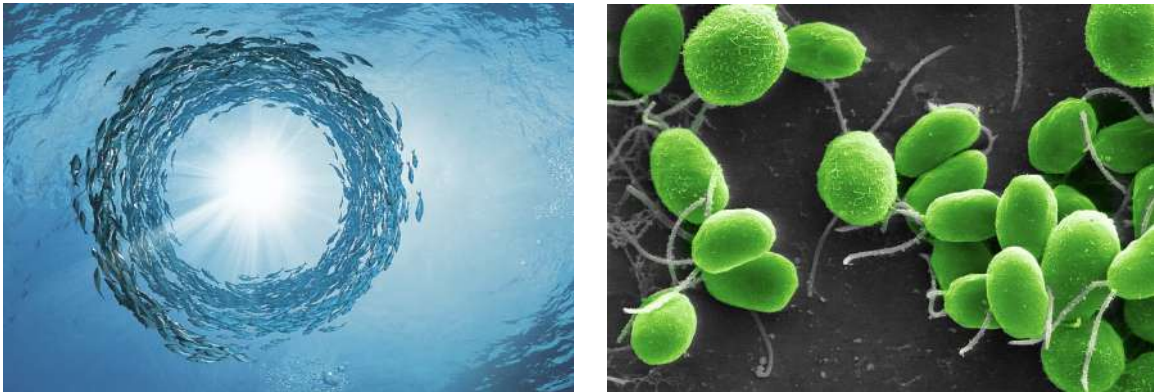


Fig. 1 Two examples of active matter systems, (a) School of fish in open water describing a closed toroidal geometry, and (b) a colony of *Chlamydomonas reinhardtii* algae, fascinating unicellular green organisms used as an early and prominent model system for third generation energy resources which prompted scientists to do extended research on physiology and signaling during the algae life cycle.

On the nano- and microscale, biology provides a plethora of active agents ranging from enzymes [12, 13], the cytoskeleton in living cells [4, 7, 14–21] to microswimmers [1, 4, 22, 23], e.g., sperm, algae, bacteria, and a diversity of planktonic microorganisms [1, 4, 22, 23]. Microswimmers are characterized by swimming in regimes in which the viscous forces with the fluid dominate over the inertia. The ratio of such forces, known as Reynolds number is on the order of  $\sim 10^{-5}$ , while for macroscopic systems like fish or humans in water are exposed to Reynolds numbers of  $\sim 10^5$ . At low Reynolds numbers there is almost no inertial delay in time between the applied forces and the fluid response is almost instantaneous. In this viscous regime, time non-periodic motion will achieve net displacement [3].

In nature, exists a rich variety of propulsion mechanisms that endure active agents to generate net motion. Sperm cells break spatial symmetry by beating its flexible

flagellum back and forth [24–26], while some bacteria, such as *Paramecia*, whose body is all covered by beating cilia, synchronize causing metachronal waves which translates into the forward motion of the cell [27], or *Escherichia coli*, [22, 28, 29] are propelled by rotating helical filaments attached to their bodies. The actin filaments of the cytoskeleton are driven by molecular motors [7, 18–21, 30], or ATP-dependent enzymatic activity-induced mechanical fluctuations drive molecular motion in the bacterial cytoplasm and the nucleus of eukaryotic cells [31].

### 0.1.1 Bacteria and bio-polymers

A fundamental determinant of microbial life is morphology. Nearly all bacteria are spherical (*Chlamydomonas reinhardtii*, Fig.1(b)) or moderately elongated (*E. coli*, Fig.2(a), self-assembled dinoflagellates [32, 33]), generally ranging in size from  $0.3\mu\text{m}$  up to almost  $1\text{mm}$ . Another example are *Proteus mirabilis*, rod-shaped bacteria responsible for the 90% of all *Proteus* infections in humans, which grow in bacterial colonies or biofilms, and show swarming motility [34]. On the other hand, Phytoplankton range from  $1\mu\text{m}$  to a few millimeters in size, are morphologically much more diverse and can be found single-celled or colonies, often arranged in chains as shown in 2(c). Their beauty and morphological complexity have amazed generations of ecologists, but the adaptive significance of their form often remains unknown.

Elongated filaments render active soft matter a promising class of new materials [36, 37]. Nature provides various examples of filamentous, polymer-like active agents or phenomena where activity governs the nonequilibrium dynamics of passive molecules. Propelled biological polar semiflexible filaments are ubiquitous, e.g., filamentous actin or microtubules in the cell cytoskeleton due to tread-milling and motor proteins [35, 38]. In motility assays, filaments are propelled on carpets of motor proteins anchored on a substrate, which results in a directed motion and the appearance of self-organized dynamical patterns [7, 10, 14, 18–21, 30, 39, 40]. Furthermore, the active dynamics of microtubules [41] or actin-filaments [42] leads to an accelerated motion of chromosomal loci [31, 43] and chromatin [44].

### 0.1.2 Assembly of active colloids

Artificial active particles have been synthesized utilizing mostly chemical or physical propulsion mechanisms [2, 45–50]. Janus particles belong to the category of artificial microswimmers, whose fabrication is achieved by coating their surfaces with two different reacting materials [2]. The locomotion of such particles is achieved by originating gradients, and not by breaking spatial symmetry as usual in biological swimmers. The flow around the particle is generated by thermal, chemical concentration, or electric/magnetic field gradients [2, 51, 52]. The flexible linker between such Janus

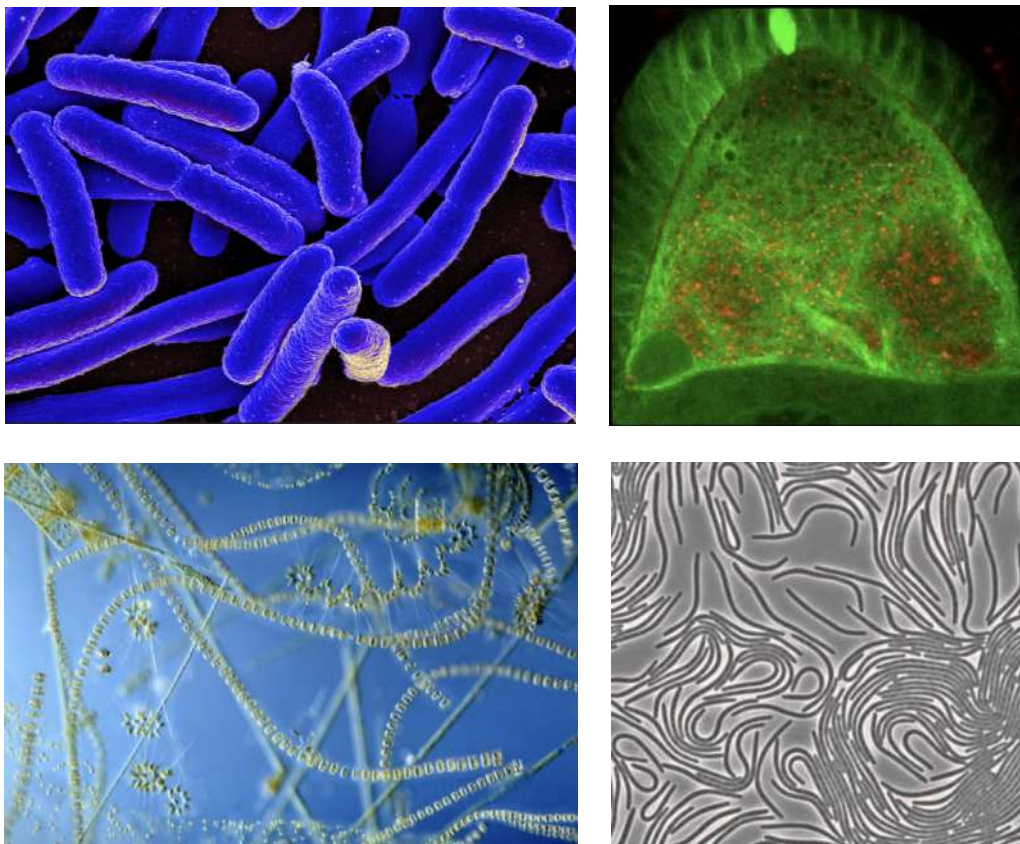


Fig. 2 (a) *E. coli* are rod-shaped, coliform bacteria that are propelled by rotating large helical filaments, (b) the analysis of the microtubules flow (fluorescent green lines) inside the cytoskeleton of a *Drosophila Oocyte* reveals emerging cytoplasmic flow patterns and an enhancement of the vesicles (red dots) and other particles embedded in the active fluid [35], (c) fluid mechanics governs a wide range of functions for tonic organisms, from propulsion to nutrient uptake to fertilization. In particular, Phytoplankton are mostly microscopic, unicellular photosynthetic organisms that live suspended in water, and (d) an aggregate of *Proteus mirabilis* in a biofilm.

particles can be realized using stripes of DNA [53], where magnetic colloids connected by double-stranded DNAs have been studied.

Moreover, synthetic active or activated colloidal polymers [54] are nowadays synthesized in various ways. Assembly of active chains can be directly arranged by connecting self-propelling Janus particles (monomers) by flexible linkers. Assembly of active chains of metal-dielectric Janus colloids can be achieved by imbalanced interactions, where simultaneously the motility and the colloid interactions are controlled by an AC electric field [55–57]. Electrohydrodynamic convection rolls lead to self-assembled colloidal chains in a nematic liquid crystal matrix and directed movement [58]. Moreover, chains of linked colloids, which are uniformly coated with catalytic

nanoparticles, have been synthesized [59]. Hydrogen peroxide decomposition on the surfaces of the colloidal monomers generates phoretic flows, and active hydrodynamic interactions between monomers results in an enhanced diffusive motion [59]. Fig.3 shows two examples of synthetic active colloidal polymers consisting of several species of colloidal particles tightly bound together.

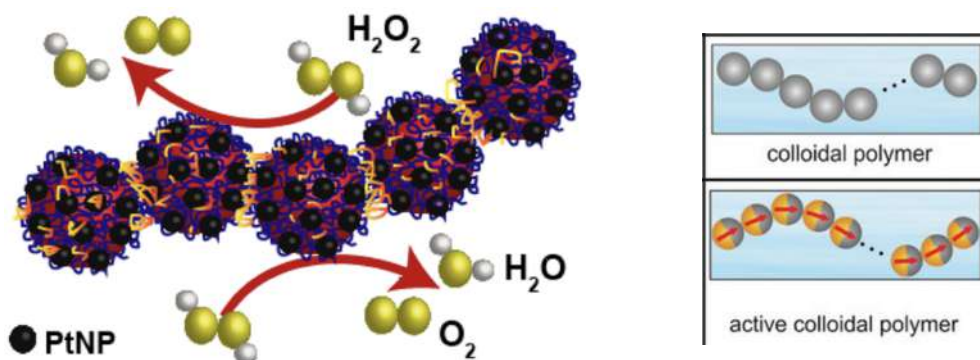


Fig. 3 (a) Synthetic active colloidal semiflexible chain with a characteristic size of  $\sim 5\mu m$  [59]. (b) Representation of a passive and an active colloidal polymer in a solvent. For the active case, an active colloid is indicated by a Janus particle with a red arrow indicating the self-propulsion direction[54].

## 0.2 Hydrodynamics in active filamentous systems

Valuable insight into the properties of self-propelled filaments/polymers, or their passive counterparts exposed to an active bath, is obtained by computer simulations and analytical theory. Filaments are modeled as semiflexible polymers, with an implementation of activity adapted to the particular propulsion mechanism. Polar polymers, which are not force free, representing actin filaments or microtubules driven by molecular motors, are typically propelled by forces tangential to the polymer contour [11, 60–65]. In addition, self-propelled polymers, where activity is taken into account by independent site velocities, with orientations changing in a diffusive manner, have been considered; in absence of hydrodynamic interactions (HI) [60, 63, 66–77], but also accounting for fluid-mediate interactions [59, 61, 62, 78–80].

In fact, the spontaneous motion in dilute and viscous solutions of elongated filaments/ polymer-like objects are common in biology. Microswimmers rely on the beating and rotation cilia or flagella for propulsion, as well as for going through periodic changes of their body shape. These systems are characterized for undergoing a spontaneous motion of their slender bodies, for being small enough to consider Brownian fluctuations relevant, and also for resisting deformations produced by the flow

field and Brownian fluctuations. The emerging behavior of such filaments appear from the interplay between fluid flow, Brownian fluctuations and the polymer elasticity, i.e., bending and bonding forces. Such systems raise a challenging new class of fluid-structure interaction problems [81]. Hydrodynamic interactions is proven to change the properties of active systems in various ways. An individual self-propelled particle—an isolated monomer in the case of a colloidal-type polymer [54]—is force and torque free, and creates a flow field lacking a Stokeslet, but includes higher multipole contributions [9, 10, 24, 79, 82–85]. In all cases, a faster dynamics of the polymer center-of-mass with increasing activity is obtained [63, 67, 69, 71, 74–76, 86]. Interestingly, conformational changes in polymers/colloidal chains and the interference of the monomers/colloids flow fields lead to autonomous polymer motion even when individual monomers are non-motile [59, 78, 79].

### 0.3 Summary

In this manuscript, we provide detailed analytical and computational studies to characterize the conformations and dynamical properties of a variety of filamentous/polymer-like agents on the mesoscopic level ( $100nm - 100\mu m$ ), where classical mechanics is still satisfied and thermal fluctuations from the environment become relevant. Such polymers are exposed to several environmental conditions, e.g., shear stress, fluid mediated interactions, active correlated bath, confinement, etc. After this introduction, the thesis starts with Chapter 1, the theoretical background, in which the fundamentals, mathematical models and theory in Stochastic Dynamics, Hydrodynamics and Active Matter are explained in detail. In this thesis, activity is considered as an independent stochastic process with an exponential temporal correlation acting on the sites of the polymer. Hence, the amount of activity on a system will give us a measure of how far from equilibrium that system is, and how persistently the constituting entities are moving.

The core of the thesis is divided in four main chapters (Ch. 2-5), which include the novel studies, findings and results of this work. Chapter 2 introduces the continuous Gaussian semiflexible polymer model extended by the activity under shear stress. Similarly to passive polymers, this extended model yields a Weissenberg-number dependent shear-induced deformation, alignment, and shear thinning behavior. For flexible polymers, activity enhances the shear-induced polymer deformation. Independent of stiffness, activity-induced swelling facilitates and enhances alignment and shear thinning compared to a passive polymer. In Chapter 3, the analytical approach for active semiflexible polymer is also used [87–93], followed by the validation of the results with Brownian dynamics simulations. Single active Brownian polymers (denoted as ABPO), are discrete linear chain composed of active Brownian particles, as a minimal

model for self-propelled polymeric object. Active Brownian polymers have already been studied analytically before [69, 73, 75, 94], but finite extensibility of the polymer length is a key property that has been neglected so far. We show that the constraint of a finite polymer contour length leads to distinctly different behavior compared with studies neglecting such property. Furthermore, we show that hydrodynamic interactions and how they are coupled with activity, through the polymer equation of motion, have a key effect on the polymer dynamics and conformational properties. Here, no Stokeslets of active origin are generated. At low activities, HI lead to a significant shrinkage of semiflexible and flexible polymers, while active free-draining flexible polymers swell monotonically. Large activities imply a reswelling, however, to a less extent than for non-HI polymers, caused by the shorter polymer relaxation times due to hydrodynamic interactions. The polymer mean square displacement is enhanced, and an activity-determined ballistic regime appears. Chapter 4 presents a similar study than Ch. 3, but with a different origin of the active source is depicted. This chapter presents the conformational and dynamical properties of semiflexible polymers in solution moved by external colored noise. Here, a Stokeslet fluid due to active forces is now generated. We introduce the multiparticle collision approach (MPC) to describe the surrounding fluid which is coupled to our Brownian dynamics simulations (polymer dynamics), and are further compared with our analytical and numerical approaches. Now, HI lead to an enhanced swelling of flexible polymers by increasing activity, and the conformational properties differ substantially from the self-propelled polymers in presence of HI and the free-draining ones.

To support simulations in Ch.3, for active Brownian polymers in dilute solutions, Chapter 5 adopts the MPC approach for fluids coupled with semiflexible polymers in presence of external active noise. After comparing the conformational properties with the Brownian dynamics simulations, we find excellent quantitative and qualitative agreement.



# Chapter 1

## Theoretical background

### 1.1 Stochastic dynamics

Stochastic dynamical systems comprise all those systems which are subjected to random forces. This randomness or "noise" represents the effect of a large number of environmental degrees of freedom. Stochastic systems can be modeled by stochastic differential equations, in which one or more terms are stochastic or random processes. In this chapter, we briefly introduce the main concepts of stochastic systems and add a few commonly used examples present in most biological and physical systems, e.g., the well-known Brownian motion, the Ornstein-Uhlenbeck process, etc.

#### 1.1.1 Langevin dynamics

Mesoscopic objects such as colloids or macromolecules show a considerably slower dynamics and are significantly larger than embedded fluid particles. Then, the interactions of a solute with the surrounding fluid can be expressed in an effective way, where the fluid is considered as a frictional background and exerts random forces produced by thermal agitation on the solute particle. Drag and random forces are not independent, but rather linked, which is expressed by the so-called fluctuation-dissipation theorem [95].

Therefore, the dynamics of mesoscopic objects embedded in a fluid at thermal equilibrium can be described by the Langevin equation [95, 96]

$$M\ddot{\mathbf{r}}(t) = -\gamma\dot{\mathbf{r}}(t) + \mathbf{F}(t) + \mathbf{F}(t), \quad (1.1)$$

where  $M$  is the mass of the object, and the terms  $\ddot{\mathbf{r}}$  and  $\dot{\mathbf{r}}$  denote its acceleration and velocity at time  $t$ , respectively. The expression  $\gamma\dot{\mathbf{r}}$  is the frictional force, with drag coefficient  $\gamma$ , and  $\mathbf{F}$  is the stochastic force accounting for the collision of the fluid

## Theoretical background

---

particles with the colloid. For colloids,  $\gamma$  is given by the Stokes law  $\gamma = 6\pi\eta r_c$ , with  $\eta$  the viscosity of the fluid and  $r_c$  the colloid radius.

The stochastic force is considered as a Gaussian and Markovian process, meaning that the process is  $\delta$ -correlated with the first two moments[95]

$$\langle \mathbf{F} \rangle = 0, \quad (1.2)$$

$$\langle \mathbf{F}(t) \cdot \mathbf{F}(t') \rangle = 6\gamma k_B T \delta(t - t') \quad (1.3)$$

Here,  $k_B$  is the Boltzmann constant, and  $T$  is the temperature. The amplitude  $6\gamma k_B T$  from the second moment can be derived from the fluctuation-dissipation theorem [96]. It is also important to mention that hydrodynamic interactions, and electrostatic or hydrophobic effects are not captured by the standard Langevin dynamics.

The well-known time regime, where the drag forces acting on the fluid dominate over inertia is called Brownian dynamics (BD). In this overdamped limit, the acceleration of the particle is negligible compared to the drag contribution,  $|M\ddot{\mathbf{r}}| \ll |\gamma\dot{\mathbf{r}}|$ . Thus, the Langevin equation (1.1) can be approximated by the expression

$$\dot{\mathbf{r}}(t) = \frac{1}{\gamma} [\mathbf{F}(t) + \mathbf{F}(t)]. \quad (1.4)$$

### 1.1.2 Ornstein-Uhlenbeck process

Typically, systems out-of-equilibrium are characterized by not following a Gaussian and Markovian process (*with noise*), but rather describing a non-Markovian process, i.e. *colored noise*, where the particles velocity correlation decay exponentially in time. A Markovian process can be recovered by extending phase-space by an additional variable exposed to white noise, with a temporal exponential correlation of the additional variable. The effective set of stochastic equations is often of the form of the Ornstein-Uhlenbeck process.

The general form of an Ornstein-Uhlenbeck process [95] for  $f$  stochastic process variables  $X_i$  can be written as a system of linear stochastic differential equations with constant coefficients,

$$\dot{X}_i + \sum_{j=1}^f \omega_{ij} X_j = \Gamma_i(t). \quad (1.5)$$

Here,  $X_i$  denote the process variables,  $\omega_{ij}$  are constant matrix elements, and  $\Gamma_i$  are the Gaussian distributed stochastic forces with the moments

$$\langle \Gamma_i \rangle = 0, \quad \langle \Gamma_i(t) \Gamma_j(t') \rangle = b_{ij} \delta(t - t') \quad (1.6)$$

where  $b_{ij} = b_{ji}$ , and describe the strength of the noise[95]. The general solution of Eq. (1.5) can be found via the method of Green's function as

$$X_i(t) = X_i^h(t) + X_i^{ih}(t) \quad (1.7)$$

where  $X_i^h(t)$  and  $X_i^{ih}(t)$ , the homogeneous and inhomogeneous solutions, respectively, have the forms

$$X_i^h(t) = \sum_j G_{ij}(t) X_j(t^*), \quad (1.8)$$

$$X_i^{ih}(t) = \sum_j \int_{t^*}^t G_{ij}(t-t') \Gamma_j(t') dt'. \quad (1.9)$$

Thereby,  $G_{ij}$  obeys the initial condition  $G_{ij}(t^*) = \delta_{ij}$  at time  $t^*$ ,  $X_i(t^*) \equiv X_i^*$ , and the differential equation

$$\dot{G}_{ij} + \sum_l \omega_{il} G_{lj} = 0, \quad (1.10)$$

with the straightforward solution

$$G_{ij} = [\exp(-\boldsymbol{\omega} t)]_{ij} \approx \delta_{ij} - \omega_{ij} t + \frac{1}{2} \omega_{ij}^2 t^2 + \mathcal{O}(\omega_{ij} t)^3. \quad (1.11)$$

Finally, the general solution is

$$X_i(t) = \sum_j G_{ij}(t-t^*) X_j^* + \sum_j \int_{t^*}^t G_{ij}(t-t') \Gamma_j(t') dt', \quad (1.12)$$

where the identities  $\mathbf{G}^{-1}(t) = \mathbf{G}(-t)$  and  $\mathbf{G}(t) \mathbf{G}^{-1}(t^*) = \mathbf{G}(t-t^*)$  were used. Using these results, we can calculate the first moment for the  $i$ -th stochastic process variable,  $X_i$ , as

$$\mu_i(t) = \langle X_i(t) \rangle = \sum_j G_{ij}(t-t^*) X_j^*, \quad (1.13)$$

and the second moment,

$$\begin{aligned} \sigma_{ij}(t) &= \langle (X_i(t) - \mu_i(t)) \cdot (X_j(t) - \mu_j(t)) \rangle = \dots \\ &= \sum_{kl} \int_{t^*}^t G_{ik}(t-t') G_{jl}(t-t') b_{kl} dt' = \sigma_{ji}. \end{aligned} \quad (1.14)$$

### 1.1.3 Fokker-Planck equation

The Fokker-Planck equations is an equivalent formulation of a stochastic process in terms of a probability density distribution function  $p(\mathbf{X}, t)$  [95]. For simplicity, the

## Theoretical background

---

calculations are expressed for a one spatial coordinate. The stochastic process of Eq. (1.29) leads to

$$\frac{\partial p(\mathbf{X}, t)}{\partial t} = \omega_{ij} \frac{\partial}{\partial X_i} [x_j p(\mathbf{X}, t)] + D_{ij} \frac{\partial^2 p(\mathbf{X}, t)}{\partial X_i \partial X_j}, \quad (1.15)$$

where the Einstein summation convention is used. The conditional probability density distribution function

$$p(\mathbf{X}, t) = p(\mathbf{X}, t | \mathbf{X}^*, t^*) p(\mathbf{X}^*, t^*) \quad (1.16)$$

obeys the same equation of motion as  $p(\mathbf{X}, t)$ , with the initial condition

$$p(\mathbf{X}, t | \mathbf{X}^*, t^*) = \delta(\mathbf{X} - \mathbf{X}^*). \quad (1.17)$$

Expressing  $p(\mathbf{X}, t)$  by its Fourier transformation  $\tilde{p}(\mathbf{k}, t | \mathbf{X}^*, t^*)$ , the linear differential equation in Eq. (1.15) reads

$$\frac{\partial \tilde{p}(\mathbf{k}, t)}{\partial t} = -\omega_{ij} k_i \frac{\partial \tilde{p}(\mathbf{k}, t)}{\partial k_j} - D_{ij} k_i k_j \tilde{p}(\mathbf{k}, t). \quad (1.18)$$

where  $\tilde{p}$  is the Fourier transform of  $p$ ,

$$p(\mathbf{X}, t | \mathbf{X}^*, t^*) = \frac{1}{(2\pi)^m} \int e^{i \sum_j k_j X_j} \tilde{p}(\mathbf{k}, t | \mathbf{X}^*, t^*) d^m k. \quad (1.19)$$

and the initial condition after the transformation is

$$\tilde{p}(\mathbf{k}, t^* | \mathbf{X}^*, t^*) = e^{-i \sum_j k_j X_j^*}. \quad (1.20)$$

Considering that  $p(\mathbf{X}, t)$  and the corresponding Fourier transform  $\tilde{p}(\mathbf{k}, t)$  are Gaussian functions[95, 97], the solution of Eq. (1.19) is

$$\tilde{p}(\mathbf{k}, t | \mathbf{X}^*, t^*) = \exp \left[ -i \sum_j k_j \mu_j (t - t^*) - \frac{1}{2} \sum_j k_i k_j \sigma_{ij} (t - t^*) \right]. \quad (1.21)$$

Inserting Eq. (1.21) into Eq. (1.18) and sorting by powers of  $k$  yields the two differential equations

$$\dot{\mu}_i = - \sum_j \omega_{ij} \mu_j, \quad (1.22)$$

$$\dot{\sigma}_{ij} = - \sum_l (\omega_{il} \sigma_{lj} - \omega_{jl} \sigma_{li}) + 2D_{ij} \quad (1.23)$$

and their respective initial conditions

$$\mu_i(t^*) = \mu_i^*, \quad (1.24)$$

$$\sigma_{ij}(t^*) = 0. \quad (1.25)$$

By inserting the Green function Eq. (1.11) into the Fourier transformed Eq. (1.19), the solutions is

$$\mu_i(t) = \sum_j G_{ij}(t - t^*)x'_j, \quad (1.26)$$

$$\sigma_{ij}(t) = 2 \sum_{k,l} \int_0^t G_{ik}(t' - t^*) D_{kl} G_{lj}(t' - t^*) dt'. \quad (1.27)$$

Finally, inserting the Fourier transform  $\tilde{p}(\mathbf{k}, t)$  from Eq. (1.21) in  $p(\mathbf{X}, t)$  from Eq. (1.19) yields the conditional probability density distribution function in space

$$p(\mathbf{X}, t | \mathbf{X}^*, t^*) = \frac{1}{(2\pi)^{N/2}} \frac{1}{\sqrt{|\boldsymbol{\sigma}(t - t^*)|}} \times \exp \left( -\frac{1}{2} [X_i - G_{ik}(t - t^*)X_k^*] [\boldsymbol{\sigma}^{-1}(t - t^*)]_{ij} [X_j - G_{jl}(t - t^*)X_l^*] \right). \quad (1.28)$$

with the Jacobian  $|\boldsymbol{\sigma}(t)|^{1/2}$ . Since  $\sigma_{ij} = \sigma_{ji}$ ,  $\sigma_{ij}$  is assumed to be positive definite, and the inverse  $[\boldsymbol{\sigma}^{-1}]_{ij}$ , square root  $[\boldsymbol{\sigma}^{1/2}]_{ij}$  and inverse square root  $[\boldsymbol{\sigma}^{-1/2}]_{ij}$  exist and are symmetric.

### 1.1.4 Itô calculus

The Itô calculus is a branch of calculus which involves stochastic processes, and in particular, systems driven by Wiener processes such as Brownian motion. Thus, the stochastic differential equation for the Itô process of a Brownian motion in one dimension is

$$dX(t) = b(X(t), t)dW(t) + F(t)dt \quad (1.29)$$

with an instantaneous diffusion coefficient  $D(X(t), t) = [b(X(t), t)]^2 / 2$ , an stochastic process  $dW(t) = \Gamma(t)dt$ , with  $\Gamma$  as the stochastic variable, and an instantaneous drift (or force)  $F(t)$ . Note that the corresponding random term,  $b(X(t), t)$ , in eq. (1.29) explicitly depend on the state of the system (i.e. on  $X(t)$ ), we call it multiplicative noise. In contrast, we would have additive noise in the equation if  $b(t)$  just depends on time.

## Theoretical background

---

If we extend the Itô calculus for an arbitrary high-dimensional order [96], the  $m$ -dimensional  $W_i$  ( $i = 1, 2, \dots, m$ ) independent Wiener processes fulfill the properties,

$$\begin{aligned}dW_i \cdot dW_j &= \delta_{ij} dt, \\dW_i^\alpha &= 0 \quad (\alpha > 2), \\dW_i \cdot dt &= 0 \quad \text{and} \\dt^\alpha &= 0 \quad (\alpha > 1).\end{aligned}\tag{1.30}$$

Now, supposing that a certain function  $f(X, t)$  is twice continuously differentiable and  $X_i$  ( $i = 1, 2, \dots, m$ ) is a vector process,  $df(X, t)$  will be also an Itô process with the differential,

$$df = \left( \sum_i \frac{\partial f}{\partial X_i} F_i + \sum_i \frac{\partial f}{\partial t} + \sum_{i,j} \frac{1}{2} \frac{\partial^2 f}{\partial X_i \partial X_j} b_i b_j \right) dt + \sum_{i,j} \frac{\partial f}{\partial X_i} b_i b_j dW_j(t).\tag{1.31}$$

We applied the notation  $F_i = F(X_i(t), t)$  and  $b_i = b(X_i(t), t)$ . Usually, one of the variables, say  $X_1$ , is the time  $t$  and  $dX_1 = dt$ . In this case,  $b_{1j} = 0$  for all  $j$  and  $F_1 = F(t)$ .

## 1.2 Hydrodynamics

Until now, we have considered the dynamics of embedding fluid particles in a stochastic environment where the correlations of the fluid are neglected. However, the dynamics of solute particles in a fluid environment can be affected by the motion of the fluid, commonly known as hydrodynamic interactions. To start with the description of our fluid, we consider it as a continuum characterized by its mass density  $\rho(\mathbf{r}, t)$ , local stress  $\boldsymbol{\sigma}(\mathbf{r}, t)$ , and fluid velocity  $\mathbf{u}(\mathbf{r}, t)$ , where each quantity is given at a specific position  $\mathbf{r}$  and time  $t$ . In this chapter, we introduce the Navier-Stokes equations as the hydrodynamic equations governing the time evolution of these quantities. Furthermore, we describe in detail a particle-based mesoscale simulation approach, the multiparticle collision dynamics method (MPC), which accounts for both the correlations of the fluid and the stochasticity of the thermal bath.

### 1.2.1 Navier-Stokes equations

In the framework of fluid mechanics, the Navier-Stokes equations are partial differential equations that describe the motion for a viscous, heat conducting fluid. These equations arise from applying Newton's second law of motion, together with the assumption that the stress in the fluid is the sum of a diffusing viscous term and a pressure term.

Considering a fixed mass of material in a volume  $V$ , the rate of change of a certain property  $g(\mathbf{r}, t)$  of such material volume is given by

$$\frac{Dg}{Dt} = \frac{\partial g}{\partial t} + \mathbf{v} \cdot \nabla g, \quad (1.32)$$

where  $D/Dt$  is defined as the material derivative. In general, the whole mass inside of the material volume  $V$  is given by  $M = \int_V \rho dV$ . Thus, assuming the conservation of mass,  $dM/dt = 0$ , inside the material volume  $V$ , since a the mass of the material under changes in size, position, volume or surface over time is assumed to be fixed. By means of the Leibniz-Reynolds transport theorem and applying also Gauss' theorem, follows for any volume  $V$ , [98]

$$\frac{d}{dt} \int_V \rho dV = \int_V \left( \frac{\partial \rho}{\partial t} + \nabla \cdot (\rho \mathbf{u}) \right) = 0. \quad (1.33)$$

Hence,

$$\frac{\partial \rho}{\partial t} + \nabla \cdot (\rho \mathbf{u}) = 0. \quad (1.34)$$

## Theoretical background

---

This is the continuity equation in the case of incompressible fluids, the mass density inside the volume  $V$  is constant in time,  $\partial\rho/\partial t = 0$ , and consequently,  $\nabla \cdot (\rho\mathbf{v}) = 0$ .

The Navier-Stokes equations represent the conservation of momentum. The extension of Newton's second law of motion for a fluid is given by the Cauchy momentum equation of motion, which in the Eulerian form reads

$$\rho \left( \frac{\partial \mathbf{u}}{\partial t} + (\mathbf{u} \cdot \nabla) \mathbf{u} \right) = \nabla \cdot \boldsymbol{\sigma} + \mathbf{f}. \quad (1.35)$$

Here,  $\boldsymbol{\sigma}$  is the fluid stress tensor, and  $\mathbf{f}$  is the force density acting on the fluid. For a Newtonian fluid, the stress tensor is given by, [99]

$$\boldsymbol{\sigma} = -p(\mathbf{r}, t)\mathbf{I} + \eta \left[ \frac{\partial \mathbf{u}}{\partial t} + \left( \frac{\partial \mathbf{u}}{\partial t} \right)^T \right] - \left( \frac{2}{3}\eta - \eta^V \right) \nabla \cdot \mathbf{v} \quad (1.36)$$

with  $p(\mathbf{r}, t)\mathbf{I}$  as the hydrostatic local pressure in the fluid, and  $\eta$  and  $\eta^V$  the shear and bulk viscosities, respectively. Now, adding the stress tensor (Eq. (1.36)) into the Navier-Stokes equation (Eq. (1.35)) turn into

$$\rho \left( \frac{\partial \mathbf{u}}{\partial t} + (\mathbf{u} \cdot \nabla) \mathbf{u} \right) = -\nabla p + \eta \Delta \mathbf{u} + \left( \frac{\eta}{3} + \eta^V \right) \nabla (\nabla \cdot \mathbf{u}) + \mathbf{f}. \quad (1.37)$$

While assuming an incompressible flow and the condition of mass conservation, the equation reads

$$\rho \left( \frac{\partial \mathbf{u}}{\partial t} + (\mathbf{u} \cdot \nabla) \mathbf{u} \right) = -\nabla p + \eta \Delta \mathbf{u} + \mathbf{f}. \quad (1.38)$$

In order to study the different contributions in the Navier-Stokes equation, we introduce the dimensionless quantities

$$\mathbf{u}' = \mathbf{u}/U_0, \quad \mathbf{r}' = \mathbf{r}/L_0, \quad t' = t/T_0, \quad (1.39)$$

where  $U_0$ ,  $L_0$ , and  $T_0$  are the characteristic velocity, length and time scales of the system, respectively. Thereby, the Navier-Stokes equation turns into the dimensionless equation

$$Re_T \frac{\partial \mathbf{u}'}{\partial t'} + Re (\mathbf{u}' \cdot \nabla') \mathbf{u}' = -\nabla' p' + \Delta' \mathbf{u}' + \mathbf{f}' \quad (1.40)$$

where  $p' = L_0 \eta^{-1} v_0^{-1} p$ ,  $\mathbf{f}' = L_0 \eta^{-1} v_0^{-1} \mathbf{f}$  and  $\nabla' = \partial/\partial \mathbf{r}'$ , all in dimensionless units. In addition, the Reynolds numbers are  $Re = \rho v_0 L_0 / \eta$  and  $Re_T = \rho L_0^2 / \eta T_0$  are introduced.

For the limit case of  $Re \ll 1$ , the non-linear advective term is negligible and the Navier-Stokes equations can be linearized. Thus, considering an incompressible fluid we get the equation

$$\rho \partial \mathbf{u} / \partial t = -\nabla p + \eta \Delta \mathbf{u} + \mathbf{f}. \quad (1.41)$$

On the top of that,  $Re_T \ll 1$ , we obtain an instantaneous relaxation of the hydrodynamic interactions compared to the characteristic scales in the system. Hence, the Stokes equations, also called creeping flow equations, arises in the form

$$\eta \Delta \mathbf{u} - \nabla p + \mathbf{f} = 0, \quad (1.42)$$

$$\nabla \cdot \mathbf{v} = 0. \quad (1.43)$$

### 1.2.2 Hydrodynamic interactions

To solve the linear Stokes equations (1.42) and (1.43), we apply the Fourier transformation  $\mathbf{u}(\mathbf{r}) = \int \mathbf{u}_q e^{-2i\pi \mathbf{q} \cdot \mathbf{r}} d\mathbf{q}^3$ , which yield

$$\eta \mathbf{q}^2 \mathbf{u}_q - i\mathbf{q} p_q = \mathbf{f}_q, \quad (1.44)$$

$$\mathbf{q} \cdot \mathbf{u}_q = 0. \quad (1.45)$$

These algebraic equations can be easily solved, and we obtain

$$\mathbf{u}(\mathbf{r}) = \int \mathbf{G}(\mathbf{r} - \mathbf{r}') \mathbf{f}(\mathbf{r}') d^3 r', \quad (1.46)$$

with the Green's function  $\mathbf{G}(\mathbf{r})$

$$\mathbf{G}(\mathbf{r}) = \frac{1}{4\pi\eta r} \mathbf{I} - \frac{1}{8\pi\eta} \nabla \otimes (\nabla \mathbf{r}). \quad (1.47)$$

Due to the fact that  $\nabla \mathbf{r} = \frac{\mathbf{r}}{r}$  and  $\nabla \otimes \mathbf{r} = \mathbf{I}$ , with  $\mathbf{I}$  as the unit matrix, we can write

$$\frac{1}{8\pi\eta} \nabla \otimes (\nabla \mathbf{r}) = \frac{1}{8\pi\eta} \nabla \otimes \left( \frac{\mathbf{r}}{r} \right) = -\frac{1}{8\pi\eta} \frac{\mathbf{r} \mathbf{r}^T}{r^3} + \frac{\mathbf{I}}{8\pi\eta r} \quad (1.48)$$

where we have used the Leibniz chain rule for calculation of  $\nabla \otimes \left( \frac{\mathbf{r}}{r} \right)$ . The Green's propagator, also known in literature as the hydrodynamic Oseen tensor, reads

$$\mathbf{G}(\mathbf{r}) = \frac{1}{8\pi\eta r} \left( \mathbf{I} + \frac{\mathbf{r} \mathbf{r}^T}{r^2} \right), \quad (1.49)$$

with  $\mathbf{r} \otimes \mathbf{r} = \mathbf{r} \mathbf{r}^T$ . The corresponding velocity field is also referred to as Stokeslet. [100]

### 1.2.3 Equations of motion of particles in fluid

In the creeping-flow limit, where the flow is linear and propagates instantaneously, the hydrodynamic forces exerted on the immersed particle  $i$  due to the motion of the other  $(N - 1)$  particles is

$$\mathbf{F}_i^h = - \sum_{j=1}^N \boldsymbol{\gamma}_{ij} \mathbf{u}_j, \quad (1.50)$$

with the velocity

$$\mathbf{u}_i = - \sum_{j=1}^N \boldsymbol{\mu}_{ij} \mathbf{F}_j^h. \quad (1.51)$$

where  $\boldsymbol{\gamma}_{ij}$  and  $\boldsymbol{\mu}_{ij}$  are the hydrodynamic friction and mobility tensors, respectively. The force density acting on the fluid from the  $i$ -th particle is then given by  $\mathbf{f}(\mathbf{r}) = \mathbf{F}_i \delta(\mathbf{r} - \mathbf{r}_i)$ . Thereby, having a particle moving in a viscous fluid with other  $(N - 1)$  embedded particles will exerts a force  $\mathbf{F}_i = -\mathbf{F}_i^h$  on the surrounding fluid, resulting in a perturbation of the flow field. Such perturbations of the flow fluid will propagate quasi-instantaneously throughout the fluid particles, inducing forces onto the other embedded solute particles. Therefore, the overall flow field  $\mathbf{u}(\mathbf{r})$  originated by the motion of the point-like particles at the position  $\mathbf{r}_i$  can be shown as a linear sum of Green's propagators,

$$\mathbf{u}(\mathbf{r}) = \sum_{i=1}^N \mathbf{G}(\mathbf{r} - \mathbf{r}_i) \mathbf{F}_i. \quad (1.52)$$

Considering the real friction between a particle at  $\mathbf{r}_i$  and the viscous fluid in which the particle is suspended, and with Eq. (1.52), we obtain

$$\dot{\mathbf{r}}_i = \sum_{j=1}^N \left( \mathbf{G}(\mathbf{r}_i - \mathbf{r}_j) + \frac{\delta_{ij}}{\gamma} \right) \mathbf{F}_j, \quad (1.53)$$

from which we can clearly identify the expression for the hydrodynamic mobility tensor

$$\boldsymbol{\mu}_{ij} = \frac{\delta_{ij}}{\gamma} \mathbf{I} + (1 - \delta_{ij}) \mathbf{G}(\mathbf{r}_i - \mathbf{r}_j). \quad (1.54)$$

By substituting  $\mathbf{G}(\mathbf{r}_i - \mathbf{r}_j)$  with the Oseen tensor of Eq. (1.49), we get

$$\boldsymbol{\mu}_{ij} = \frac{\delta_{ij}}{\gamma} \mathbf{I} + (1 - \delta_{ij}) \frac{1}{8\pi\eta r} \left( \mathbf{I} + \frac{\mathbf{r}\mathbf{r}^T}{r^2} \right). \quad (1.55)$$

This expression points out the long-range interactions of the flow field, with a decay of  $\sim 1/r$ , induced by the motion of suspended particles.

For a rigid object with an arbitrary shape, the calculation of the flow field at distance  $\mathbf{r}$  from the solute particle of size  $l$  using Eq. (1.46) becomes untractable and, a multipole expansion can be performed in powers of  $l/r$ . Longer range corrections of spherical objects can be taken into account the Rotne-Prager-Yamakawa (RPY) tensor. The RPY approximation is extensively used to model hydrodynamic interactions between spherical particles suspended in a fluid. At first order, one can approximate the velocity distribution by a point force exerted at the centre of the body. This corresponds to the far field solution, which is the already mentioned Stokeslet (monopole). However, this approximation is no longer satisfied for finite size sphere. We consider a rigid sphere of diameter  $l$  with its center positioned at  $r_i$ . We rewrite Eq. (1.46) using a Taylor expansion and obtain the fluid velocity  $\mathbf{u}(\mathbf{r})$ , with a uniform force density  $\mathbf{f}_i = \mathbf{F}_i / (\pi l^2)$  applied on the sphere surface,

$$\mathbf{u}_i(\mathbf{r}) = \left(1 + \frac{l^2}{6} \nabla_i^2\right) \mathbf{G}(\mathbf{r} - \mathbf{r}_i) \cdot \mathbf{F}_i. \quad (1.56)$$

This naturally leads to a different Green's propagator  $\mathbf{G}(\mathbf{r})$  than the Oseen tensor, namely

$$\Omega(\mathbf{r}_{ij}) = \begin{cases} \frac{1}{8\pi\eta r_{ij}} \left[ \mathbf{I} + \frac{\mathbf{r}_{ij}\mathbf{r}_{ij}^T}{r_{ij}^2} + \frac{l^2}{2r_{ij}^2} \left( \frac{1}{3}\mathbf{I} - \frac{\mathbf{r}_{ij}\mathbf{r}_{ij}^T}{r_{ij}^2} \right) \right], & r_{ij} > l \\ \frac{1}{3\pi\eta l} \left[ \left(1 - \frac{9}{16} \frac{r_{ij}}{l}\right) \mathbf{I} + \frac{3}{16} \frac{r_{ij}}{l} \frac{\mathbf{r}_{ij}\mathbf{r}_{ij}^T}{r_{ij}^2} \right], & r_{ij} < l, \end{cases} \quad (1.57)$$

The velocity correlations decay at least as  $\sim 1/r^4$  for  $r_{ij} < l$ , which results in a positive definite mobility matrix tensor, which is an essential feature in Brownian dynamics simulations.

## 1.3 Simulations of systems with HI

### 1.3.1 Ermak-McCammon scheme

To study soft colloids and polymers in the overdamped Langevin description, several Brownian dynamics simulation algorithms are available in the literature [101–103]. Here, we introduce the Ermak-McCammon algorithm.

In this framework, a system of  $N$  ( $i = 1, \dots, N$ ) solute Brownian particles embedded in a viscous fluid with thermal fluctuations are considered with equation of motion

$$\dot{\mathbf{r}}_i(t) = \sum_{j=0}^N \mathbf{H}_{ij} [\mathbf{F}_j(t) + \mathbf{\Gamma}_i(t)] + k_B T \sum_{j=0}^N \nabla_j \cdot \mathbf{H}_{ij} \quad (1.58)$$

## Theoretical background

---

which relates the velocity of particle  $i$  to forces applied to the rest of the particles including hydrodynamic interactions as given by Eq. (1.53). The tensor  $\mathbf{H}_{ij}$  accounts for the hydrodynamic interactions and has the form

$$\mathbf{H}_{ij} = \delta_{ij}\mathbf{I}/3\pi\eta l + (1 - \delta_{ij})\mathbf{\Omega}_{ij}, \quad (1.59)$$

with the first term accounting for local friction and second term the RPY tensor of Eq. (1.57) for the particle-particle correlations. Thus, the hydrodynamic mobility tensor  $\mathbf{H}_{ij}$  introduces long-range interactions and couples distant particles yields  $\nabla_j \cdot \mathbf{H}_{ij} = 0$  for every particles, and the gradient-mobility term in the Langevin equation vanishes. This is different for a no-slip surface, where this term is non-zero and has to be taken into account. Thermal fluctuations obey the fluctuation-dissipation relation

$$\langle \mathbf{\Gamma}_i(t)\mathbf{\Gamma}_j(t') \rangle = 2k_B T \mathbf{H}_{ij}^{-1} \delta(t - t'). \quad (1.60)$$

The positive-definite mobility matrix  $\mathbf{\Omega}_{ij}$  allows the thermal noise correlation to be numerically implemented by a Cholesky decomposition [101]. For the numerical discretization, the iterative Langevin equation in terms of the dimensionless discrete time variable  $n = t/\Delta t$  and position variable  $\tilde{\mathbf{r}} = \mathbf{r}/l$  now reads

$$\tilde{\mathbf{r}}_i(n+1) = \tilde{\mathbf{r}}_i(n) + \sum_{j=0}^N \tilde{\mathbf{H}}_{ij} \tilde{\mathbf{F}}_j(n) + \sqrt{2\tilde{\mathbf{H}}_{ij}} \tilde{\mathbf{\Gamma}}_i(n), \quad (1.61)$$

where the rescaled forces are  $\tilde{\mathbf{F}}_j = \mathbf{F}_j(l/k_B T)$ , the mobilities are  $\tilde{\mathbf{H}}_{ij} = \mathbf{H}_{ij}(k_B T \Delta t)/l^2$ , and the rescaled thermal noise has the variance unity

$$\langle \tilde{\mathbf{\Gamma}}_i(n)\tilde{\mathbf{\Gamma}}_j^T(m) \rangle = \delta_{nm}\delta_{ij}I. \quad (1.62)$$

### 1.3.2 Multiparticle collision dynamics (MPC)

The multiparticle collision dynamics approach (MPC), introduced by Malevanets and Kapral, [104, 105] is a coarse-grained mesoscale simulation method used to describe the hydrodynamic interactions as well as thermal fluctuations of compressible fluids, i.e., ideal gas. It has been proven that the MPC fluid obeys the Navier-Stokes equation with an ideal gas equation of state [104, 106], and a H-theorem has been derived [104, 107], which ensures the relaxation of the fluid to equilibrium. In addition, the equilibrium distribution function of the velocities has been shown to be Maxwellian [104, 107]. The versatility of this method, allows to couple it with other simulation techniques, e.g., molecular dynamics simulations [108–111]. Moreover, the MPC algorithm is highly

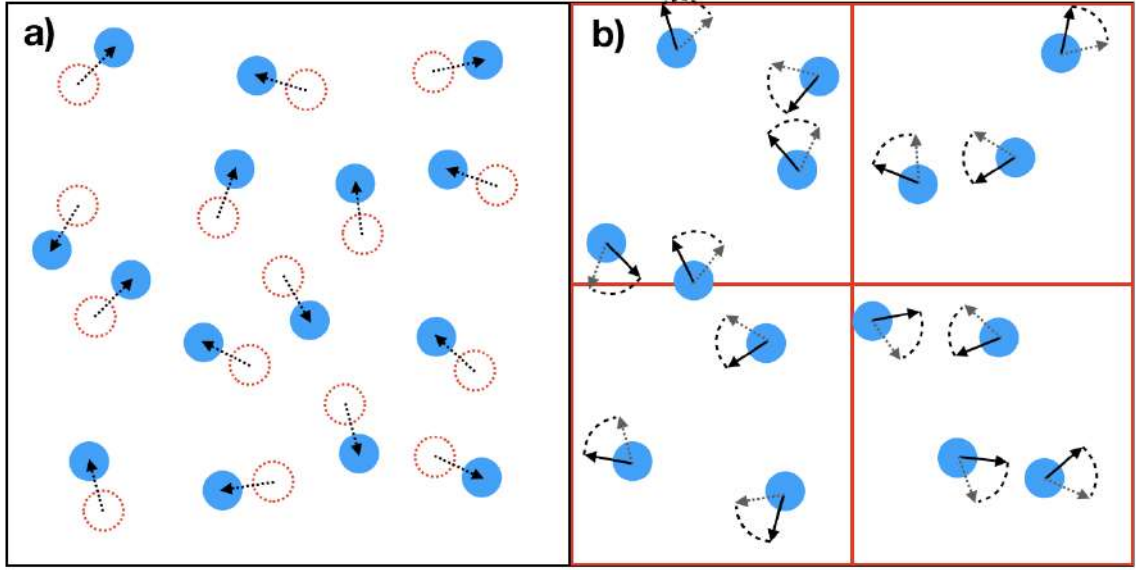


Fig. 1.1 Scheme of the Multiparticle Collision dynamics (MPC) streaming and collision steps. (a) Red dotted circles represent previous particle positions, blue bullets represent the new positions after streaming, and black dotted arrows represent particle velocities. (b) The collision cells are indicated by red lines. Particle velocities (grey arrow) are being rotated respect to the the center-of-mass frame of the individual collision cell to the new velocities (black arrow).

parallel, and is suitable for GPU implementation with a high performance efficiency [112].

The MPC fluid consists of a set of  $N_f$  point-like particles represented by their positions  $\mathbf{r}_i$ , velocities  $\mathbf{v}_i$  ( $i = 1, \dots, N$ ) and mass  $m$ . The algorithm is based in two steps, streaming and collision. In the streaming step, particles move without interacting with each other, but with the freedom to be perturbed by a possible external applied field. Hence, the positions and velocities are updated as

$$\mathbf{r}_i(t+h) = \mathbf{r}_i(t) + h\mathbf{v}_i(t), \quad (1.63)$$

$$\mathbf{v}_i(t+h) = \mathbf{v}_i(t) \quad (1.64)$$

$h$  is the collision time, which is directly related with the viscosity of the fluid [113]. In the collision step, the system is divided into cubic cells of length  $a$ , which defines the local interacting environment. Linear momentum is exchanged between the  $N_c$  particles of a collision cell by applying a rotation of their relative velocities, where  $\mathbf{v}_{i,cm}(t+h) = \mathbf{v}_i(t+h) - \mathbf{v}_{cm}(t+h)$ , around a random oriented axis by an angle  $\alpha$ .

## Theoretical background

---

Thus, the particle velocities are

$$\mathbf{v}_i(t+h) = \mathbf{v}_{cm}(t+h) + \mathbf{R}(\alpha)\mathbf{v}_{i,cm}(t+h) \quad (1.65)$$

where the center-of-mass velocity is  $\mathbf{v}_{cm}(t) = \sum_i \mathbf{v}_i(t)/N_c$ . Here,  $\mathbf{R}$  denotes the rotation operator

$$\mathbf{R}(\alpha) = \begin{pmatrix} \mathcal{R}_x^2 + (1 - \mathcal{R}_x^2) & \mathcal{R}_x \mathcal{R}_y (1 - c) - \mathcal{R}_z s & \mathcal{R}_x \mathcal{R}_z (1 - c) + \mathcal{R}_y s \\ \mathcal{R}_x \mathcal{R}_y (1 - c) + \mathcal{R}_z s & \mathcal{R}_y^2 + (1 - \mathcal{R}_y^2)c & \mathcal{R}_y \mathcal{R}_z (1 - c) - \mathcal{R}_x s \\ \mathcal{R}_x \mathcal{R}_z (1 - c) - \mathcal{R}_y s & \mathcal{R}_y \mathcal{R}_z (1 - c) + \mathcal{R}_x s & \mathcal{R}_z^2 + (1 - \mathcal{R}_z^2)c \end{pmatrix}, \quad (1.66)$$

where  $c = \cos \alpha$ ,  $s = \sin \alpha$ , and  $\mathcal{R} = (\mathcal{R}_x, \mathcal{R}_y, \mathcal{R}_z)$ , with the Cartesian components of  $\mathcal{R}$  defined as

$$\mathcal{R}_x = \sqrt{1 - \theta^2} \cos \varphi, \quad \mathcal{R}_y = \sqrt{1 - \theta^2} \sin \varphi, \quad \mathcal{R}_z = \theta, \quad (1.67)$$

and  $\theta$  and  $\varphi$  are uncorrelated, uniformly distributed random numbers taken from the interval  $[-1, 1]$  and  $[0, 2\pi]$ , respectively. Typically, the rotation angle  $\alpha = 130^\circ$  [111]. In many occasions, e.g., isothermal fluids, systems out of equilibrium, etc., the energy conservation is violated and a mechanism to regulate the temperature of the system has to be implemented. The Maxwell Boltzmann thermostat rescales velocities on the level of individual MPC cells. [114, 115] After every collision step, the relative velocities,  $\mathbf{v}_{i,cm}(t)$ , in each cell are rescaled by a factor  $\kappa$  to get the new velocities

$$\mathbf{v}'_i = \mathbf{v}_{cm} + \kappa \mathbf{v}_{i,cm}, \quad (1.68)$$

with the scaling factor

$$\kappa = \left( \frac{2E_k}{\sum_{i=1}^{N_c} m \mathbf{v}_{i,cm}^2} \right). \quad (1.69)$$

Here,  $E_k$  is the kinetic energy taken from the gamma distribution expected for a canonical ensemble

$$P(E_k) = \frac{1}{E_k \Gamma(f/2)} \left( \frac{E_k}{k_B T} \right)^{f/2} \exp \left( -\frac{E_k}{k_B T} \right), \quad (1.70)$$

with  $\Gamma(x)$  being the gamma function and  $f = 3(N_c - 1)$  is the number of degrees of freedom of the MPC particles in a collision cell.

## 1.4 Active systems

In this chapter, we present the theoretical and computational framework to model active Brownian polymers. In simulations, we rely on the active Brownian polymer model (ABPO) [116, 117], where a discrete linear chain composed of active Brownian particle (ABP) [6, 118, 119] is considered. For the analytical model, we take the continuous Gaussian semiflexible polymer model (GSFP) [87–90, 92, 120], extended by an active force density; the Gaussian active semiflexible polymer (GASFP) [74, 76, 77, 116, 117, 121]. Here, fluid mediated interactions have not been considered yet.

### 1.4.1 Active Brownian particle (ABP)

An active Brownian particle (ABP) is commonly represented as a hard-sphere-type particle being propelled by a constant force along a preferred direction in 3-dimensions

$$\mathbf{e}(t) = (\cos \phi \sin \theta, \sin \phi \sin \theta, \cos \theta)^T. \quad (1.71)$$

which changes direction in a diffusive manner. The equation of motion for the particle position  $\mathbf{r}$  is given by [8, 122]

$$M\ddot{\mathbf{r}}(t) = \gamma\mathbf{v}(t) - \gamma\dot{\mathbf{r}}(t) + \mathbf{F}(t) + \mathbf{\Gamma}(t), \quad (1.72)$$

where  $M$  is the particle mass,  $\mathbf{v}(t) = v_0\mathbf{e}(t)$  is the propulsion velocity with modulus  $v_0$ ,  $\mathbf{F}(t)$  the external force acting on the particle, and  $\mathbf{\Gamma}(t)$  is a Gaussian and Markovian stochastic process accounting for thermal fluctuations of the translational motion. For

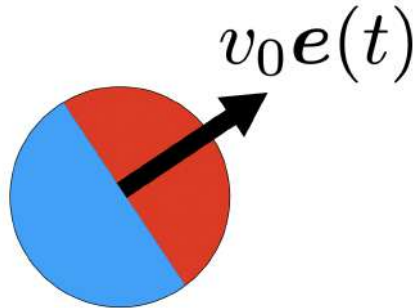


Fig. 1.2 Illustration of an Active Brownian Particle (ABP) represented by a blue-red sphere (resembling a Janus particle). The blue part undergoes the catalytic reaction while the red one does not react with the environment. In average, the ABP propels towards the direction of the active vector  $\mathbf{e}(t)$  (black arrow).

colloids or polymers, we can neglect the inertia term ( $M\ddot{\mathbf{r}}$ ) and adopt the overdamped

## Theoretical background

---

limit Eq. (1.4), which for the active case is

$$\dot{\mathbf{r}}(t) = v_0 \mathbf{e}(t) + \frac{1}{\gamma} [\mathbf{F}(t) + \mathbf{\Gamma}(t)]. \quad (1.73)$$

The stochastic process  $\mathbf{\Gamma}(t)$  first and second moments are given by

$$\langle \mathbf{\Gamma} \rangle = 0, \quad (1.74)$$

$$\langle \Gamma_\alpha(t) \Gamma_\beta(t') \rangle = 2\gamma k_B T \delta_{\alpha\beta} \delta(t - t'). \quad (1.75)$$

Here,  $\delta_{\alpha\beta}$  the Kronecker delta with  $\alpha, \beta \in \{x, y, z\}$ ,  $\delta(t - t')$ . Translational friction coefficient  $\gamma$ , is related with the translational diffusion coefficient  $D_T = k_B T / \gamma$ . The orientation vector  $\mathbf{e}$  of the active velocity  $\mathbf{v}$  is independent of the colloid translation, and follows the stochastic differential equation

$$\dot{\mathbf{e}}(t) = \hat{\boldsymbol{\eta}}(t) \times \mathbf{e}(t), \quad (1.76)$$

with the Gaussian and Markovian stochastic process  $\hat{\boldsymbol{\eta}}$  of zero mean and the second moment,

$$\langle \hat{\eta}_\alpha(t) \hat{\eta}_\beta(t') \rangle = 2D_R \delta_{\alpha\beta} \delta(t - t'), \quad (1.77)$$

where  $D_R$  is the rotational diffusion coefficient. The correlation function for the rotational diffusion of  $\mathbf{v}(t)$  reads [122]

$$\langle \mathbf{v}(t) \cdot \mathbf{v}(t') \rangle = v_0^2 e^{-(d-1)D_R|t-t'|}, \quad (1.78)$$

with  $d$  denoting the spatial dimension. The correlation function (1.78) can be also derived from the differential equation of the active velocity  $\mathbf{v}$  [1, 8, 86],

$$\dot{\mathbf{v}}(t) = -\gamma_R \mathbf{v}(t) + \hat{\boldsymbol{\eta}}(t), \quad (1.79)$$

with the damping factor  $\gamma_R = (d-1)D_R$ . Here, the second moment of random process is

$$\langle \hat{\eta}_\alpha(t) \hat{\eta}_\beta(t') \rangle = \frac{2(d-1)}{d} D_R v_0^2 \delta_{\alpha\beta} \delta(t - t'). \quad (1.80)$$

The set of equations (1.73) and (1.79) is typically referred to literature as an Active-Ornstein-Uhlenbeck Process (AOUP) [123].

In Brownian dynamics simulations, the inertia equation of motion (1.72), and also the overdamped equation (1.73), are solved via the Ermak-McCammon scheme

[101, 102, 124]. The solution of the equation of motion for the rotation of the orientation vector  $\mathbf{e}$  is obtained as follows.[125, 126] We can interpret the motion of  $\mathbf{e}$  as a random walk on the surface of a unity radius sphere. Thus, the corresponding time discretization in the integration time interval  $\Delta t$  is

$$\mathbf{e}'(t + \Delta t) = \mathbf{e}(t) + \mathbf{e}_\theta(t)\Delta\hat{\eta}_\theta + \mathbf{e}_\phi(t)\Delta\tilde{\eta}_\phi, \quad (1.81)$$

where  $\mathbf{e}_\xi \sim \partial\mathbf{e}/\partial\xi$  ( $\xi \in \{\phi, \theta\}$ ) are the unit vectors which follow from Eq. (1.71). The stochastic variables  $\Delta\hat{\eta}_\xi$  ( $\xi \in \{\Phi, \theta\}$ ) are Gaussian and Markovian processes with zero mean and the second moments

$$\langle \Delta\hat{\eta}_\xi \Delta\hat{\eta}_{\xi'} \rangle = 2D_R \delta_{\xi\xi'} \Delta t. \quad (1.82)$$

After normalization, the vector  $\mathbf{e}(t + \Delta t)$  yields

$$\mathbf{e}(t + \Delta t) = \mathbf{e}'(t + \Delta t) / |\mathbf{e}'(t + \Delta t)|. \quad (1.83)$$

### 1.4.2 Active Brownian polymer (ABPO)

A semiflexible active polymer is composed of  $N_m$  active Brownian particles (cf. Fig. 1.3) [67, 117], which obey the equations of motion ( $i = 1, \dots, N_m$ )

$$\dot{\mathbf{r}}_i(t) = v_0 \mathbf{e}_i(t) + \frac{1}{\gamma} [\mathbf{F}_i(t) + \mathbf{I}_i(t)], \quad (1.84)$$

$$\dot{\mathbf{e}}_i(t) = \hat{\boldsymbol{\eta}}_i(t) \times \mathbf{e}_i(t). \quad (1.85)$$

The forces  $\mathbf{F}_i(t) = -\nabla_{\mathbf{r}_i}(U_l + U_b + U_{LJ})$  following from the bond ( $U_l$ ), bending ( $U_b$ ), and volume exclusion ( $U_{LJ}$ ) potentials, [117]

$$U_l = \frac{\kappa_l}{2} \sum_{i=2}^{N_m} (|\mathbf{R}_i| - l)^2, \quad (1.86)$$

$$U_b = \frac{\kappa_b}{2} \sum_{i=2}^{N_m-1} (\mathbf{R}_{i+1} - \mathbf{R}_i)^2, \quad (1.87)$$

$$U_{LJ} = \begin{cases} 4\epsilon \sum_{i<j} \left[ \left( \frac{\sigma}{r_{ij}} \right)^{12} - \left( \frac{\sigma}{r_{ij}} \right)^6 + \frac{1}{4} \right], & r_{ij} < \sqrt[6]{2}\sigma \\ 0, & r_{ij} > \sqrt[6]{2}\sigma \end{cases}, \quad (1.88)$$

where  $\mathbf{R}_{i+1} = \mathbf{r}_{i+1} - \mathbf{r}_i$  is the bond vector,  $\mathbf{r}_{ij} = \mathbf{r}_i - \mathbf{r}_j$  the vector between monomers  $i$  and  $j$ , and  $r_{ij} = |\mathbf{r}_{ij}|$ . The energy  $\epsilon$  measures the strength of the purely repulsive potential, and  $\sigma$  is the diameter of a monomer.  $\mathbf{I}_i$  and  $\hat{\boldsymbol{\eta}}_i$  are Gaussian and Markovian

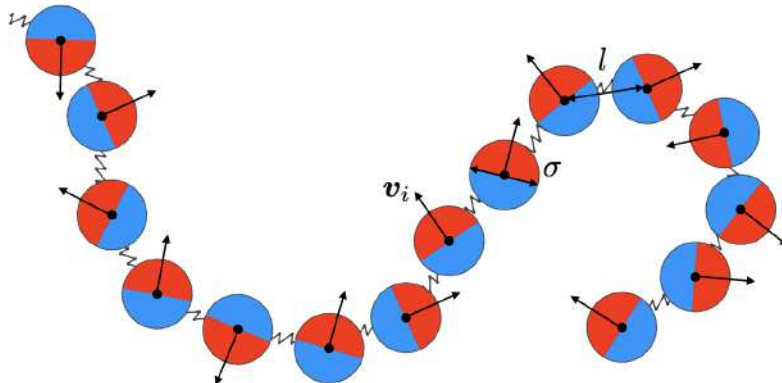


Fig. 1.3 illustration of an active Brownian polymer (ABPO), where the monomers are represented by blue-red ABPs, in a passive environment (white noise). The black arrows represent the independent active velocities  $\mathbf{v}_i$ ,  $\sigma$  is the diameter of the particles and  $l$  the bond-length between two ABPs.

stochastic processes with zero mean and the second moments defined in Eqs. (1.75) and (1.82). Here,  $\kappa_l$  and  $\kappa_b$  are the bonding and bending constants, respectively.

As for the ABP model, the translational equations of motion (1.84) are solved via the Ermark-McCammon algorithm. [101, 102] The selection of equations of motion (1.85) for the orientation vectors are given by Eqs. (1.81) and (1.82).

We characterize activity by the Péclet number  $Pe$  and the ratio  $\Delta$  between translational,  $D_T = k_B T / \gamma$ , and rotational,  $D_R$ , diffusion coefficient of an isolated monomer, where

$$Pe = \frac{v_0}{lD_R}, \quad \Delta = \frac{D_T}{l^2 D_R}. \quad (1.89)$$

The coefficient  $\kappa_l$  (Eq. (1.86)) for the bond strength is adjusted according to the applied Péclet number, in order to avoid bond stretching with increasing activity. By choosing  $\tilde{\kappa}_l = \kappa_l l^2 / k_B T \propto Pe$ , bond-length variations are negligible and we ensure the contour length is fixed for all considered activities. Furthermore, the scaled bending force coefficient  $\tilde{\kappa}_b = \kappa_b l^2 / k_B T$  (Eq. (1.87)) is related to the polymer persistence length,  $l_p = 1/(2p)$ , by

$$pL = N_m \frac{\tilde{\kappa}_b (1 - \coth(\tilde{\kappa}_b)) + 1}{\tilde{\kappa}_b (1 + \coth(\tilde{\kappa}_b)) - 1}. \quad (1.90)$$

The parameters of the truncated and shifted Lennard-Jones potential are  $\sigma = 0.8l$  and  $\epsilon = k_B T$ .

### 1.4.3 Continuous gaussian active semiflexible polymer (GASFP)

For the analytical treatment of the polymers, the mean-field model for a continuous Gaussian semiflexible polymer, denoted in literature as Gaussian semiflexible polymer (GSFP) model, is adopted [89, 90, 127–130]. We consider the polymer as a differentiable space curve  $\mathbf{r}(s, t)$  of contour length  $L$ , with contour coordinate  $s$  ( $-L/2 \leq s \leq L/2$ ) at time  $t$ . The overdamped equation of motion is then given by the Langevin equation [120, 131]

$$\gamma \frac{\partial \mathbf{r}(s, t)}{\partial t} = 2\nu k_B T \frac{\partial^2 \mathbf{r}(s, t)}{\partial s^2} - \epsilon k_B T \frac{\partial^4 \mathbf{r}(s, t)}{\partial s^4} + \mathbf{\Gamma}(s, t), \quad (1.91)$$

with the boundary conditions for free ends

$$\begin{aligned} 2\nu \frac{\partial \mathbf{r}(s, t)}{\partial s} - \epsilon \frac{\partial^3 \mathbf{r}(s, t)}{\partial s^3} \Big|_{s=L/2} &= 0, \\ 2\nu \frac{\partial \mathbf{r}(s, t)}{\partial s} - \epsilon \frac{\partial^3 \mathbf{r}(s, t)}{\partial s^3} \Big|_{s=-L/2} &= 0, \\ 2\nu_0 \frac{\partial \mathbf{r}(s, t)}{\partial s} + \epsilon \frac{\partial^2 \mathbf{r}(s, t)}{\partial s^2} \Big|_{s=L/2} &= 0, \\ 2\nu_0 \frac{\partial \mathbf{r}(s, t)}{\partial s} - \epsilon \frac{\partial^2 \mathbf{r}(s, t)}{\partial s^2} \Big|_{s=-L/2} &= 0, \end{aligned} \quad (1.92)$$

where here  $\gamma$  is the translational friction coefficient per unit length. The terms in Eq. (1.91) with the second and fourth derivative capture chain flexibility, i.e., chain entropy, and bending forces, respectively. The Lagrangian multipliers  $\nu(s)$  and  $\nu_0 = \nu(\pm L/2)$  account for the inextensibility of the polymer (we will denote  $\nu$  as stretching coefficient in the following), and  $\epsilon$  characterizes the bending stiffness [87, 90]. For a polymer in three dimensions, previous studies yield  $\epsilon = 3/4p$  and  $\nu_0 = 3/4$ , where  $p = 1/2l_p$  and  $l_p$  is the persistence length [87, 90]. Adopting the mean-field approach, the stretching coefficient  $\nu$  is independent of  $s$  and is determined by the global constraint

$$\int_{-L/2}^{L/2} \left\langle \left( \frac{\partial \mathbf{r}(s)}{\partial s} \right)^2 \right\rangle ds = L. \quad (1.93)$$

The stochastic force  $\mathbf{\Gamma}(s, t)$  is assumed to be stationary, Markovian, and Gaussian [95, 132], with zero mean,  $\langle \mathbf{\Gamma}(s, t) \rangle = 0$ , and the second moments

$$\langle \Gamma_\alpha(s, t) \Gamma_\beta(s', t') \rangle = 2\gamma k_B T \delta_{\alpha\beta} \delta(s - s') \delta(t - t'). \quad (1.94)$$

## Theoretical background

---

In order to study active Brownian polymers, we extend the GSFP-model to the Gaussian active semiflexible polymer (GASFP) model [74, 76, 77, 116, 121], by including an active velocity term into the original equation. In analogy to ABP, activity is introduced by assigning a propulsion velocity  $\mathbf{v}(s, t)$  is assigned to every point  $\mathbf{r}(s, t)$ , which change in an independent manner [1, 2, 8, 118, 133, 134]. The equation of motion for the ABPO is then given by the Langevin equations

$$\frac{\partial \mathbf{r}(s, t)}{\partial t} = \mathbf{v}(s, t) + \frac{1}{\gamma} \left[ 2\nu k_B T \frac{\partial^2 \mathbf{r}(s, t)}{\partial s^2} - \epsilon k_B T \frac{\partial^4 \mathbf{r}(s, t)}{\partial s^4} + \mathbf{\Gamma}(s, t) \right], \quad (1.95)$$

$$\frac{\partial}{\partial t} \mathbf{v}(s, t) = -\gamma_R \mathbf{v}(s, t) + \hat{\boldsymbol{\eta}}(s, t), \quad (1.96)$$

where  $\hat{\boldsymbol{\eta}}(s, t)$  is a Gaussian and Markovian stochastic force with zero mean and the second moments

$$\langle \hat{\eta}_\alpha(s, t) \hat{\eta}_\beta(s', t') \rangle = \frac{d-1}{d} v_0^2 l \gamma_R \delta_{\alpha\beta} \delta(t-t') \delta(s-s'). \quad (1.97)$$

This yields the correlation function [1, 73, 74, 86, 123]

$$\langle \mathbf{v}(s, t) \cdot \mathbf{v}(s', t') \rangle = v_0^2 l e^{-\gamma_R |t-t'|} \delta(s-s'). \quad (1.98)$$

For a spherical colloid in 3-dimensions, the relation  $\gamma_R = 2D_R$  applies. Since only first and second moments of the active velocity are required for the current analytical studies, the results are independent of the underlying active velocity dynamics of an active site—either AOUP or ABP.

In the previous description, the activity is introduced as an intrinsic velocity of the monomers, where the polymer can be considered as comprised of ABPs [66, 72, 86]. However,  $\mathbf{v}$  can also be considered as an external stochastic process with the exponential correlation (1.78) [1, 8, 73, 86]. This correlated noise represents an active bath of colored noise on passive monomers. [6, 45, 67, 68, 71, 122, 133–137]. Both examples are mathematically equivalent and are illustrated in Fig. 1.4.

We introduce the length scale  $l$  in the continuum representation of a semiflexible polymer. Thereby, the ratio  $L/l$  can be interpreted as the number of uniformly distributed active sites along the polymer. In the flexible limit, we set  $p = 1/l$ , which leads to the relation  $pL = L/l$ . The choice  $p = 1/l$  is motivated by discrete bead-spring polymers, typically used in computer simulations [72, 117], where every monomer is an ABP. Since we are working with a touching-bead model, the bead diameter  $\sigma$  and bond-length  $l$  must be equal,  $\sigma = 0.8l$ , and are taken as the minimum length scale

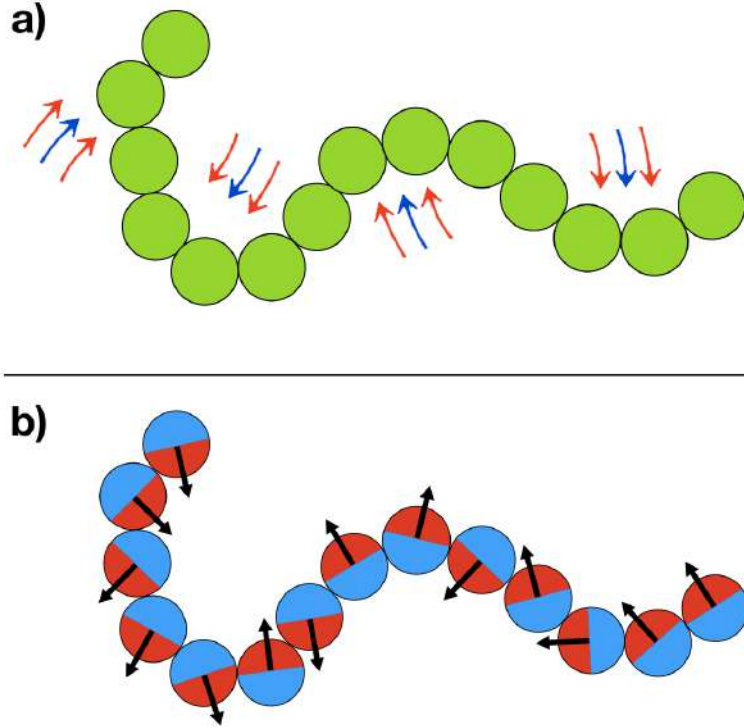


Fig. 1.4 (a) Illustration of a passive polymer comprised by a set of passive monomers (green) surrounded by an active bath pictured with red/blue lines. Such an active environment induces active correlations (colored noise) into the monomers which decay exponentially in time. (b) Illustration of an active Brownian polymer (ABPO), where the monomers are represented by blue-red ABPs, in a passive environment (white noise).

and free parameter in the continuum polymer model. In the flexible case, the length scale  $l$  corresponds to the Kuhn length [138, 139].

To solve Eq. (1.95), a linear inhomogeneous partial differential equation of fourth order, we apply the eigenfunction expansion

$$\mathbf{r}(s, t) = \sum_{n=0}^{\infty} \chi_n(t) \varphi_n(s), \quad (1.99)$$

where  $\chi_n(t)$  and  $\varphi_n(s)$  are the time-dependent amplitudes and the position-dependent eigenfunctions, respectively. The differential equation for the eigenfunction is

$$\epsilon k_B T \frac{d^4}{ds^4} \varphi_n(s) - 2\nu k_B T \frac{d^2}{ds^2} \varphi_n(s) = \xi_n \varphi_n(s). \quad (1.100)$$

## Theoretical background

---

with the eigenvalue  $\chi_n(t)$ . The eigenfunction  $\varphi_n$  of the self-adjoint eigenvalue problem (1.100) form a complete set of orthogonal basis function, which are given by [88, 89, 120, 140]

$$\begin{aligned}\varphi_0 &= \sqrt{1/L} \\ \varphi_n(s) &= \sqrt{\frac{c_n}{L}} \left[ \zeta'_n \frac{\sinh(\zeta'_n s)}{\cosh(\zeta'_n L/2)} + \zeta_n \frac{\sin(\zeta_n s)}{\cos(\zeta_n L/2)} \right], \quad \forall n \quad \text{odd}, \\ \varphi_n(s) &= \sqrt{\frac{c_n}{L}} \left[ \zeta'_n \frac{\cosh(\zeta'_n s)}{\sinh(\zeta'_n L/2)} - \zeta_n \frac{\cos(\zeta_n s)}{\sin(\zeta_n L/2)} \right], \quad \forall n \quad \text{even}.\end{aligned}\tag{1.101}$$

$\varphi_0$  determines the translational motion of the polymer center-of-mass. The set of constants  $c_n$  from Eq. (1.101) are derived from the normalization condition [88, 89, 120]

$$\int_{-L/2}^{L/2} \varphi_n(s) \varphi_m(s) ds = \delta_{nm}.\tag{1.102}$$

From the boundary conditions (1.92), we get the equations for the wave numbers  $\zeta_n$  and  $\zeta'_n$

$$\zeta_n'^2 - \zeta_n^2 = 2\nu/\epsilon,\tag{1.103}$$

$$\begin{aligned}\epsilon \left[ \zeta_n'^3 \sin(\zeta_n L/2) \cosh(\zeta'_n L/2) - \zeta_n'^3 \cos(\zeta_n L/2) \sinh(\zeta'_n L/2) \right] \\ - 2\nu_0 (\zeta_n^2 + \zeta_n'^2) \cos(\zeta_n L/2) \cosh(\zeta'_n L/2) = 0, \quad \forall n \quad \text{odd}\end{aligned}\tag{1.104}$$

$$\begin{aligned}\epsilon \left[ \zeta_n'^3 \cos(\zeta_n L/2) \sinh(\zeta'_n L/2) + \zeta_n'^3 \sin(\zeta_n L/2) \cosh(\zeta'_n L/2) \right] \\ + 2\nu_0 (\zeta_n^2 + \zeta_n'^2) \sin(\zeta_n L/2) \sinh(\zeta'_n L/2) = 0, \quad \forall n \quad \text{even},\end{aligned}\tag{1.105}$$

where the eigenvalues are related to the wave numbers via  $\xi_n = k_B T (\epsilon \zeta_n^4 + 2\nu \zeta_n^2)$ , with the 0-th eigenvalue  $\xi_0 = 0$ .

In the flexible limit, where the persistence length  $l_p \ll L$  (or also  $pL \rightarrow \infty$ ), the eigenvalue equation and eigenfunctions have a much more compact solution. Now, the wave numbers are given by  $\zeta_n = n\pi/L$  and the eigenvalues by  $\xi_n = 2\nu k_B T \zeta_n^2$ . Thus,

the well-known eigenfunctions of the Rouse model are obtained [88, 132, 141],

$$\begin{aligned}\varphi_0 &= \sqrt{\frac{1}{L}}, \\ \varphi_n(s) &= \sqrt{\frac{2}{L}} \sin\left(\frac{n\pi s}{L}\right), \quad \forall n \text{ odd}, \\ \varphi_n(s) &= \sqrt{\frac{2}{L}} \cos\left(\frac{n\pi s}{L}\right), \quad \forall n \text{ even}.\end{aligned}\tag{1.106}$$

The most general solution of (1.95) can be written in terms of an eigenfunction expansion,

$$\mathbf{r}(s, t) = \sum_{n=0}^{\infty} \boldsymbol{\chi}_n(t) \varphi_n(s), \quad \boldsymbol{\Gamma}(s, t) = \sum_{n=0}^{\infty} \boldsymbol{\Gamma}_n(t) \varphi_n(s),\tag{1.107}$$

and for the velocity

$$\mathbf{v}(s, t) = \sum_{n=0}^{\infty} \mathbf{v}_n(t) \varphi_n(s), \quad \hat{\boldsymbol{\eta}}(s, t) = \sum_{n=0}^{\infty} \hat{\boldsymbol{\eta}}_n(t) \varphi_n(s).\tag{1.108}$$

Inserting the eigenfunction expansion (1.107) into the equation of motion (1.95), multiplying with  $\varphi_m$ , integrating over  $\int ds$  and using the orthogonality property of the eigenfunctions yields the Langevin equation for the amplitudes  $\boldsymbol{\chi}_n(t)$  and the active noise  $\mathbf{v}_n(t)$

$$\frac{d}{dt} \boldsymbol{\chi}_n = -\frac{1}{\tau_n} \boldsymbol{\chi}_n + \frac{1}{\gamma} \boldsymbol{\Gamma}_n + \mathbf{v}_n, \quad n > 0; \quad \frac{d}{dt} \boldsymbol{\chi}_0 = \frac{1}{\gamma} \boldsymbol{\Gamma}_0 + \mathbf{v}_{(0)},\tag{1.109}$$

$$\frac{d}{dt} \mathbf{v}_n = -\gamma_R \mathbf{v}_n + \hat{\boldsymbol{\eta}}_n,\tag{1.110}$$

where  $v_{n=0} \equiv v_{(0)}$ , and the relaxation times are given by

$$\tau_n = \frac{\gamma}{\xi_n} = \frac{\gamma}{k_B T (\epsilon \zeta_n^4 + 2\nu \zeta_n^2)}, \quad n > 0; \quad \tau_0 = \infty.\tag{1.111}$$



# Chapter 2

## Active polymer under shear flow

The conformational and rheological properties of active filaments/polymers exposed to shear flow are studied analytically. Using the continuous Gaussian semiflexible polymer model extended by the activity, it is derived the analytical expressions for the dependence of the deformation, orientation, relaxation times, and viscosity on the persistence length, shear rate, and activity. The model yields a Weissenberg-number dependent shear-induced deformation, alignment, and shear thinning behavior, similarly to the passive counterpart. Thereby, the model shows an intimate coupling between activity and shear flow. As a consequence, activity enhances the shear-induced polymer deformation for flexible polymers. For semiflexible polymers/filaments, a nonmonotonic deformation is obtained because of the activity-induced shrinkage at moderate and swelling at large activities. Independent of stiffness, activity-induced swelling facilitates and enhances alignment and shear thinning compared to a passive polymer. In the asymptotic limit of large activities, a polymer length- and stiffness-independent behavior is obtained, with universal shear-rate dependencies for the conformations, dynamics, and rheology.

### 2.1 Model

#### 2.1.1 Equation of motion

The filament/polymer is described by the Gaussian semiflexible polymer model introduced in Sec.(1.1.3). Thereby, the polymer of length  $L$  is considered as a continuous, differentiable space curve  $\mathbf{r}(s, t)$ , with the contour coordinate  $s$  ( $-L/2 \leq s \leq L/2$ ), and the time  $t$ . The activity is introduced by assigning an active velocity  $\mathbf{v}(s, t)$  to every point  $\mathbf{r}(s, t)$  (cf. Fig. 2.1). The equation of motion of  $\mathbf{r}(s, t)$  is then given

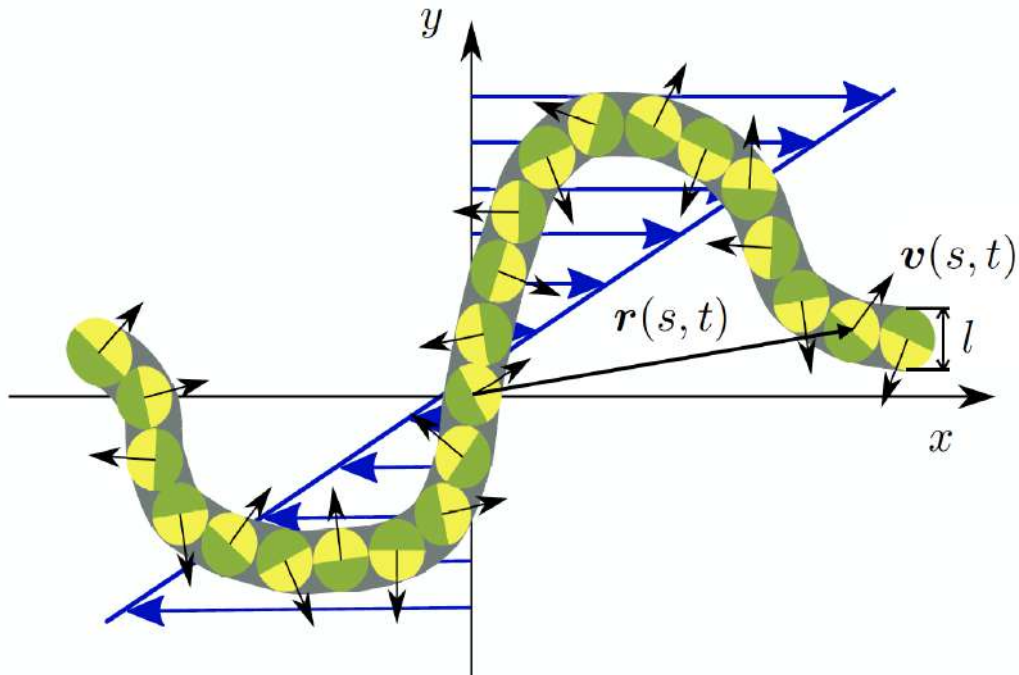


Fig. 2.1 Illustration of the continuous semiflexible active polymer (ABPO) in shear flow. The arrows and colors indicate the orientation of the active velocity  $\mathbf{v}(s, t)$ .

by [74, 76]

$$\frac{\partial}{\partial t} \mathbf{r}(s, t) = \mathbf{v}(s, t) + \frac{k_B T}{\gamma} \left( 2\lambda \frac{\partial^2}{\partial s^2} \mathbf{r}(s, t) - \epsilon \frac{\partial^4}{\partial s^4} \mathbf{r}(s, t) \right) + \frac{1}{\gamma} \mathbf{\Gamma}(s, t) + \mathbf{K} \mathbf{r}(s, t), \quad (2.1)$$

with the boundary conditions of Eq. (1.92). The terms with the second and fourth derivative in Equation (2.1) account for the entropy elasticity and bending stiffness, respectively,  $\mathbf{\Gamma}$  for thermal fluctuations, and  $\mathbf{K} \mathbf{r}(s, t)$  for the shear flow, with the shear-rate tensor  $\mathbf{K}$ . The Lagrangian multipliers  $\lambda_0 = \lambda(\pm L/2)$ ,  $\lambda(s)$ , and  $\epsilon$  are determined by constraints [87, 90]. In general, this yields  $\epsilon = 3/4p$  and  $\lambda_0 = 3/4$  for a polymer in three dimensions, where  $p = 1/2l_p$  in terms of the persistence length  $l_p$  [89, 90]. The Lagrangian multiplier  $\lambda$ , denoted as stretching coefficient, is determined in a mean-field manner via the global constraint of Eq. (1.93). [74, 89, 90]

As discussed in Sec. (1.4.3), the active velocity  $\mathbf{v}(s, t)$  can be considered as external colored noise experienced by the respective polymer site, the picture adopted here, or as intrinsic polymer property originating from self-propulsion. For an identical mathematical formulation, the active site has then to be described by an active Ornstein–Uhlenbeck particle (AOUP) [123, 125]. However, also an ABP can be con-

sidered, as long as only second moments of the active velocity correlation function are relevant [117]. In any case, the active velocity is described by a diffusive process—Brownian motion—either for the propulsion direction only (ABPs) [1, 2, 8, 118, 133, 134], or for the individual Cartesian components, i.e., the magnitude of  $\mathbf{v}$  is changing too (AOUPs) [1, 74, 123, 125]. Independent of the details of the underlying stochastic (active) processes, we denote our polymer as active Brownian Polymer (ABPO). Hence, the active velocity,  $\mathbf{v}(s, t)$ , is described by a non-Markovian, but Gaussian stochastic process with zero mean and the second moments [74, 76, 125]

$$\langle v_\alpha(s, t)v_\beta(s', t') \rangle = \frac{v_0^2 l}{3} e^{-\gamma_R |t-t'|} \delta(s-s') \delta_{\alpha\beta}, \quad (2.2)$$

i.e., the polymer is exposed to colored noise [74, 76, 125]. Here,  $v_0$  is the propulsion velocity, the damping factor  $\gamma_R$  can be related to the rotational diffusion coefficient  $D_R$  of a spherical colloid in three dimensions via  $\gamma_R = 2D_R$ , and  $\alpha, \beta \in \{x, y, z\}$ . The stochastic process  $\mathbf{r}(s, t)$  of the translational motion is assumed to be stationary, Markovian, and Gaussian with zero mean and the second moments

$$\langle \Gamma_\alpha(s, t)\Gamma_\beta(s', t') \rangle = 2\gamma k_B T \delta_{\alpha\beta} \delta(s-s') \delta(t-t'), \quad (2.3)$$

where  $T$  is the temperature,  $k_B$  the Boltzmann constant, and  $\gamma$  the translational friction coefficient per length. The latter is related with the translational, thermal diffusion coefficient  $D_T$  via  $D_T = k_B T / \gamma l$ . Finally, shear is applied along the  $x$ -direction and the gradient along the  $y$ -direction of the Cartesian reference frame. Hence, the shear-rate tensor is given by  $K_{xy} = \dot{\gamma}$ , where  $\dot{\gamma}$  is the shear rate.

### 2.1.2 Eigenfunction expansion

The linear equation of motion (2.1) is solved by the eigenfunction expansion

$$\mathbf{r}(s, t) = \sum_{n=0}^{\infty} \chi_n(t) \varphi_n(s) \quad (2.4)$$

and an analogous representation of  $\mathbf{v}$  and  $\mathbf{r}$  shown in Eq. (1.107) and (1.108), in terms of the eigenfunctions  $\varphi_n$  of the eigenvalue equation [74, 88]

$$\epsilon k_B T \frac{\partial^4}{\partial s^4} \varphi_n(s) - 2\lambda k_B T \frac{\partial^2}{\partial s^2} \varphi_n(s) = \xi_n \varphi_n(s), \quad (2.5)$$

which gives exactly the same solution as for the eigenfunctions in Eq. (1.101). As mentioned in Sec. (1.4.3), the eigenfunction  $\varphi_0$  accounts for the polymer's center of mass

motion, the  $c_n$ s are normalization coefficients, and the wave numbers are determined by the boundary conditions of Eq. (1.92).

Insertion of the eigenfunction expansion for  $\mathbf{r}(s, t)$  from Eq. (2.4) into the equation of motion from Eq. (2.1) yields the new equation of motion for the mode amplitudes  $\chi_n$ ,

$$\frac{\partial}{\partial t}\chi_{n\alpha}(t) = -\frac{1}{\tau_n}\chi_{n\alpha}(t) + v_{n\alpha}(t) + \frac{1}{\gamma}\Gamma_{n\alpha}(t) + \dot{\gamma}\chi_{ny}\delta_{x\alpha}, \quad (2.6)$$

with respective amplitudes  $\mathbf{v}_n(t)$  and  $\mathbf{\Gamma}_n(t)$  of the active velocity and stochastic force, and the relaxation times ( $n > 0$ )

$$\tau_n = \frac{\gamma}{\xi_n} = \frac{\gamma}{k_B T(\epsilon\zeta_n^4 + 2\lambda\zeta_n^2)}. \quad (2.7)$$

The stationary-state solution of Equation (2.6) for  $n > 0$  is

$$\chi_{n\alpha}(t) = \int_{-\infty}^t dt' e^{-(t-t')/\tau_n} [v_{n\alpha}(t') + \Gamma_{n\alpha}(t') + \dot{\gamma}\chi_{ny}(t')\delta_{x\alpha}], \quad (2.8)$$

and for the polymer center of mass motion ( $n = 0$ ),

$$\chi_{0\alpha}(t) = \chi_{0\alpha}(0) + \int_0^t dt' [v_{0\alpha}(t') + \Gamma_{0\alpha}(t') + \dot{\gamma}\chi_{0y}(t')\delta_{x\alpha}]. \quad (2.9)$$

### 2.1.3 Mode–amplitude correlation functions

The time correlation functions of the mode amplitudes can be calculated straightforwardly by Equation (2.8), which yields  $\langle \chi_n(t) \cdot \chi_m(t') \rangle = \delta_{nm} \langle \chi_n(t) \cdot \chi_n(t') \rangle$ , with ( $n > 0, t \geq 0$ )

$$\langle \chi_{ny}(t)\chi_{ny}(0) \rangle = \langle \chi_{nz}(t)\chi_{nz}(0) \rangle = \left( \frac{k_B T \tau_n}{\gamma} - \frac{v_0^2 l \gamma_R \tau_n^3}{3(1 - (\gamma_R \tau_n)^2)} \right) e^{-t/\tau_n} + \frac{v_0^2 l \tau_n^2}{3(1 - (\gamma_R \tau_n)^2)} e^{-\gamma_R t}, \quad (2.10)$$

$$\begin{aligned} \langle \chi_{nx}(t)\chi_{nx}(0) \rangle &= \langle \chi_{ny}(t)\chi_{ny}(0) \rangle + \frac{\dot{\gamma}^2 v_0^2 l \tau_n^4}{3(1 - (\gamma_R \tau_n)^2)^2} e^{-\gamma_R t} \\ &+ \left[ \frac{\dot{\gamma}^2 \tau_n^2}{2} \left( \frac{k_B T \tau_n}{\gamma} - \frac{v_0^2 l \gamma_R \tau_n^3}{3(1 - (\gamma_R \tau_n)^2)} \right) \left( 1 + \frac{t}{\tau_n} \right) - \frac{\dot{\gamma}^2 \gamma_R v_0^2 l \tau_n^5}{3(1 - (\gamma_R \tau_n)^2)^2} \right] e^{-t/\tau_n}, \end{aligned} \quad (2.11)$$

$$\begin{aligned} \langle \chi_{nx}(t)\chi_{ny}(0) \rangle &= \frac{\dot{\gamma}v_0^2 l \tau_n^3}{3(1 - (\gamma_R \tau_n)^2)(1 - \gamma_R \tau_n)} e^{-\gamma_R t} \\ &+ \left[ \frac{\dot{\gamma} \tau_n}{2} \left( \frac{k_B T \tau_n}{\gamma} - \frac{v_0^2 l \gamma_R \tau_n^3}{3(1 - (\gamma_R \tau_n)^2)} \right) \left( 1 + \frac{2t}{\tau_n} \right) - \frac{2\dot{\gamma} \gamma_R v_0^2 l \tau_n^4}{3(1 - (\gamma_R \tau_n)^2)^2} \right] e^{-t/\tau_n}. \end{aligned} \quad (2.12)$$

### 2.1.4 Inextensibility and stretching coefficient $\lambda$

The inextensibility constraint (1.93), together with the eigenfunction expansion and the correlation functions (2.10)–(2.12), leads to the equation

$$\sum_{n=1}^{\infty} \langle \boldsymbol{\chi}_n^2 \rangle \phi_n = 1 \quad (2.13)$$

to determine  $\lambda$ , where  $\phi_n = \int_{-L/2}^{L/2} (\partial \varphi_n(s)/\partial s)^2 ds/L$  and

$$\langle \boldsymbol{\chi}_n^2 \rangle = \frac{3k_B T}{\gamma} \tau_n + \frac{v_0^2 l}{1 + \gamma_R \tau_n} \tau_n^2 + \dot{\gamma}^2 \frac{k_B T}{2\gamma} \tau_n^3 + \dot{\gamma}^2 \frac{v_0^2 l (2 + \gamma_R \tau_n)}{6(1 + \gamma_R \tau_n)^2} \tau_n^4. \quad (2.14)$$

In general, Equation (2.13) has to be solved numerically. However, the sum over the mode numbers can be evaluated in the limit  $pL \rightarrow \infty$ , or even for moderate  $pL$ , for larger activities  $Pe \gg 1$  [76], due to the dominance of the stretching modes in these limits, i.e.,  $\zeta_n = n\pi/L$  and  $\tau_n = \gamma L^2/3k_B T \pi^2 p \mu n^2 = \tau_R/\mu n^2$ , where  $\tau_R = \gamma L^2/3k_B T \pi^2 p$  is the Rouse relaxation time of the passive polymer [88, 132]. Here, the Péclet number  $Pe$  and other relevant dimensionless quantities, such as the Weissenberg number  $Wi$ , the ratio between the translational and rotational diffusion coefficient  $\Delta$ , and the scaled stretching coefficient  $\mu$ , in terms of the value at equilibrium,  $3p/2$ , are introduced as

$$Pe = \frac{v_0}{D_R l}, \quad Wi = \dot{\gamma} \tau_0, \quad \Delta = \frac{D_T}{l^2 D_R}, \quad \mu = \frac{2\lambda}{3p}. \quad (2.15)$$

Thereby,  $\tau_0 = \tau_1(Pe, Wi = 0)$  is the longest polymer relaxation time at zero shear but in the presence of activity. Combined with results from Refs [74, 142], we find

from Equation (2.13)

$$\begin{aligned} \frac{1}{\sqrt{\mu}} \coth(2pL\sqrt{\mu}) - \frac{1}{2pL\mu} + \frac{Pe^2}{6\mu\Delta} \left[ \sqrt{\frac{\mu}{1+6\mu^2p^3l^3\Delta}} \coth\left(2pL\sqrt{\frac{\mu}{1+6\mu^2p^3l^3\Delta}}\right) - \frac{1}{2pL} \right] \\ + \frac{Wi^2\pi^4\mu_0^2}{540pL\mu^3} + \frac{Wi^2Pe^2L^3(2+2L^3/3\pi^2l^3\Delta pL\mu)}{54\pi^2\Delta^2(pL)^2l^3(1+2L^3/3\pi^2l^3\Delta pL\mu)^2}\mu^2 = 1, \end{aligned} \quad (2.16)$$

where for the evaluation of the term proportional to  $Wi^2Pe^2 \sim \dot{\gamma}^2v_0^2$  only the first mode,  $n = 1$ , has been taken into account; the deviation to the full sum is below 3% for all  $Pe, pL$ , and  $Wi$ . The last term on the left-hand side reflects the coupling between activity and shear flow.

The following asymptotic dependencies for the stretching coefficient  $\mu$  are obtained:

(i) Passive semiflexible polymer in shear flow, i.e.,  $Pe = 0$  (for details, cf. Ref. [142])

– For  $pL \gg 1$  and  $\mu \gg 1$

$$\mu^3 - \mu^{5/2} - \frac{\pi^4 Wi^2}{540pL} = 0, \quad \xrightarrow{Wi \gg 1} \mu = Wi^{2/3} \left( \frac{\pi^4}{540pL} \right)^{1/3}, \quad (2.17)$$

– For  $pL < 1$  and  $\mu \gg 1$

$$\mu = \frac{Wi^{2/3}}{pL} \left( \frac{4}{15} \right)^{1/3}. \quad (2.18)$$

(ii) Active flexible polymer at weak shear flow, i.e.,  $Wi \ll 1$ ,  $pL \gg 1$ , and  $\tau_n = \tau_R/\mu_0 n^2$  [74, 76]. For later use, we denote the Lagrangian multiplier at  $Wi = 0$  and  $Pe > 0$  by  $\mu_0$

– For  $1 \ll Pe < \infty$  and  $\mu_0 \rightarrow \infty$

$$\mu_0 = \frac{Pe^{4/3}}{pL} \frac{L}{6l\Delta}, \quad (2.19)$$

– For  $Pe \rightarrow \infty$ , i.e.,  $\mu_0 \rightarrow \infty$

$$\mu_0 = \frac{Pe}{pL\Delta} \sqrt{\frac{L^3}{54l^3}}. \quad (2.20)$$

(iii) Active flexible polymer in shear flow,  $\tau_n = \tau_R/\mu n^2$ ,

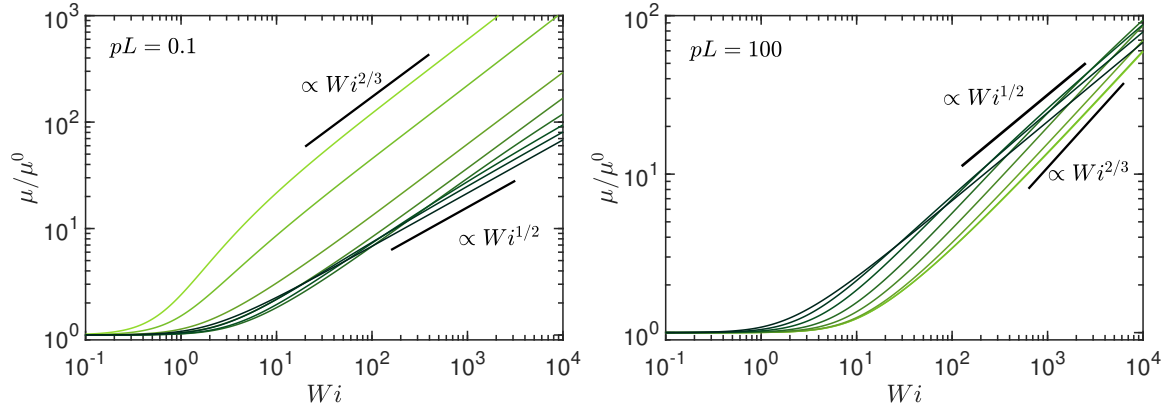


Fig. 2.2 Stretching coefficient  $\mu = 2\lambda/3p$  normalized by the value  $\mu_0$  of the active, non-sheared system as function of the Weissenberg number  $Wi$  for the Péclet numbers  $Pe = 0, 0.6, 3, 10, 30, 10^2, 3 \times 10^2, \text{ and } \infty$  (bright to dark color); (**left**)  $pL = L/2l_p = 0.1$  (stiff) and (**right**)  $pL = 10^2$  (flexible polymer). The number of active sites is  $L/l = 10^2$  and the diffusion coefficient ratio  $\Delta = 0.3$ .

- For  $1 < Pe, Wi < \infty, L^3/3\pi l^3 pL\Delta\mu \gg 1$ , and  $pL \gg 1$  (with Equation (2.19))

$$\mu = Wi^{2/3} \mu_0^{2/3} \left( \frac{Pe^2}{36\Delta pL} \right)^{1/3} = Wi^{2/3} \frac{Pe^{14/9}}{pL\Delta} \left( \frac{L}{36l} \right)^{2/3}, \quad (2.21)$$

- For  $Pe \rightarrow \infty$ , i.e.,  $\mu_0 = Pe\sqrt{L^3/54l^3}/pL\Delta \rightarrow \infty$

$$\mu = \mu_0 \frac{1}{\sqrt{2}} \sqrt{1 + \sqrt{1 + \frac{8Wi^2}{\pi^2}}} \xrightarrow{Wi \gg 1} Wi^{1/2} \frac{Pe}{pL\Delta} \sqrt{\frac{\sqrt{2}L^3}{54\pi l^3}}. \quad (2.22)$$

Hence, in the limit  $Wi \rightarrow \infty$ ,  $\mu$  exhibits a crossover from a  $\mu \sim Wi^{2/3}$  dependence for  $1 \ll Pe < \infty$  to a dependence  $\mu \sim Wi^{1/2}$  for  $Pe \rightarrow \infty$ . The latter characteristics are different from the passive case and are a consequence of the coupling between activity and shear flow.

The full numerical solution for the stretching coefficient  $\mu$  is presented in Figure 2.2 as a function of the Weissenberg number and for various activities. We set  $L/l = 10^2$  for the number of active sites. Hence, when changing  $pL$ , we change the persistence length  $l_p = 1/2p$  at a fixed contour length in order to maintain the active-site density. As illustrated for  $pL = 0.1$  and  $pL = 10^2$ ,  $\mu$  exhibits a crossover from a dependence  $\mu \sim Wi^{2/3}$  at low  $Pe$  to the relation  $\mu \sim Wi^{1/2}$  for  $Pe \rightarrow \infty$  and sufficiently large  $Wi$ , in agreement with the theoretical limits, Equations (2.21) and (2.22). It must be

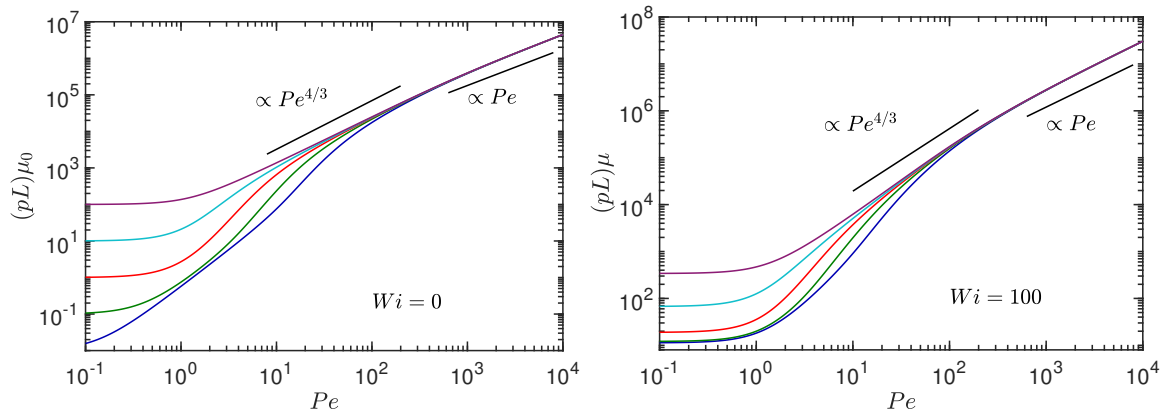


Fig. 2.3 Stretching coefficient  $\mu = 2\lambda/3p$  as a function of the Péclet number  $Pe$  for the stiffness  $pL = 10^{-2}, 10^{-1}, 10^0, 10^1,$  and  $10^2$  (bottom to top). The Weissenberg numbers are (**left**)  $Wi = 0$  [74] and (**right**)  $Wi = 10^2$ . The number of active sites is  $L/l = 10^2$  and  $\Delta = 0.3$ .

emphasized that  $\mu/\mu_0$  approaches the asymptotic dependence

$$\frac{\mu}{\mu_0} = \sqrt{Wi} \sqrt{\frac{\sqrt{2}}{\pi}} \quad (2.23)$$

for  $Pe \gg 1$ . Hence, a universal, activity- and  $pL$ -independent behavior is predicted. For completeness, Figure 2.3 illustrates the dependence of  $\mu$  on the Péclet number for the Weissenberg numbers  $Wi = 0$  (left) and  $Wi = 10^2$  (right). The predicted power-law dependencies (Eq. (2.19) for  $Wi < 1$ , and Eq. (2.22) for  $Pe \gg 1$  and  $Wi \ll Pe$ ) and scaling with respect to  $pL$  are recovered. Figure 2.2 shows a shift of the crossover from the  $Wi^{2/3}$  to the  $Wi^{1/2}$  dependence towards smaller  $Wi$  with increasing  $Pe$ . This crossover strongly depends on  $L/l$ , and shifts to larger  $Wi$  with increasing  $L/l$ . Hence, for a larger number of active sites, no crossover could be observed anymore for suitable Weissenberg numbers. On the contrary, for a smaller number  $L/l$ , the crossover appears already at smaller  $Wi$ . In the extreme case of  $L/l \rightarrow 1$ , a behavior similar to an active dumbbell in shear flow appears [86].

## 2.2 Dynamics and conformations

### 2.2.1 Relaxation times

The relaxation times (2.7) depend on the shear rate ( $Wi$ ), activity ( $Pe$ ), and persistence length ( $p$ ) via the stretching coefficient  $\lambda = 2\mu/3p$ . In the limit of a highly flexible polymer, the relaxation time is  $\tau_n = \tau_R/(\mu n^2)$ . Hence, the mode-number dependence of  $\tau_n$  is unaffected by the nonequilibrium character of the dynamics. However, the

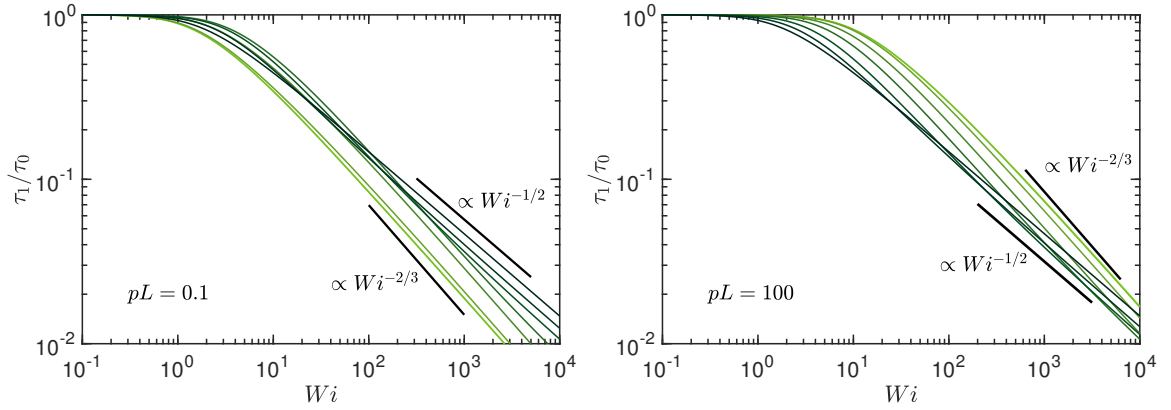


Fig. 2.4 Longest polymer relaxation time  $\tau_1$  normalized by the longest relaxation time  $\tau_0$  of the active, non-sheared system ( $Wi = 0$ ) as function of the Weissenberg number  $Wi$  for the Péclet numbers  $Pe = 0, 0.6, 3, 10, 30, 10^2, 3 \times 10^2$ , and  $\infty$  (bright to dark color); **(left)**  $pL = 0.1$  and **(right)**  $pL = 10^2$ . The number of active sites is  $L/l = 10^2$  and  $\Delta = 0.3$ .

presence of  $\mu$  indicates the fundamental importance to account for the inextensibility of the polymer. Since  $\mu \geq 1$  is a monotonically increasing function of  $Pe$  and  $Wi$ , activity and shear flow always accelerate the relaxation process and the relaxation times become shorter [76, 143].

Figure 2.4 displays the numerically obtained longest relaxation time as a function of the Weissenberg number for various  $Pe$  and the stiffness  $pL = 0.1$  (stiff) and  $pL = 10^2$  (flexible polymer). For  $pL \ll 1$  and small Péclet numbers ( $Pe \lesssim 1$ ), the relaxation time  $\tau_1$ , corresponding to the rotation relaxation time of a rigid polymer, dominates over all other (bending) relaxation times [76, 88]. Hence, the relaxation times of Figure 2.4 (left) are not simply proportional to  $\mu^{-1}$  in this limit. However, with increasing  $Pe$ , bending contributions gradually vanish and the asymptotic dependence  $\tau_1/\tau_0 = \mu_0/\mu$  is assumed. According to Equation (2.23), the ratio  $\tau_1/\tau_0$  is then independent of  $Pe$  and  $pL$ . In Figure 2.4 (right) for flexible polymers, bending modes are negligibly small and the relation  $\tau_1 \sim 1/\mu$  applies for all  $Pe$ . Consequently,  $\tau_1$  exhibits the power-law dependencies of Equations (2.17), (2.21), and (2.22).

It must be emphasized that the shear-rate dependency  $\tau_1 \sim 1/\sqrt{Wi}$  is a consequence of the activity of the polymer and emerges from the coupling of activity and shear (cf. Equation (2.16)). The passive polymer under shear exhibits the dependence  $\tau_1 \sim Wi^{-2/3}$ , which we find for small  $Pe$  also for the active polymer. A dumbbell of active monomers exhibits a similar coupling of activity and shear and, correspondingly, shows a comparable crossover of the relaxation times [142].

Figure 2.5 illustrates the mode-number dependence of the relaxation times for various activities and shear rates. For semiflexible polymers, activity and shear flow modify the relaxation behavior because stretching modes ( $n^2$ ) dominate over bending

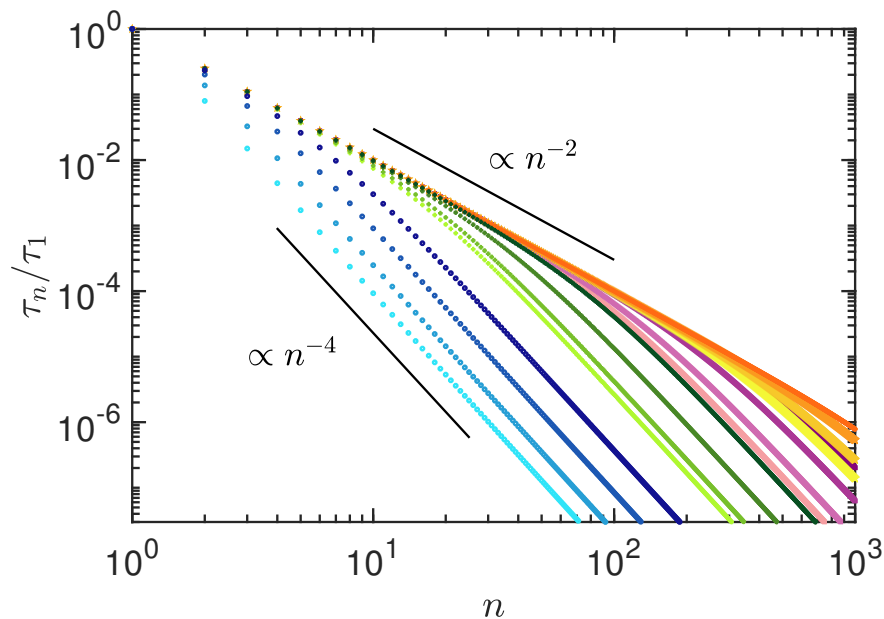


Fig. 2.5 Mode-number dependence of the relaxation times  $\tau_n$  normalized by the longest relaxation time  $\tau_1$  for the Péclet numbers  $Pe = 0, 10^1, 10^2,$  and  $10^3$  (different colors and symbols; from left to right), and the Weissenberg numbers  $Wi = 0, 10^1, 10^2,$  and  $10^3$  (different tone, bright to dark, for every color). The persistence length is  $pL = 1$  and  $L/l = 10^2$ .

modes ( $n^4$ ) with increasing activity and flow strength. Bending stiffness remains dominant at larger mode numbers. Activity as well as flow induce a transition from semiflexible to flexible polymer behavior, which extends to smaller and smaller length scales with increasing  $Pe$  and  $Wi$ .

## 2.2.2 Radius of gyration

The polymer conformations are characterized by the radius of gyration tensor  $\mathbf{G}$ , with the components

$$G_{\alpha\beta} = \frac{1}{L} \int_{-L/2}^{L/2} \langle (r_\alpha(s) - r_{cm\alpha})(r_\beta(s) - r_{cm\beta}) \rangle ds, \quad (2.24)$$

where  $\mathbf{r}_{cm}$  is the center-of-mass position of the polymer. Insertion of the eigenfunction expansion (2.4) yields

$$G_{\alpha\beta} = \frac{1}{L} \sum_{n=1}^{\infty} \langle \chi_{n\alpha}(t) \chi_{n\beta}(t) \rangle \quad (2.25)$$

in terms of the mode-amplitude correlation functions  $\langle \chi_{n\alpha} \chi_{n\beta} \rangle$  (Equations (2.10)–(2.12)).

Figure 2.6 depicts the radius of gyration-tensor component  $G_{xx}$  along the flow direction for rather stiff ( $pL = 0.1$ ) and highly flexible ( $pL = 10^2$ ) polymers. Note that only the excess deformation due to shear is shown. Activity leads to additional conformational changes, which are included in  $G_{xx}^0 = G_{xx}(Wi = 0)$ . As for passive semiflexible polymers, shear leads to an extension and alignment along the flow direction, which saturates at large shear rates because of the finite polymer contour length [142, 144]. The actual asymptotic stretching for  $Wi \rightarrow \infty$  depends on the activity. At  $pL \gg 1$ , the asymptotic limits are  $G_{xx}^\infty/G_{xx}^0 = 12pL/7$  for  $Pe = 0$  [142], and  $G_{xx}^\infty = L^2\pi^6/9450$ ,  $G_{xx}^0 = L^2/45$ , hence  $G_{xx}^\infty/G_{xx}^0 = \pi^6/210$  for  $Pe \rightarrow \infty$ . It is noteworthy that the latter limit is independent of  $pL$ , i.e., it applies for every stiffness, and the same asymptotic behavior is displayed in Figure 2.6 (left) and (right). Shear flow leads to an additional stretching of the active polymer, particularly for  $Pe \rightarrow \infty$ , and not simply to an orientational alignment as for a rod, where  $G_{xx}^\infty/G_{xx}^0 = 3$  for  $Wi \gg 1$  [142], since  $\pi^6/210 \approx 4.6 > 3$ . However, the difference of the asymptotic values for  $Pe = 0$  and  $Pe \rightarrow \infty$ , respectively, can be substantial, since  $G_{xx}^\infty$  of the passive system depends on polymer length. The polymer pre-stretching by activity reduces the possible stretching by shear. The asymptotic limits for  $pL \rightarrow 0$  at  $Pe = 0$  are  $G_{xx}^\infty = 10L^2/105$  and  $G_{xx}^0 = L^2/36$ , hence,  $G_{xx}^\infty/G_{xx}^0 = 24/7$ , in agreement with Figure 2.6 (left). Note that  $G_{xx}/G_{xx}^0$  depends non-monotonically on the Péclet number at small  $pL$ . The ratio  $G_{xx}/G_{xx}^0$  increases with increasing  $Pe$  at small  $Pe$  and decreases again for  $Pe \gg 1$  (cf. Figure 2.6 (left)). In contrast,  $G_{xx}/G_{xx}^0$  decrease monotonically with increasing  $Pe$  at large  $pL$  (cf. Figure 2.6 (right)). In any case, shear leads to an alignment and additional stretching even in the limit of very large activity.

The radius of gyration-tensor component along the gradient direction is displayed in Figure 2.7. Note that  $G_{yy} \equiv G_{zz}$ . Consistent with the extension in the flow direction, a polymer shrinks in the transverse direction. We find the asymptotic dependencies for  $Wi \rightarrow \infty$  and  $Pe = 0$ ,  $G_{yy}/G_{yy}^0 = \sqrt[3]{30}Wi^{-2/3}$  for  $pL \rightarrow 0$ , and  $G_{yy}/G_{yy}^0 = \sqrt[3]{540pL/\pi^4}Wi^{-2/3}$  for  $pL \gg 1$ . In the limit  $Pe \rightarrow \infty$ ,  $G_{yy}/G_{yy}^0 = \pi/(\sqrt{2}Wi)$  independent of  $pL$ . Again, the latter dependence is specific for active systems, since passive polymers typically show a weaker dependence on the Weissenberg number [142, 144].

### 2.2.3 Alignment

Anisotropic objects in shear flow are preferentially aligned along the flow direction [142, 144]. We characterize the extent of alignment by the angle  $\chi_G$  between the eigenvector of the gyration tensor with the largest eigenvalue and the flow direction. The alignment

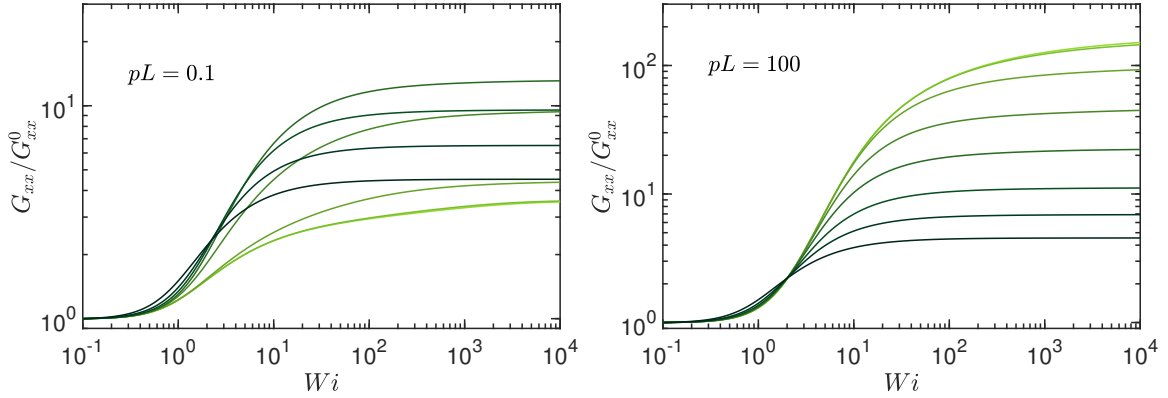


Fig. 2.6 Radius of gyration-tensor component  $G_{xx}$  along the flow direction normalized by the value  $G_{xx}^0$  at zero shear as function of the Weissenberg number  $Wi$  for the Péclet numbers  $Pe = 0, 0.6, 3, 10, 30, 10^2, 3 \times 10^2$ , and  $\infty$  (bright to dark color); **(left)**  $pL = 0.1$  and **(right)**  $pL = 10^2$ . The number of active sites is  $L/l = 10^2$  and  $\Delta = 0.3$ .

angle is conveniently obtained from the relation

$$\tan(2\chi_G) = \frac{2G_{xy}}{G_{xx} - G_{yy}} = \frac{\sum_{n=1}^{\infty} \langle \chi_{nx} \chi_{ny} \rangle}{\sum_{n=1}^{\infty} \langle \chi_{nx}^2 \rangle - \langle \chi_{ny}^2 \rangle}, \quad (2.26)$$

where

$$\langle \chi_{nx} \chi_{ny} \rangle = \frac{\dot{\gamma} k_B T}{2\gamma} \tau_n^2 + \frac{\dot{\gamma} v_0^2 l (2 + \gamma_R \tau_n)}{6(1 + \gamma_R \tau_n)^2} \tau_n^3. \quad (2.27)$$

In the asymptotic limit  $\mu \gg 1$ , i.e.,  $\tau_n \approx \tau_R/n^2\mu$ , this expression reduces to [86]

$$\tan(2\chi_G) = \frac{2\mu}{Wi\mu_0}. \quad (2.28)$$

Hence, we obtain the asymptotic dependence  $\tan(2\chi_G) \sim Wi^{-1/3}$  for  $Pe \rightarrow 0$  and  $\tan(2\chi_G) \sim Wi^{-1/2}$  for  $Pe \rightarrow \infty$ , respectively. The various regimes are displayed in Figure 2.8. For  $Wi < 1$ , the stretching coefficient is approximately unity and  $\tan(2\chi_G)$  decreases as  $Wi^{-1}$ . For large Weissenberg numbers, the shear-rate dependence of  $\mu$  becomes important and changes the  $Wi$  dependence to  $\tan(2\chi) \sim Wi^{-1/3}$  for  $Pe \ll 1$  and to  $\tan(2\chi) \sim Wi^{-1/2}$  for  $Pe \gg 1$ .

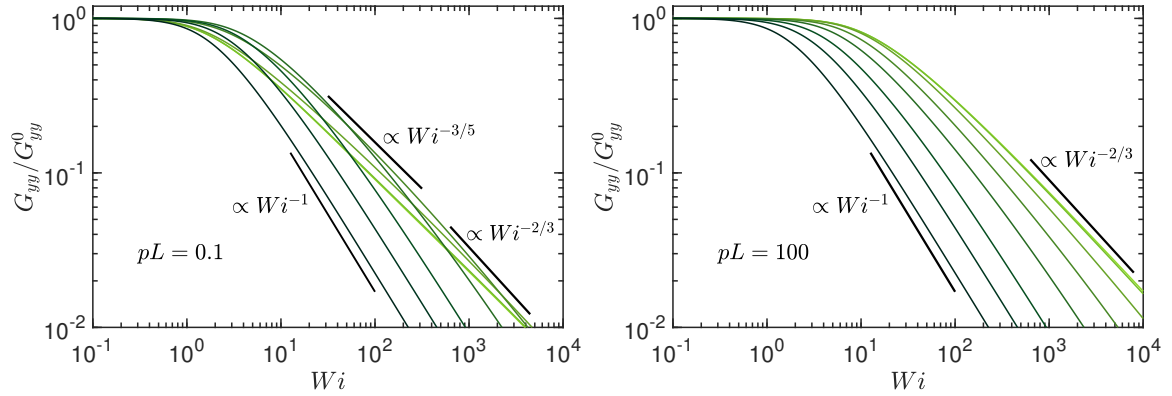


Fig. 2.7 Radius of gyration-tensor component  $G_{yy}$  along the gradient direction normalized by the value  $G_{yy}^0$  at zero shear as function of the Weissenberg number  $Wi$  for the Péclet numbers  $Pe = 0, 0.6, 3, 10, 30, 10^2, 3 \times 10^2$ , and  $\infty$  (bright to dark color); (left)  $pL = 0.1$  and (right)  $pL = 10^2$ . The number of active sites is  $L/l = 10^2$  and  $\Delta = 0.3$ .

## 2.3 Rheology: Viscosity

The polymer contribution  $\eta_p$  to the viscosity of a dilute solution follows from the virial expression of the stress tensor

$$\sigma_{xy} = -\rho \int_{-L/2}^{L/2} \langle F_x(s)r_y(s) \rangle ds \quad (2.29)$$

via  $\eta_p = \sigma_{xy}/\dot{\gamma}$ , where  $\mathbf{F}$  is the intramolecular force of Equation (2.1) and  $\rho$  the polymer concentration. The active force,  $\gamma\mathbf{v}(s, t)$ , does not contribute to the stress tensor. Evaluation of the average in Equation (2.29) yields

$$\eta_p = \frac{\rho k_B T \gamma}{\dot{\gamma}} \sum_{n=1}^{\infty} \frac{1}{\tau_n} \langle \chi_{nx} \chi_{ny} \rangle = \frac{\rho k_B T}{2} \sum_{n=1}^{\infty} \left[ \tau_n + \frac{\gamma v_0^2 l (2 + \gamma_R \tau_n)}{3 k_B T (1 + \gamma_R \tau_n)^2} \tau_n^2 \right], \quad (2.30)$$

which depends via the stretching coefficient  $\mu$  on the shear rate.

The zero-shear viscosity  $\eta_p^0$  follows from Equation (2.30) via the stretching coefficient  $\mu_0$ . Its dependence on  $Pe$  is shown in Figure 2.9. The viscosity  $\eta_p^{00}$  at zero shear and zero Péclet number is given by  $\eta_p^{00} = \rho k_B T \pi^2 \tau_R / 12$  for  $pL \gg 1$ , and by  $\eta_p^{00} = \gamma L^3 \rho / 72$  for  $Pe \rightarrow 0$ . In the latter case, the first mode,  $\tau_1 = \gamma L^3 / 36 k_B T$ , describing the rotational motion of the rodlike polymer, dominates the sum over the relaxation times [88]. For flexible polymers, where  $pL \gg 1$ , the zero-shear viscosity increases monotonically with increasing  $Pe$ , and saturates at  $\eta_p^0 / \eta_p^{00} = 4pL/5$  in the limit  $Pe \rightarrow \infty$ . Thereby, the viscosity increase, associated with the monotonic swelling of the polymer with increasing activity [74], is substantial because  $\eta_p^0 / \eta_p^{00} \sim pL$ . With

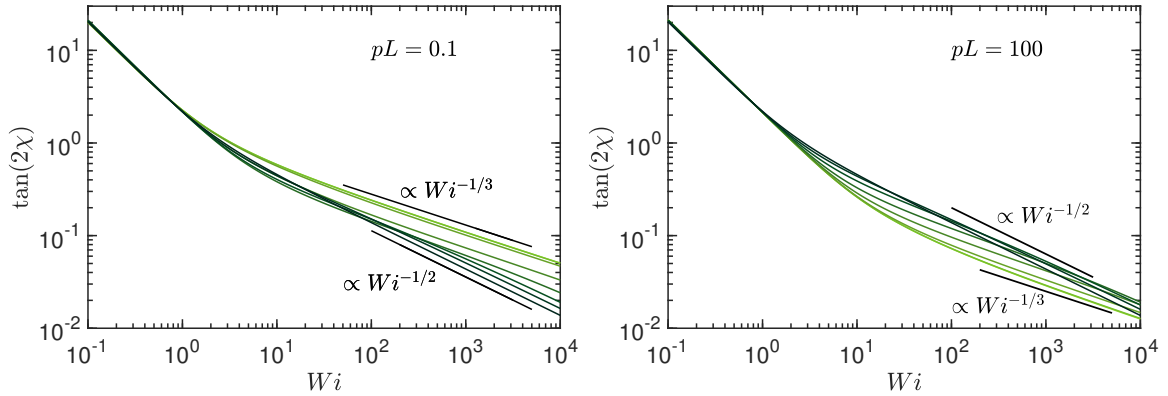


Fig. 2.8 Shear-induced polymer alignment, characterized by the angle  $\chi_G$  between the eigenvector of the gyration tensor with the largest eigenvalue and the flow direction, as function of the Weissenberg number  $Wi$ . The Péclet numbers are  $Pe = 0, 0.6, 3, 10, 30, 10^2, 3 \times 10^2$ , and  $\infty$  (bright to dark color); **(left)**  $pL = 0.1$  and **(right)**  $pL = 10^2$ . The number of active sites is  $L/l = 10^2$  and  $\Delta = 0.3$ .

increasing stiffness, the activity-induced polymer shrinkage (cf. Ref. [74]) implies a decrease in  $\eta_p^0$ , followed by an increase due to a reswelling of the polymer for  $Pe \rightarrow \infty$ , and the asymptotic value  $\eta_p^0/\eta_p^{00} = 8/5$  is assumed. Here, the activity dependence of  $\eta_p^0$  is significantly smaller than for flexible polymers, and reduces to a factor below two in the rod limit.

The shear-rate dependence of the viscosity  $\eta_p$ , normalized by  $\eta_p^0$ , is displayed in Figure 2.10 for various Péclet numbers. Independent of persistence length and activity, the polymers exhibit shear thinning. However, the dependence on the Weissenberg number is strongly affected by the activity. The behavior of passive semiflexible polymers, where  $Pe = 0$ , has been discussed theoretically in Ref. [142]. For such polymers, the viscosity exhibits the asymptotic dependencies for  $Wi \rightarrow \infty$ :  $\eta_p/\eta_p^0 = (540pL/\pi^4)^{1/3}Wi^{-2/3}$  for  $pL \gg 1$  and  $\eta_p/\eta_p^0 = (30)^{1/3}Wi^{-2/3}$  for  $pL < 1$ . In fact, for large stiffness,  $pL = L/2l_p < 1$ , there is a cross-over regime with an approximate power-law drop of  $\eta_p \sim Wi^{-3/5}$  as indicated in Figure 2.10 (left). Here, both bending and stretching modes contribute with a Weissenberg number-dependent weight. Activity substantially changes the shear-thinning behavior, and, with increasing  $Pe$ , the ratio  $\eta_p/\eta_p^0$  decreases faster with increasing shear rate. From Equation (2.30), we obtain the relation

$$\frac{\eta_p}{\eta_p^0} = \frac{\mu_0^2}{\mu^2} \underset{Wi \rightarrow \infty}{=} \frac{\pi}{\sqrt{2}Wi} \quad (2.31)$$

in the limit  $Pe \rightarrow \infty$ , which is independent of  $pL$ . Hence, activity enhances shear thinning considerably.

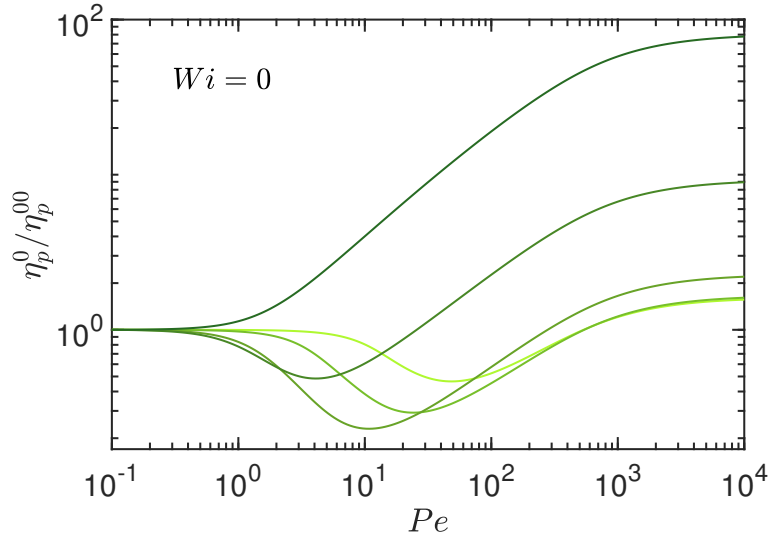


Fig. 2.9 Zero-shear viscosity  $\eta_p^0$  normalized by the zero-shear viscosity  $\eta_p^{00}$  of a passive polymer as function of the Péclet number  $Pe$  for the polymer stiffness  $pL = 100, 10, 1, 0.1,$  and  $0.01$  (top to bottom at  $Pe = 10^4$ , dark to bright color). The number of active sites is  $L/l = 10^2$  and  $\Delta = 0.3$ .

Shear thinning of passive polymers, where  $Pe = 0$ , has intensively been studied experimentally [145, 146], theoretically [142], and by simulations [144, 147–152]. Specifically, measurements on DNA molecules provided insight into the behavior of individual polymers [146]. These experiments and simulations often predicted a power-law decay of the viscosity in the shear-thinning regime, with exponents in the range  $1/2$  to  $2/3$ . The spread is partially explained by the very broad crossover regime between the zero-shear viscosity and the asymptotic dependence for  $Wi \rightarrow \infty$ . In any case, activity is predicted to lead to a significantly stronger shear-thinning effect.

## 2.4 Discussion

The coupling between shear flow and activity, as is visible in the correlation functions (2.10)–(2.12), determines the characteristics of an ABPO in shear flow. The shear-rate dependence of all properties—conformational, dynamical, and rheological—are modified by activity. Thereby, the determining factor is the polymer inextensibility, which is reflected in the activity and shear-rate dependence of the stretching coefficient  $\lambda = 3p\mu/2$  in our coarse-grained description. In particular, the asymptotic behavior for  $Pe, Wi \rightarrow \infty$  is naturally governed by inextensibility. As far as the dynamics is concerned, we find a weaker variation of the relaxation times with shear rate at large activities compared to a passive polymer, with the longest relaxation time  $\tau_1$  changing from a  $\tau_1 \sim Wi^{-2/3}$  dependence of a passive polymer to a  $\tau_1 \sim Wi^{-1/2}$  decay for

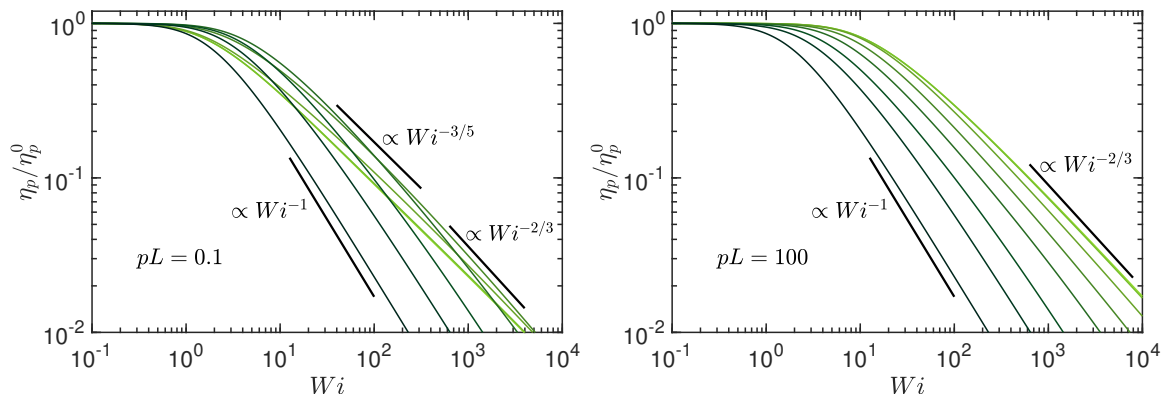


Fig. 2.10 Shear viscosity  $\eta_p$  normalized by the viscosity  $\eta_p^0$  of a non-sheared, active polymer as function of the Weissenberg number  $Wi$  for the Péclet numbers  $Pe = 0, 0.6, 3, 10, 30, 10^2, 3 \times 10^2$ , and  $\infty$  (bright to dark color); **(left)**  $pL = 0.1$  and **(right)**  $pL = 10^2$ . The number of active sites is  $L/l = 10^2$  and  $\Delta = 0.3$ .

$Pe \gg 1$ . In turn, this results in a change of the shrinkage of the radius of gyration components  $G_{yy} = G_{zz}$  from a  $Wi^{-2/3}$  to a  $Wi^{-1}$  dependence, a similar change for the viscosity  $\eta_p$ , and a change of the alignment from a  $Wi^{-1/3}$  to a  $Wi^{-1/2}$  dependence with increasing  $Wi$  at  $Pe \gg 1$ . As has already been discussed in Ref. [74], flexible and semiflexible ABPO show the same activity-induced swelling behavior for  $Pe \gg 1$ , independent of  $pL$ . Consequently, a universal shear-flow behavior is obtained in that limit. For all conformational ( $G_{xx}$ ,  $G_{yy}$ ,  $\tan(2\chi_G)$ ), dynamical ( $\tau_1$ ), and rheological ( $\eta_p$ ) properties, universal curves are obtained, with shear-rate dependencies differing from those of a passive system. The behavior originates from the dominance of the flexible modes ( $n^2$ ) in the relaxation behavior for all stiffness caused by activity.

Active dumbbells already exhibit various of the discussed shear-induced characteristics [86]. However, the polymer nature, with the many more internal degrees of freedom, provides additional features and means of controlling active properties. Specifically, the number of active sites,  $L/l$ , is important. As our study shows, the crossover from the power laws valid for passive polymers to those of an ABPO at  $P \gg 1$  depends crucially on  $L/l$ . With increasing  $L/l$ , the power laws for  $Pe \gg 1$  appear at much larger Weissenberg numbers only. Depending on the size of the polymer, the Weissenberg numbers of the crossover could exceed experimentally accessible values. For computer simulations of an ABPO described as bead-spring polymer [72, 117], this aspect is of minor concern because typically every monomer is considered as an ABP and not too long polymers are studied.

## Chapter 3

# Active Brownian polymer with hydrodynamic interactions

In this chapter, we analyze the influence of hydrodynamic interactions on the conformational and dynamical properties of ABPOs, denoted as ABPOs+HI in the following, by computer simulations and an analytical approach. In simulations, we employ a bead-spring linear phantom or self-avoiding polymer with ABP monomers (cf. Fig. 3.1), where the ABP propulsion direction changes diffusively, [117] and hydrodynamic interactions are taken into account Rotne-Prager-Yamakawa hydrodynamic tensor. [153, 154] For the analytical calculations, we consider a Gaussian semiflexible polymer, [74, 89, 120] with active sites modeled by an Ornstein-Uhlenbeck process (active Ornstein-Uhlenbeck particle, AOUP), [74, 123, 125] where the active velocity vector changes in a diffusive manner; here, HI is included via the preaveraged Oseen tensor. [132, 155] The main purpose of our study is to resolve the influence of hydrodynamics on the properties of self-propelled polymers, respecting the force-free nature of an individual active agent. Hence, no Stokeslet due to self-propulsion is present. Only Stokeslets arising from bond, bending, and excluded-volume interactions between monomers, as well as thermal forces are considered. Moreover, we neglect higher order multipole contributions of the active monomers, especially the force dipole. Since we consider point particles, source multipoles are also absent. All these multipoles decay faster than a Stokeslet. Hence, we capture the long-range character of HI in polymers of a broad class of active monomers. As far as near-field hydrodynamic effects are concerned, our model closest resembles a polymer composed of neutral squirmers, [24, 82, 83, 85] where particular effects by higher multipole interactions between monomers are not resolved.[78, 79]

## 3.1 Computer simulations

### 3.1.1 Model: Equation of motion

A semiflexible active polymer is composed of  $N_m$  active Brownian particles (ABPs) ( $i = 1, \dots, N_m$ , cf. Fig. 3.1), [67, 117] which obey the equations of motion

$$\dot{\mathbf{r}}_i(t) = v_0 \mathbf{e}_i(t) + \sum_{j=1}^{N_m} \mathbf{H}_{ij} [\mathbf{F}_i(t) + \mathbf{F}_j(t)], \quad (3.1)$$

$$\dot{\mathbf{e}}_i(t) = \hat{\boldsymbol{\eta}}_i(t) \times \mathbf{e}_i(t). \quad (3.2)$$

Here,  $\mathbf{r}_i(t)$  and  $\dot{\mathbf{r}}_i(t)$  denote the position and velocity of particle  $i$ , respectively, and  $\mathbf{c}$ . The forces  $\mathbf{F}_i(t) = -\nabla_{\mathbf{r}_i}(U_l + U_b + U_{LJ})$  following from the bond ( $U_l$ ), bending ( $U_b$ ), and volume exclusion ( $U_{LJ}$ ) potentials, [117] given by Eqs. (1.87), (1.86) and (1.88), respectively.  $\mathbf{F}_i$  and  $\hat{\boldsymbol{\eta}}_i$  are Gaussian and Markovian stochastic processes with zero mean and the second moments

$$\langle \mathbf{F}_i(t) \mathbf{F}_j^T(t') \rangle = 2k_B T \mathbf{H}_{ij}^{-1} \delta(t - t'), \quad (3.3)$$

$$\langle \hat{\eta}_{i\alpha}(t) \hat{\eta}_{j\beta}(t') \rangle = 2D_R \delta_{\alpha\beta} \delta_{ij} \delta(t - t'), \quad (3.4)$$

where  $\mathbf{F}_i^T$  denotes the transpose of  $\mathbf{F}_i$ , and  $\mathbf{H}_{ij}^{-1}$  the inverse of  $\mathbf{H}_{ij}$ ;  $T$  is the temperature,  $k_B$  the Boltzmann constant, and  $D_R$  the rotational diffusion coefficient of a spherical colloid. The tensor  $\mathbf{H}_{ij}(\mathbf{r}_{ij}) = \delta_{ij} \mathbf{I} / 3\pi\eta l + (1 - \delta_{ij}) \boldsymbol{\Omega}(\mathbf{r}_{ij})$  accounts for hydrodynamic interactions, with the first term including local friction, and the Rotne-Prager-Yamakawa tensor [124, 153, 154]

$$\boldsymbol{\Omega}(\mathbf{r}_{ij}) = \begin{cases} \frac{1}{8\pi\eta r_{ij}} \left[ \mathbf{I} + \frac{\mathbf{r}_{ij} \mathbf{r}_{ij}^T}{r_{ij}^2} + \frac{l^2}{2r_{ij}^2} \left( \frac{1}{3} \mathbf{I} - \frac{\mathbf{r}_{ij} \mathbf{r}_{ij}^T}{r_{ij}^2} \right) \right], & r_{ij} > l \\ \frac{1}{3\pi\eta l} \left[ \left( 1 - \frac{9}{16} \frac{r_{ij}}{l} \right) \mathbf{I} + \frac{3}{16} \frac{r_{ij}}{l} \frac{\mathbf{r}_{ij} \mathbf{r}_{ij}^T}{r_{ij}^2} \right], & r_{ij} < l \end{cases}, \quad (3.5)$$

with the solvent viscosity  $\eta$  and the unit matrix  $\mathbf{I}$ . We assume a touching bead model of spherical colloids, hence, the monomer hydrodynamic radius is half of the bond length  $l$ . The Rotne-Prager-Yamakawa tensor insures the positive definiteness of the hydrodynamic tensor even at small distances. The translational equations of motion (3.1) are solved via the Ermak-McCammon algorithm. [101, 102] The procedure to solve the equations of motion (3.2) for the orientation vectors is described in Subsec.1.4.1. [122]

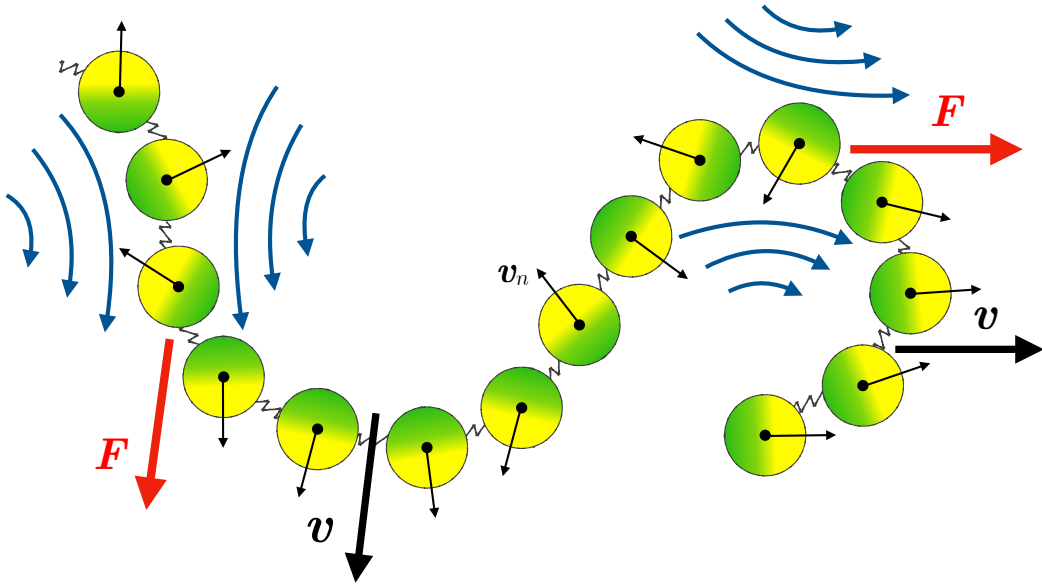


Fig. 3.1 Illustration of the activity-induced flow by the motion of an ABPO+HI. Several ABPs moving by chance together in a certain direction, indicated by the velocity arrow  $\mathbf{v}$ , drag other connected ABPs, which in turn exert a force,  $\mathbf{F}$ , indicated by the red arrow, on the fluid inducing Stokes flow. The small arrows  $\mathbf{v}_n$  display the direction of the active velocity. No flow field is generated by the active motion of an individual ABP.

The Péclet number  $Pe$  and the ratio  $\Delta$  between translational,  $D_T = k_B T / 3\pi\eta l$ , and rotational,  $D_R$ , diffusion coefficient are given by Eq. (1.89). The coefficient  $\kappa_l$  (Eq. (1.86)) for the bond strength is adjusted according to the applied Péclet number, in order to avoid bond stretching with increasing activity. By choosing  $\kappa_l l^2 / k_B T = (10 + 2Pe)10^3$ , bond-length variations are smaller than 3% of the equilibrium value  $l$ . Here, the scaled bending force coefficient  $\tilde{\kappa}_b = \kappa_b l^2 / k_B T$  (Eq. (1.87)) is related to the polymer persistence length,  $l_p = 1/(2p)$ , by Eq. (1.90). We set  $\sigma = 0.8l$  and  $\epsilon = k_B T$  as the parameters of the truncated and shifted Lennard-Jones potential.

### 3.1.2 Conformations

We characterize the polymer conformations by the mean square end-to-end distance. Results for phantom polymers of length  $L = (N_m - 1)l = 49l$  and  $L = 199l$  are presented in Fig. 3.2. Evidently, ABPOs in the presence of hydrodynamic interactions exhibit a pronounced shrinkage for  $1 \lesssim Pe \lesssim 10$ , where shrinkage depends on polymer length and is substantially stronger for longer polymers. Semiflexible ABPOs+HI shrink stronger than ABPOs-HI, but the effect vanishes gradually as  $pL \rightarrow 0$ . This is a consequence of the reduced influence of hydrodynamic interactions for rather stiff polymers. [91] Yet, the asymptotic swollen value for  $Pe \rightarrow \infty$  of ABPOs+HI is

smaller than the value for ABPOs-HI, for which theory predicts  $L^2/2$  and simulations yield approximately  $2L^2/5$ . [74] Hence, hydrodynamic interactions affect the swelling behavior of flexible and semiflexible polymers for all  $Pe > 0$ . In particular, the asymptotic size  $\langle r_e^2 \rangle \approx L^2/10$  for  $Pe \rightarrow \infty$ , which is independent of stiffness, is smaller than the value for an ABPO-HI.

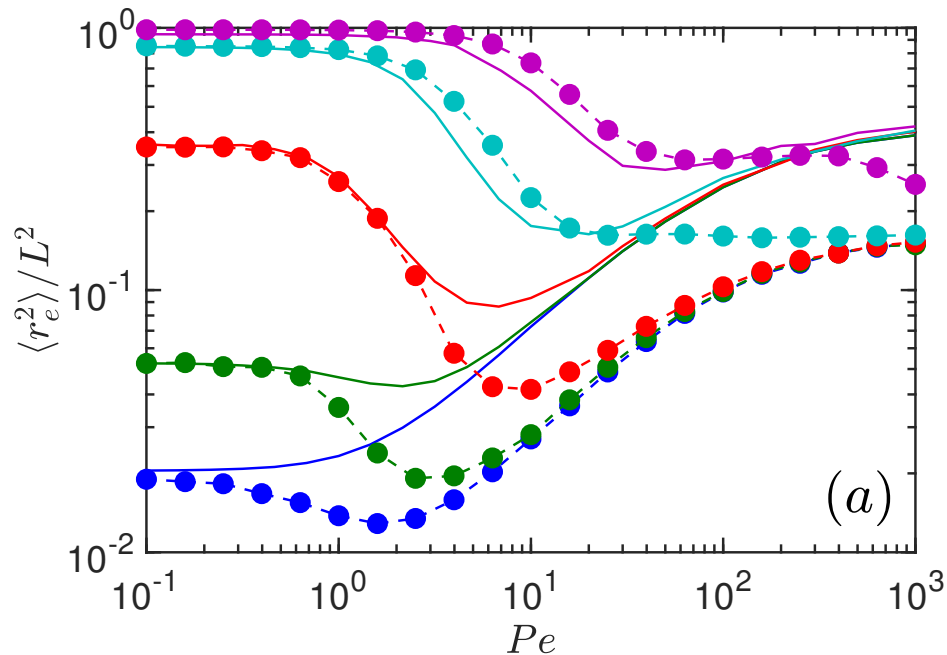


Fig. 3.2 Mean square end-to-end distance (simulations) as a function of the Péclet number for semiflexible polymers with  $N_m = 50$  ( $L = 49l$ ) monomers (bullets) and  $pL = 5 \times 10^1$  (blue),  $1.5 \times 10^1$  (green),  $2.6$  (red),  $2.5 \times 10^{-1}$  (cyan), and  $2.5 \times 10^{-2}$  (purple). In the solid lines are theoretical results for ABPOs-HI, and bullets are for phantom polymers. The dashed lines are guides for the eye. See Fig. 3.4 for snapshots.

Self-avoidance reduces the extent of shrinkage, specifically of flexible polymers. This is illustrated in Fig. 3.3. For  $pL \gtrsim 10$ , the equilibrium value  $\langle r_e^2 \rangle$  of a self-avoiding polymer is swollen compared to a phantom polymer. Such an ABPO+HI exhibits a less pronounced shrinkage for all polymer lengths. Naturally, excluded-volume effects vanish with decreasing  $pL$ , and for  $pL < 1$  there is hardly any difference between a phantom and a self-avoiding polymer. Moreover, the swelling behavior with and without excluded-volume interactions is rather similar in the limit  $Pe \gg 1$ . Interestingly, phantom and self-avoiding polymers show a universal dependence on  $Pe$  as they start to swell. Here, active forces exceed both, excluded-volume interactions and bending forces. As predicted by theory (cf. Sec. 3.2.3), the internal dynamics is determined by the modes of a flexible polymer, i.e., intermolecular tension, in this regime. Snapshots of conformations with and without HI are presented in Fig. 3.4.

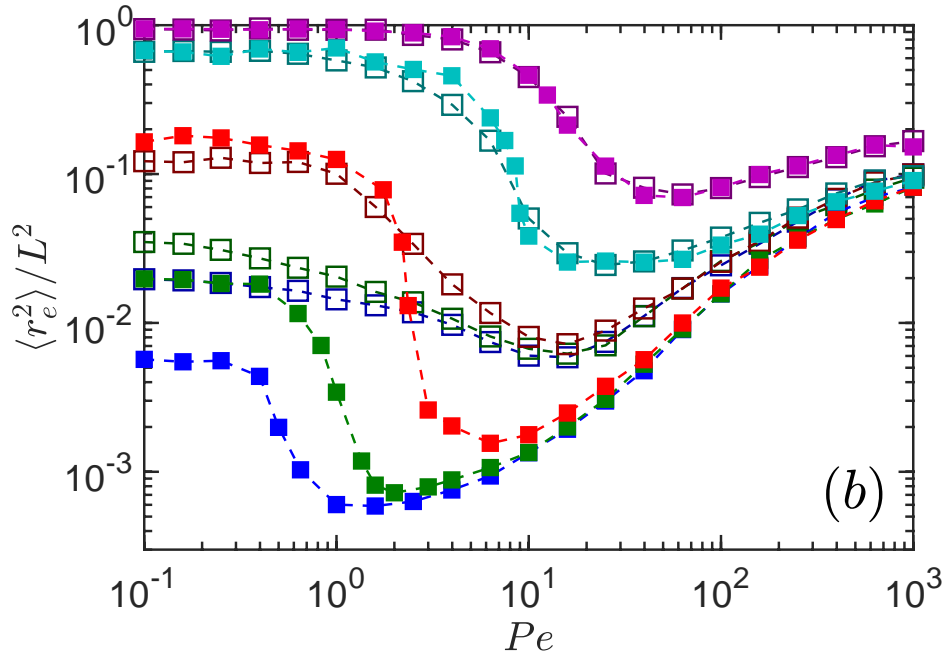


Fig. 3.3 Mean square end-to-end distance (simulations) as a function of the Péclet number for semiflexible polymers with  $N_m = 200$  ( $L = 199l$ ) monomers (squares) for  $pL = 2 \times 10^2$  (blue),  $6 \times 10^1$  (green),  $10^1$  (red), 1 (cyan), and  $10^{-1}$  (purple). In filled squares correspond to phantom and open squares to self-avoiding polymers. The dashed lines are guides for the eye. See Fig. 3.4 for snapshots.

### 3.1.3 Dynamical properties

The dynamics of ABPO+HI is characterized by the monomer mean square displacement (MSD) averaged over all monomers  $\langle \overline{\Delta \mathbf{r}^2}(t) \rangle = \sum_i \langle (\mathbf{r}_i(t) - \mathbf{r}_i(0))^2 \rangle / N_m$ . Figure 3.5 shows MSDs of a polymer with  $N_m = 200$  monomers for various Péclet numbers. A passive polymer exhibits the well-known Zimm behavior, with the time dependence  $t^{2/3}$  of the MSD in the center-of-mass reference frame for  $t/\tau_Z \ll 1$ . At long times  $t/\tilde{\tau}_1 \gg 1$ , the center-of-mass displacement dominates the monomer MSD for all Péclet numbers. Here, we find the HI-independent MSD  $\langle \mathbf{r}_{cm}^2 \rangle = 2v_0^2 lt / \gamma_R L$  following from Eq. (3.1) for  $Pe \gg 1$  (see also Eq. (3.41)). For Péclet numbers  $Pe > 1$ , the active ballistic regime,  $\langle \overline{\Delta \mathbf{r}^2} \rangle \sim t^2$ , is present at short times ( $\gamma_R t, t/\tilde{\tau}_1 < 1$ ). Moreover, for  $t/\tilde{\tau}_1 \gtrsim 1$  and moderate Péclet numbers,  $Pe \approx 10$ , activity implies a polymer-specific regime, where the monomer MSD exhibits a power-law dependence  $\langle \overline{\Delta \mathbf{r}^2}(t) \rangle \sim t^{\alpha'}$ , with an exponent of  $\alpha' \approx 2/5$ , a value smaller than the exponent  $\alpha' = 2/3$  of the Zimm dynamics. The reduction of the exponent is a clear consequence of the coupling between hydrodynamics and activity, since ABPOs-HI always display slopes  $\alpha' \gtrsim 1/2$ , where  $\alpha' = 1/2$  is the value of a passive flexible polymer (Rouse model). [76] However, this regime appears as a crossover from the ballistic to the diffusive regime. Neverthe-

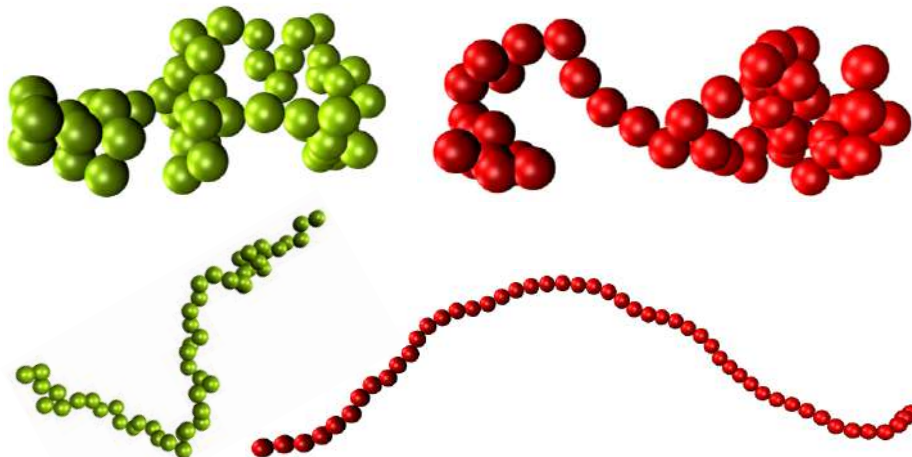


Fig. 3.4 Configurations of flexible phantom ABPOs of length  $N_m = 50$  for the Péclet numbers  $Pe = 1$  (top) and  $10^3$  (bottom) in the presence (green) and absence (red) of hydrodynamic interactions.

less, it is a consequence of hydrodynamics with a sub-diffusive motion. The polymer-specific regime vanishes gradually with increasing  $Pe$ . As discussed in Sec. 3.2.3, this is a consequence of the decreasing polymer relaxation times with increasing activity.

## 3.2 Analytical model of active Brownian polymer in solution

The simulations of the previous section yield a surprising shrinkage of even flexible polymers by hydrodynamic interactions. In order to shed light on the underlying mechanisms, we study an mean-field analytical model, where an active polymer is described by a continuous Gaussian semiflexible polymer model. [89, 120] This approach has been applied successfully in the analysis the properties of ABPO-HI [74, 76] in close quantitative agreement with simulations.[117]

### 3.2.1 Equations of motion

The polymer is considered as a differentiable space curve  $\mathbf{r}(s, t)$  of length  $L$ , with contour coordinate  $s$  ( $-L/2 \leq s \leq L/2$ ) and time  $t$ . Activity is introduced in analogy to an active Ornstein-Uhlenbeck particle (AOUP)[125] by assigning a propulsion velocity  $\mathbf{v}(s, t)$  to every point  $\mathbf{r}(s, t)$  (cf. Fig. 3.1) [2, 74, 76], which changes in an independent

### 3.2 Analytical model of active Brownian polymer in solution

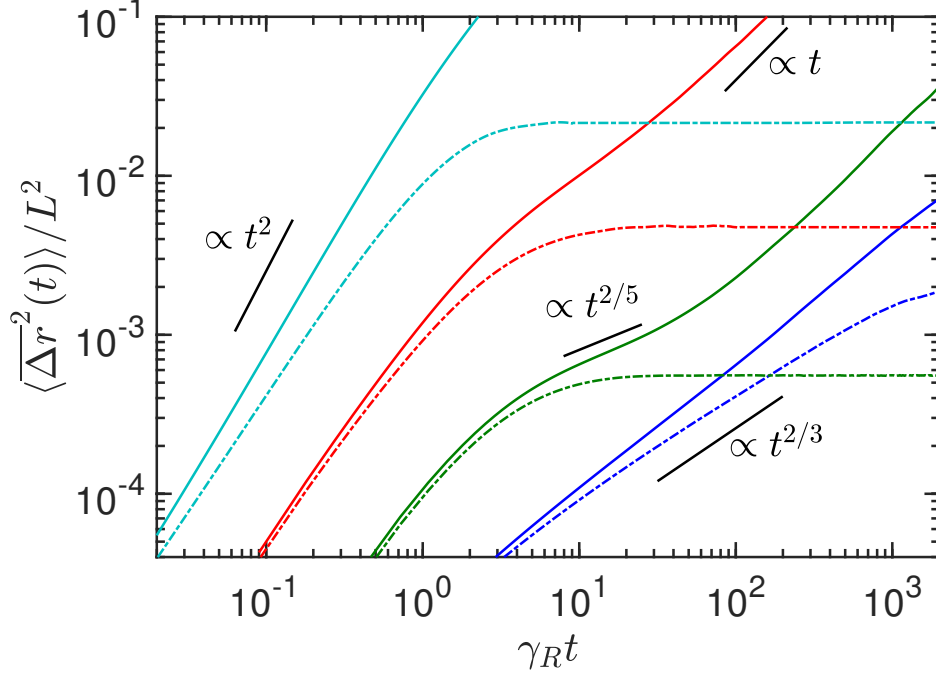


Fig. 3.5 Mean square displacement of a flexible phantom polymer with  $N_m = 200$  ( $pL = 200$ ) monomers for the Péclet numbers  $Pe = 0$  (blue),  $10^1$  (green),  $10^2$  (red), and  $10^3$  (cyan). The time is scaled by the factor  $\gamma_R = 2D_R$ . The solid lines indicate the monomer MSD and the dashed lines the MSD in the polymer center-of-mass reference frame. The black lines are guides for the eye correspond to a power-law fit of the data in the respective regime.

manner. The equation of motion is then given by the Langevin equation [120, 131]

$$\begin{aligned} \frac{\partial \mathbf{r}(s, t)}{\partial t} = & \mathbf{v}(s, t) + \int_{-L/2}^{L/2} ds' \mathbf{H}(\mathbf{r}(s), \mathbf{r}(s')) \\ & \times \left[ 2\nu k_B T \frac{\partial^2 \mathbf{r}(s', t)}{\partial s'^2} - \epsilon k_B T \frac{\partial^4 \mathbf{r}(s', t)}{\partial s'^4} + \mathbf{\Gamma}(s', t) \right], \end{aligned} \quad (3.6)$$

with boundary conditions for free ends as specified in Refs. 74, 76, 88. The tensor  $\mathbf{H}(\mathbf{r}(s), \mathbf{r}(s'))$  accounts for hydrodynamic interactions; it is defined as  $\mathbf{H}(\mathbf{r}(s), \mathbf{r}(s')) = \mathbf{\Omega}(\mathbf{r}(s) - \mathbf{r}(s')) + \mathbf{I}\delta(s - s')/3\pi\eta$ , where the second term on the right hand side describes the local friction, and

$$\mathbf{\Omega}(\Delta \mathbf{r}) = \frac{1}{8\pi\eta|\Delta \mathbf{r}|} \left( \mathbf{I} + \frac{\Delta \mathbf{r} \otimes \Delta \mathbf{r}}{|\Delta \mathbf{r}|^2} \right) \quad (3.7)$$

is the Oseen tensor [132, 155]. The terms in Eq. (3.6) with the second and fourth derivative capture chain flexibility, i.e., chain entropy, and bending forces, respectively.

The Lagrangian multipliers  $\nu(s)$  and  $\nu_0 = \nu(\pm L/2)$  account for the inextensibility of the polymer (we will denote  $\nu$  as stretching coefficient in the following), and  $\epsilon$  characterizes the bending stiffness [87, 90]. For a polymer in three dimensions, previous studies yield  $\epsilon = 3/4p$  and  $\nu_0 = 3/4$ , where  $p = 1/2l_p$  and  $l_p$  is the persistence length [87, 90]. Adopting a mean-field approach, the stretching coefficient  $\nu$  is independent of  $s$  and is determined by the global constraint

$$\int_{-L/2}^{L/2} \left\langle \left( \frac{\partial \mathbf{r}(s)}{\partial s} \right)^2 \right\rangle ds = L. \quad (3.8)$$

The stochastic force  $\mathbf{F}(s, t)$  is assumed to be stationary, Markovian, and Gaussian. [95, 132]

Within the AOUP description of the analytical calculations, the active velocity  $\mathbf{v}(s, t)$  is a non-Markovian but Gaussian stochastic process with zero mean and the correlation function [1, 73, 74, 86]

$$\langle \mathbf{v}(s, t) \cdot \mathbf{v}(s', t') \rangle = v_0^2 l e^{-\gamma_R |t-t'|} \delta(s - s'). \quad (3.9)$$

Here,  $v_0$  is the constant propulsion velocity and  $\gamma_R$  characterizes the decay of the velocity correlation function. For a spherical colloid in solution, the relation  $\gamma_R = 2D_R$  applies, where  $D_R$  is the rotational diffusion coefficient. The correlation function (3.9) emerges due to a diffusive motion of either the Ornstein-Uhlenbeck process for the active velocity, or by the change of the propulsion direction (unit vector) of an ABP. [74, 125]. Since only first and second moments of the active velocity are required for the current analytical studies, the results are independent of the underlying active velocity dynamics of an active site—either AOUP or ABP. Further details on the derivation of the equations of motion are presented in Ref. 74, including a discussion of the factor  $l$  in Eq. (3.9).

Self-propelled systems are force and torque free [1, 2]. Hence, only conservative and random forces give rise to Stokeslet-type hydrodynamic interactions in Eq. (3.6). However, we neglect force-dipole, source-dipole, and higher multipole flow field contributions, as they decay as  $\mathcal{O}(r^{-2})$  with distance compared to a  $1/r$  decay of the Stokeslet flow field [79].

### 3.2.2 Solution of the equations of motion

#### Hydrodynamic tensor: Preaveraging approximation

The hydrodynamic tensor renders Eq. (3.6) a nonlinear and nonlocal equation of motion. In order to obtain an (approximate) analytical solution, we apply the preaveraging approximation originally proposed by Zimm [132, 156], where the hydrodynamic

### 3.2 Analytical model of active Brownian polymer in solution

---

tensor is replaced by its average over the stationary state distribution function, i.e.,  $\mathbf{H}(\mathbf{r}(s) - \mathbf{r}(s')) \rightarrow \langle \mathbf{H}(\mathbf{r}(s) - \mathbf{r}(s')) \rangle = \mathbf{H}(s, s')$ . Hence, Eq. (3.6) turns into a linear equation—an Ornstein-Uhlenbeck process—with a Gaussian stationary-state distribution function for the distance  $\Delta \mathbf{r}(s, s') = \mathbf{r}(s) - \mathbf{r}(s')$  of the form [95, 120, 125, 132]

$$\Psi(\Delta \mathbf{r}) = \left( \frac{3}{2\pi a^2(s, s')} \right)^{3/2} \exp \left( -\frac{3\Delta \mathbf{r}^2}{2a^2(s, s')} \right), \quad (3.10)$$

with  $a^2(s, s') = \langle (\mathbf{r}(s) - \mathbf{r}(s'))^2 \rangle$ . Note that  $a(s, s')$  is not necessarily a function of  $s - s'$  only. The explicit form of  $a(s, s')$  will be discussed later. Preaveraging yields [120]

$$\mathbf{\Omega}(s, s') = \frac{\Theta(|s - s'| - l)}{3\pi\eta} \sqrt{\frac{3}{2\pi a^2(s, s')}} \mathbf{I} = \Omega(s, s') \mathbf{I}, \quad (3.11)$$

and the hydrodynamic tensor becomes

$$\mathbf{H}(s, s') = \left[ \frac{\delta(s - s')}{3\pi\eta} + \Omega(s, s') \right] \mathbf{I} = H(s, s') \mathbf{I}. \quad (3.12)$$

The Heaviside step function,  $\Theta(x)$ , in Eq. (3.11) introduces a lower cut-off, which we choose as  $l$ . [120] In a touching bead model of a polymer,  $l$  is the bead diameter and, hence, the polymer thickness.

The preaveraging approximation has very successfully been applied to describe the dynamics of DNA [131] and semiflexible polymers. [120] Even quantitative agreement between analytical theory and simulations of the full hydrodynamic contribution of rather stiff polymers is achieved, [157] as well as with measurements on DNA. [131, 158] This demonstrates that preaveraging is also suitable for rather stretched polymers, it, however, fails for rodlike objects.[91]

#### Eigenfunction expansion

The final linear equation is solved by the eigenfunction expansion

$$\mathbf{r}(s, t) = \sum_{n=0}^{\infty} \chi_n(t) \varphi_n(s) \quad (3.13)$$

in terms of the eigenfunctions  $\varphi_n$  of the equation

$$\epsilon k_B T \frac{d^4}{ds^4} \varphi_n(s) - 2\nu k_B T \frac{d^2}{ds^2} \varphi_n(s) = \xi_n \varphi_n(s), \quad (3.14)$$

with the eigenvalues ( $n \in \mathbb{N}_0$ )

$$\xi_n = k_B T (\epsilon \zeta_n^4 + 2\nu \zeta_n^2). \quad (3.15)$$

The mode numbers  $\zeta_n$  follow from the boundary conditions. The respective eigenfunctions and eigenvalues are explicitly presented in Refs. [74, 76, 88]. Specifically, in the limit of a flexible polymer,  $pL \gg 1$ , the eigenfunctions are

$$\varphi_0 = \sqrt{\frac{1}{L}}, \quad (3.16)$$

$$\varphi_n(s) = \sqrt{\frac{2}{L}} \sin\left(\frac{n\pi s}{L}\right), \quad \forall n \text{ odd} \quad (3.17)$$

$$\varphi_n(s) = \sqrt{\frac{2}{L}} \cos\left(\frac{n\pi s}{L}\right), \quad \forall n \text{ even}, \quad (3.18)$$

with the wave numbers  $\zeta_n = n\pi/L$  and the eigenvalues  $\xi_n = 2\nu k_B T \pi^2 n^2 / L^2$ .

The equation of motion (3.6) yields the Langevin equation for the mode amplitudes,  $\chi_n(t)$ ,

$$\frac{d\chi_m(t)}{dt} = \sum_{n=0}^{\infty} H_{mn} [\Gamma_n(t) - \xi_n \chi_n(t)] + \mathbf{v}_m(t). \quad (3.19)$$

The mode representation of the hydrodynamic tensor is  $H_{nm} = (\delta_{nm} + 3\pi\eta\Omega_{nm})/3\pi\eta$ , with the preaveraged Oseen tensor  $\Omega_{nm}$ . [120] The second moments of the stochastic force amplitudes  $\Gamma_n$  are given by

$$\langle \Gamma_{n\alpha}(t) \Gamma_{m\beta}(t') \rangle = 2k_B T \delta_{\alpha\beta} \delta(t-t') H_{nm}^{-1}, \quad (3.20)$$

with  $\alpha, \beta \in \{x, y, z\}$ . The mode representation of the correlation function (3.9) of the active velocity is [74]

$$\langle \mathbf{v}_n(t) \cdot \mathbf{v}_m(t') \rangle = v_0^2 l e^{-\gamma_R |t-t'|} \delta_{nm}. \quad (3.21)$$

In Eq. (3.19), all modes are coupled in general and the set of equations can only be solved numerically. To arrive at an analytical solution, we neglect the off-diagonal terms of the hydrodynamic mode tensor  $H_{nm}$ , which leads to the decoupled equations [120, 131, 132]

$$\frac{d\chi_n(t)}{dt} = -\frac{1}{\tilde{\tau}_n} \chi_n + H_{nn} \Gamma_n(t) + \mathbf{v}_n(t), \quad (3.22)$$

## 3.2 Analytical model of active Brownian polymer in solution

---

with the relaxation times

$$\tilde{\tau}_n = \frac{1}{H_{nn}\xi_n} = \frac{\tau_n}{1 + 3\pi\eta\Omega_{nn}}, \quad (3.23)$$

and  $\tau_n = 3\pi\eta/\xi_n$ , the relaxation times in absence of hydrodynamic interactions; for flexible polymers  $\tau_n = 3\eta L^2/(2\nu k_B T \pi n^2)$ . [76, 88]

The stationary-state solution of Eq. (3.19) is

$$\boldsymbol{\chi}_n(t) = \int_{-\infty}^t dt' e^{-(t-t')/\tilde{\tau}_n} [\mathbf{v}_n(t') + H_{nn}\boldsymbol{\Gamma}_n(t')] \quad (3.24)$$

for  $n > 0$ , and for  $n = 0$  the solution is

$$\boldsymbol{\chi}_0(t) = \boldsymbol{\chi}_0(0) + \int_0^t dt' [\mathbf{v}_{(0)}(t') + H_{00}\boldsymbol{\Gamma}_0(t')]. \quad (3.25)$$

### Averages and correlation functions

With the correlation functions of the stochastic forces (3.20) and velocities (3.21), the correlation functions of the mode amplitudes become ( $t \geq t'$ )

$$\begin{aligned} \langle \boldsymbol{\chi}_n(t) \cdot \boldsymbol{\chi}_m(t') \rangle &= \delta_{nm} \left( \frac{k_B T \tau_n}{\pi \eta} e^{-|t-t'|/\tilde{\tau}_n} \right. \\ &\quad \left. + \frac{v_0^2 l \tilde{\tau}_n^2}{1 - (\gamma_R \tilde{\tau}_n)^2} \left[ e^{-\gamma_R |t-t'|} - \gamma_R \tilde{\tau}_n e^{-|t-t'|/\tilde{\tau}_n} \right] \right), \end{aligned} \quad (3.26)$$

$$\begin{aligned} \langle \boldsymbol{\chi}_0(t) \cdot \boldsymbol{\chi}_0(t') \rangle &= \langle \boldsymbol{\chi}_0^2(0) \rangle + 6k_B T H_{00} t' \\ &\quad + \frac{v_0^2 l}{\gamma_R^2} \left[ 2\gamma_R t' - 1 - e^{\gamma_R(t'-t)} + e^{-\gamma_R t} + e^{-\gamma_R t'} \right]. \end{aligned} \quad (3.27)$$

The eigenfunction expansion (3.13) and the correlation functions (3.26) permit us to calculate the mean square distance  $a^2(s, s')$ . Explicitly, we find

$$a^2(s, s') = \sum_{n=1}^{\infty} \langle \boldsymbol{\chi}_n^2 \rangle (\varphi_n(s) - \varphi_n(s'))^2, \quad (3.28)$$

with the stationary-state average

$$\langle \boldsymbol{\chi}_n^2 \rangle = \frac{k_B T \tau_n}{\pi \eta} + \frac{v_0^2 l \tilde{\tau}_n^2}{1 + \gamma_R \tilde{\tau}_n}. \quad (3.29)$$

As for passive polymers, the relaxation behavior (3.26) is determined by hydrodynamics. Remarkably, however, the mode-amplitude correlation functions (3.29) depend on the hydrodynamic interactions via the relaxation times (3.23). In Eq. (3.29),

the active term with  $v_0^2$  leads to enhanced fluctuations, specifically at small mode numbers,[121] and reflects the violation of the fluctuation-dissipation relation. [159] Thus, HI changes, additionally to the dynamics, also the stationary-state conformational properties of an active polymer.

### Hydrodynamic tensor: Mode representation

In order to determine the relaxation times  $\tilde{\tau}_n$ , the double integral

$$\Omega_{nn} = \sqrt{\frac{1}{6\pi^3\eta^2}} \int_{-L/2}^{L/2} \int_{-L/2}^{L/2} \Theta(|s-s'| - l_c) \frac{\varphi_n(s)\varphi_n(s')}{\sqrt{a^2(s,s')}} ds' ds \quad (3.30)$$

needs to be evaluated, which itself depends via  $a^2(s,s')$  on the Oseen tensor  $\Omega_{nn}$ . Hence, the equation has to be solved in an iterative and self-consistent manner, where the double integration, combined with the summation of Eq. (3.28), constitutes a major computational challenge. To arrive at a more easily tractable expression with a single integral, we apply standard approximations for the integrals over the functions  $\varphi_n$  in Eq. (3.30) as, e.g., described in Ref. 132 for a flexible polymer. For a passive semiflexible polymer,  $a^2(s,s')$  is only a function of the difference  $|s-s'|$  [89, 120]. This is no longer the case in the presence of activity, where  $a^2(s,s')$  depends on  $s-s'$  and  $s+s'$  in general. In fact, an analytical expression of  $a^2$  for a flexible ABPO-HI can be calculated by performing the sum in Eq. (3.28). To obtain an approximate expression, which depends on the difference  $|s-s'|$  only, we replace the difference of the eigenfunctions in Eq. (3.28) by the expression approximately valid for a passive polymer, namely  $\varphi_n(s) - \varphi_n(s') = 2 \sin(n\pi(s-s')/2L)$  for  $n$  odd, and  $\varphi_n(s) - \varphi_n(s') = 0$  for  $n$  even. As a result, we obtain

$$a^2(s) = \frac{8}{L} \sum_{n,\text{odd}} \left( \frac{k_B T \tilde{\tau}_n}{\pi \eta} + \frac{v_0^2 l \tilde{\tau}_n^2}{1 + \gamma_R \tilde{\tau}_n} \right) \sin^2 \left( \frac{n\pi}{2L} s \right), \quad (3.31)$$

and, hence,  $\Omega_{nn}$  is given by

$$\Omega_{nn} = \sqrt{\frac{2}{3\pi^3} \frac{1}{\eta L}} \int_{l_c}^L \frac{L-s}{\sqrt{a^2(s)}} \cos \left( \frac{n\pi}{L} s \right) ds. \quad (3.32)$$

Aside from the distance  $a^2(s-s')$ , which depends on activity via the relaxation times, this expression is identical with that of a passive polymer. [120] As shown in Appendix A, the approximations of Eqs. (3.31) capture the dependence of  $a^2$  on the contour coordinate well, the better the larger the Péclet number.

## 3.2 Analytical model of active Brownian polymer in solution

---

Assuming a linear dependence of  $a^2(s - s')$  on  $|s - s'|$ , i.e.,  $a^2(s) = a_0^2|s|L$ , as for a passive flexible polymer [120], we obtain the analytical solution of Eq. (3.32),

$$\Omega_{nn} = \frac{1}{\sqrt{3\pi^3\eta a_0}} \frac{1}{\sqrt{n}}, \quad (3.33)$$

in analogy to the Zimm approach [120, 132, 156]. Choosing for  $a_0^2$  the result of a flexible ABPO-HI, namely  $a_0^2 = 1/\mu pL + Pe^2/6\mu pL\Delta$ , where the Péclet number  $Pe$  and  $\Delta$  are defined in Eq. 1.89, and  $\mu$  is given by  $\mu = 2\nu/(3p)$ , [74] we obtain

$$\Omega_{nn} \sim \frac{\sqrt{pL\mu}}{Pe\sqrt{n}} \quad (3.34)$$

for  $Pe \gg 1$ .

In the following, when not indicated otherwise, the approximate expressions (3.31) and (3.32) are used for the calculation of the Oseen tensor. Moreover, we use  $\Delta = 1/3$ , the value of a spherical colloid of diameter  $l$  in solution.

### 3.2.3 Stretching coefficient and relaxation times

The stretching coefficient and relaxation times are interdependent and need to be determined simultaneously. Due to nonlinearities, specifically in  $\Omega_{nn}$ , the respective quantities can only be determined numerically.

We focus here on flexible polymers, where  $pL \gg 1$ , and we set  $L/l = pL$ . Then, in terms of the eigenfunction expansion (3.13), Eq. (3.8) for the stretching coefficient  $\nu$ , respectively  $\mu = 2\nu/3p$ , becomes

$$\sum_{n=1}^{\infty} \left[ \frac{k_B T \tau_n}{\pi \eta} + \frac{v_0^2 l \tilde{\tau}_n^2}{1 + \gamma_R \tilde{\tau}_n} \right] \zeta_n^2 = L, \quad (3.35)$$

with the relaxation times (Eq. (3.23))

$$\tilde{\tau}_n = \frac{\tau_R}{\mu n^2 (1 + 3\pi \eta \Omega_{nn})}, \quad (3.36)$$

where  $\tau_R \equiv \eta L^2 / (\pi k_B T p)$  is the Rouse relaxation time [88, 132]. In the non-hydrodynamic case, i.e.,  $\Omega_{nn} = 0$ , we find the asymptotic solution  $\mu = Pe^{4/3}/6\Delta$  of Eq. (3.35), independent of  $pL$ . [74] For the relaxation times, we recover the Zimm behavior  $\tilde{\tau}_n = \tau_Z/n^{3/2}$  at  $Pe = 0$ , with the longest relaxation time  $\tau_Z = \eta(L/p)^{3/2}/(\sqrt{3\pi}k_B T)$  (Zimm relaxation time).

The scaled stretching coefficient,  $\mu$ , is presented in Fig. 4.7 as a function of the Péclet number. For the considered polymer lengths and stiffness,  $\mu$  is independent of  $pL$ . Moreover, it increases approximately linearly with Péclet number for  $Pe \gtrsim 5$ , somewhat weaker than  $\mu$  of comparable passive polymers. Hence, hydrodynamics modifies the stretching coefficient.

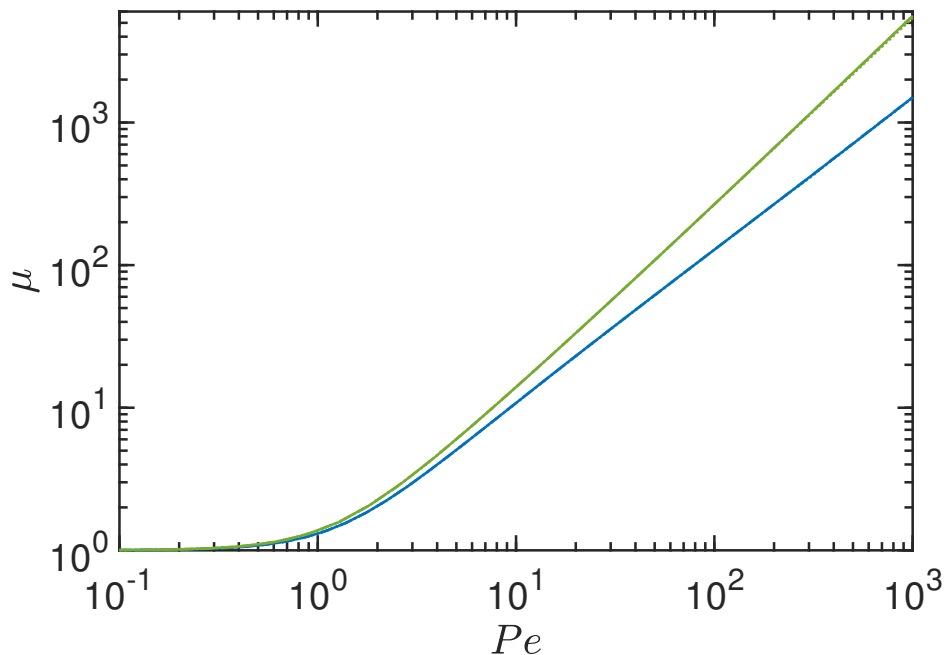


Fig. 3.6 Normalized stretching coefficient  $\mu = 2\nu/(3p)$ , solution of Eq. (3.35), as function of the Péclet number  $Pe$  for flexible polymers with  $pL = 10^3, 10^4$ , and  $10^5$  without HI (green) and with HI (blue). The results are independent of polymer length.

Figure 3.7 displays longest relaxation times,  $\tilde{\tau}_1$ , as function of  $Pe$ . For  $1 < Pe \lesssim 10$ , hydrodynamic interactions enhance the decay of the relaxation time with increasing  $Pe$  compared to the non-hydrodynamic case, specifically for  $pL > 10^3$ . Note that  $\mu \sim Pe$ , independent of the polymer length in the considered length regime. This is a consequence of an increase of  $\Omega_{nn}$  with increasing  $Pe$  (cf. Appendix A). In contrast, a slower decay of  $\tilde{\tau}_1$  is obtained for  $Pe > 10$ . Here, we find a strong polymer-length dependence, which is related to particular values of  $\Omega_{nn}$  (cf. Fig. B.1). The approximation (3.34) yields the relation  $\tilde{\tau}_1 \sim 1/\sqrt{Pe}$  for  $3\pi\eta\Omega_{nn} \gg 1$ , which describes the Péclet number dependence well in the interval  $10 < Pe < 10^3$  for  $pL = 10^5$ . As shown in Fig. B.1 for shorter polymers,  $\Omega_{nn}$  varies more slowly with  $Pe$  and, hence,  $\tilde{\tau}_1$  decays faster with increasing  $Pe$ . In the limit  $Pe \rightarrow \infty$ ,  $\Omega_{nn}$  becomes very small and the contribution to the relaxation times vanishes gradually. Hence,  $\tilde{\tau}_1$  approaches the asymptotic dependence  $\tilde{\tau}_1 \sim 1/Pe$ , determined by  $\mu$ .

## 3.2 Analytical model of active Brownian polymer in solution

Results on the mode-number dependence of the relaxations times for various  $Pe$  are presented in Appendix C. The intricate dependence of  $\Omega_{nn}$  on the relaxation times poses a major challenge for an (approximate) analytical solution, a problem we were not able to overcome so far.

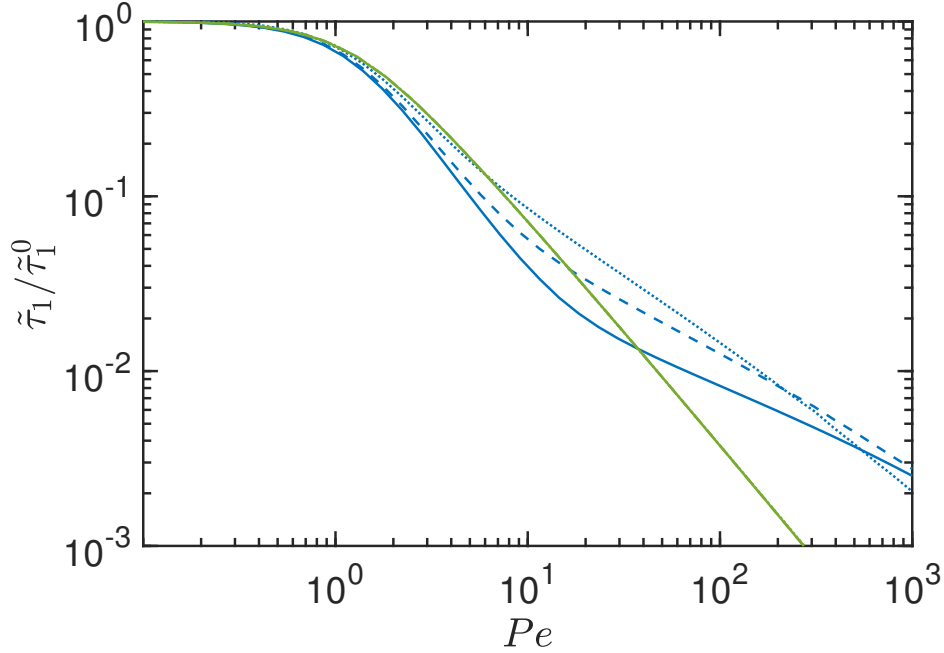


Fig. 3.7 The longest polymer relaxation time  $\tilde{\tau}_1$ , Eq. (3.36), normalized by the corresponding passive value  $\tilde{\tau}_1^0$  as function of the Péclet number  $Pe$  for flexible polymers with  $pL = 10^5$  (solid),  $10^4$  (dashed), and  $10^3$  (dotted). The green line shows the result of an active polymer in absence of HI, where  $\tau_1 \sim Pe^{-4/3}$ .

### 3.2.4 Conformational properties

The conformational properties of a polymer are characterized by the mean square end-to-end distance  $\langle \mathbf{r}_e^2 \rangle = \langle (\mathbf{r}(L/2) - \mathbf{r}(-L/2))^2 \rangle$ , which is given by

$$\langle \mathbf{r}_e^2 \rangle = \frac{8}{L} \sum_{n, \text{odd}} \left( \frac{k_B T \tau_n}{\pi \eta} + \frac{v_0^2 l \tilde{\tau}_n^2}{1 + \gamma_R \tilde{\tau}_n} \right) \quad (3.37)$$

in terms of the mode amplitudes of Eq. (3.29). Numerical results for  $\langle \mathbf{r}_e^2 \rangle$  of flexible polymers ( $pL \gg 1$ ) are shown in Fig. 3.8 for various polymer lengths. Starting from the equilibrium value  $\langle \mathbf{r}_e^2 \rangle = L/p$  at  $Pe = 0$ , ABPOs+HI first shrink with increasing activity and then swell for higher  $Pe$  (solid lines), in qualitative agreement with the simulation results of Sec. 3.1.2. In the asymptotic limit  $Pe \rightarrow \infty$ , a limiting value

$\langle r_e^2 \rangle < L^2$  is assumed. Thereby, the shrinkage strongly depends on the polymer length and is more pronounced for longer polymers. As shown in Fig. 3.8, flexible ABPO-HI exhibit a drastically different behavior and swell monotonically with increasing activity. The reason for the qualitatively different conformational properties rests on the different polymer-length dependence of the Rouse and Zimm relaxation times, where  $\tau_R/\tau_Z \approx \sqrt{pL}$ . Hence, in the presence of hydrodynamic interactions, relaxation times are shorter by the factor  $1/\sqrt{pL}$ , which can be orders of magnitude for long flexible polymers.

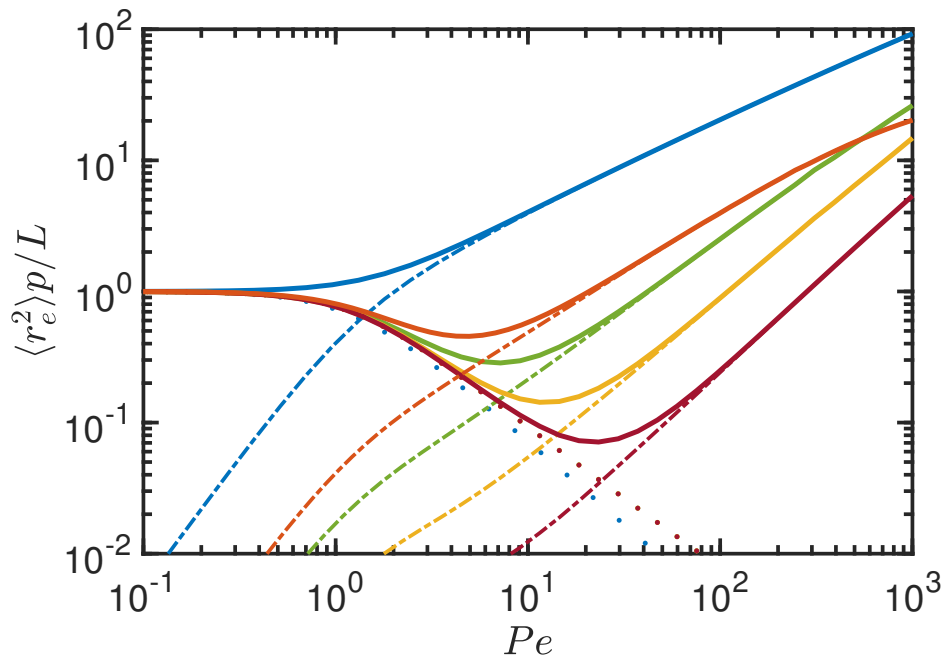


Fig. 3.8 Polymer mean square end-to-end distance  $\langle r_e^2 \rangle$ , Eq. (3.37), as a function of the Péclet number  $Pe$  for flexible ABPOs+HI of length  $pL = 2 \times 10^2$  (orange),  $10^3$  (green),  $10^4$  (yellow), and  $10^5$  (magenta). The blue lines correspond to a free-draining flexible polymer with  $pL = 50$ . The dotted curves represent the contribution with the relaxation times  $\tau_n$  and the dashed-dotted curves that with  $v_0^2$  of Eq. (3.37), respectively.

Hydrodynamic interactions lead to a polymer-length dependence of the swelling with increasing Péclet number ( $Pe \ll \infty$ ), as shown in Fig. 3.8. For polymer lengths in the range  $pL \approx 10^2 - 10^3$ ,  $\Omega_{nn}$  depends only weakly on the mode number (cf. Fig. B.1), hence, replacement of the relaxation times  $\tilde{\tau}_n$  by the relaxation times  $\tau_Z/n^{3/2}$  yields

$$\langle r_e^2 \rangle = \frac{L}{p\mu} \left[ 1 + \frac{4Pe^2}{(3\pi)^{3/2} \Delta \sqrt{pL}} \left( 1 - \frac{1}{2\sqrt{2}} \zeta(3/2) \right) \right], \quad (3.38)$$

### 3.2 Analytical model of active Brownian polymer in solution

---

in the limit  $\gamma_R \tilde{\tau}_n \gg 1$ , where  $\zeta(x)$  is Riemann's zeta function ( $\zeta(3/2) \approx 2.61$ ). In the limit of very large  $pL$  and  $Pe \gg 1$ , at least in the vicinity of  $pL = 10^5$ ,  $\tilde{\tau}_n$  can be approximated by  $\Omega_{nn}$  of Eq. (??), which yields

$$\langle \mathbf{r}_e^2 \rangle \sim \frac{L}{p\mu} \frac{Pe^3}{\sqrt{\mu pL}}. \quad (3.39)$$

Thus, we find the same dependence on  $pL$  for both, small and large  $pL$ , and  $\langle \mathbf{r}_e^2 \rangle / L^2$  decreases as  $1/(pL)^{3/2}$ . The dependence on  $Pe$  changes from  $\langle \mathbf{r}_e^2 \rangle \sim Pe$  for  $pL \approx 10^2 - 10^3$  to  $\langle \mathbf{r}_e^2 \rangle \sim Pe^{3/2}$  for  $pL \approx 10^5$ , because  $\mu \approx Pe$ . For an ABPO-HI, we found instead  $\langle \mathbf{r}_e^2 \rangle \sim LPe^{2/3}/p$ , [74] since for such a polymer  $\mu \sim Pe^{4/3}$ . Hence, hydrodynamic interactions lead to a qualitative different  $Pe$  dependence.

Figure 3.8 shows the individual contributions to  $\langle \mathbf{r}_e^2 \rangle$ —the term with the relaxation times  $\tau_n$  (dotted lines) and that with  $v_0^2$  (dashed-dotted lines) in Eq. (3.37), respectively. The initial shrinkage of  $\langle \mathbf{r}_e^2 \rangle$  with increasing  $Pe$  is caused by the decreasing relaxation times  $\tau_n \sim 1/\mu$  with increasing activity. In the thermal contribution of Eq. (3.38),  $\langle \mathbf{r}_e^2 \rangle \sim L/(p\mu)$ , the stretching coefficient  $\mu$  increases with increasing activity, which formally implies a decreasing persistence length below the value of a passive polymer, corresponding to more compact conformations than of the passive case. The  $v_0^2$ -dependent term causes a swelling of the polymer. For an ABPO-HI, the competing effects lead to an overall swelling, since swelling exceeds shrinkage. In case of an ABPO+HI, swelling is weaker due to fluid-induced collective motion (cf. Fig. 3.1) compared to the random motion of an ABPO-HI, and  $\langle \mathbf{r}_e^2 \rangle$  assumes a minimum. Mathematically, this is reflected by the shorter relaxation times  $\tilde{\tau}_n$  compared to  $\tau_n$ . Hydrodynamic interactions accelerate the polymer dynamics and higher  $Pe$  are required to achieve a significant swelling of an ABPO+HI.

The exponents of the (approximate) power-law regimes for the various  $pL$  values approximately exhibit the above predicted scaling relations with respect to  $Pe$  ( $Pe > 10$ ). The shift of the dashed-dotted curves in Fig. 3.8 to smaller  $\langle \mathbf{r}_e^2 \rangle$  with increasing polymer length,  $pL$ , reflects the discussed decrease in relaxation times by hydrodynamics.

Figure 3.9 shows a comparison of analytical and simulation results. We find good agreement for short polymers ( $N_m = 50$ ), but theory yields a less pronounced shrinkage for the longer polymers. We like to emphasize that for an ABPO-HI the theoretical approach reproduces the simulation data very well. [117] The reason of the discrepancy is not evident, but is related to the applied approximations, which seem to underestimate hydrodynamic effects. We speculate that the preaveraging approximation may fail, because active fluctuations could be large and the replacement of  $\mathbf{H}(\mathbf{r} - \mathbf{r}')$  by  $\langle \mathbf{H}(\mathbf{r} - \mathbf{r}') \rangle$  no longer be justified. Yet, the analytical expression captures the qualitative behavior, and even more quantitatively the swelling behavior at large

$Pe$  is reasonably well reproduced, although the asymptotic value for  $Pe \rightarrow \infty$  is somewhat overestimated due to the applied mean-field approximation of the bond-length constraint.

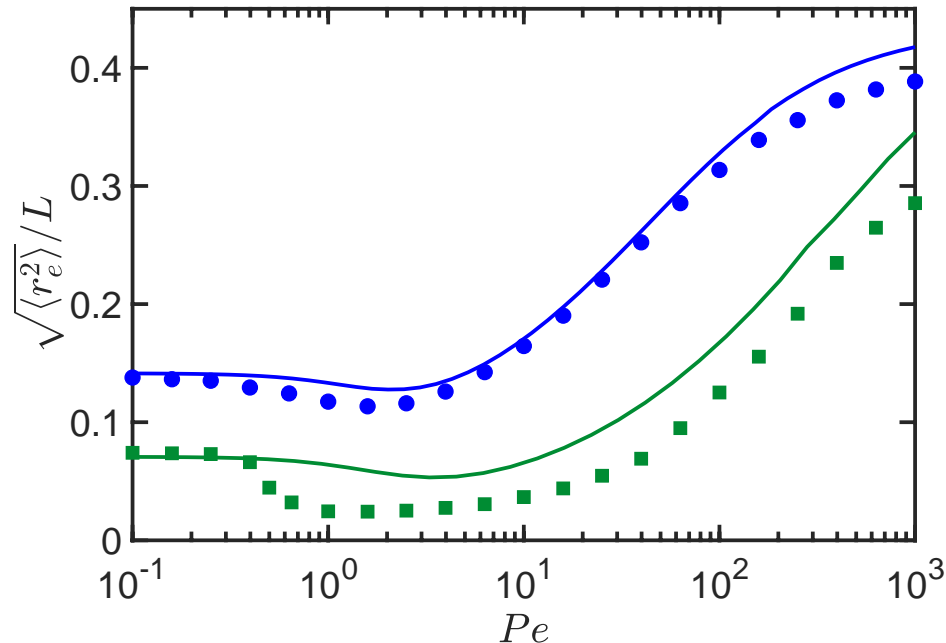


Fig. 3.9 Mean square end-to-end distance as a function of the Péclet number of flexible ABPOs+HI for the monomer number  $N_m = 50$  ( $pL = 50$ ) (blue) and  $N_m = 200$  ( $pL = 200$ ) (green). Solid lines correspond to analytical and symbols to simulation results.

### 3.2.5 Dynamical properties

The dynamics of the polymers is characterized by the site mean square displacement (MSD) averaged over the polymer contour,  $\langle \overline{\Delta \mathbf{r}^2}(t) \rangle = \int \langle (\mathbf{r}(s, t) - \mathbf{r}(s, 0))^2 \rangle ds/L$ , which yields

$$\langle \overline{\Delta \mathbf{r}^2}(t) \rangle = \langle \Delta \mathbf{r}_{cm}^2(t) \rangle + \langle \overline{\Delta \mathbf{r}_0^2}(t) \rangle + \langle \overline{\Delta \mathbf{r}_a^2}(t) \rangle, \quad (3.40)$$

with the center-of-mass mean square displacement

$$\langle \Delta \mathbf{r}_{cm}^2(t) \rangle = \frac{6k_B T}{L} H_{00} t + \frac{2v_0^2 l}{\gamma_R^2 L} (\gamma_R t - 1 + e^{-\gamma_R t}), \quad (3.41)$$

### 3.2 Analytical model of active Brownian polymer in solution

---

$H_{00} = (1 + 3\pi\eta\Omega_{00})/(3\pi\eta)$ , the activity-modified equilibrium internal-dynamics contribution

$$\langle \overline{\Delta \mathbf{r}_0^2(t)} \rangle = \frac{1}{L} \sum_{n=1}^{\infty} \frac{6k_B T \tau_n}{\gamma} (1 - e^{-t/\tilde{\tau}_n}) , \quad (3.42)$$

and the active contribution

$$\langle \overline{\Delta \mathbf{r}_a^2(t)} \rangle = \frac{1}{L} \sum_{n=1}^{\infty} \frac{2v_0^2 l \tilde{\tau}_n^2}{1 + \gamma_R \tilde{\tau}_n} \left( 1 - \frac{e^{-\gamma_R t} - \gamma_R \tilde{\tau}_n e^{-t/\tilde{\tau}_n}}{1 - \gamma_R \tilde{\tau}_n} \right). \quad (3.43)$$

Remarkably, in the center-of-mass MSD only the thermal contribution includes hydrodynamics, via  $H_{00}$  [131], which depends on activity through  $\mu$ , whereas the active term is identical with that of an ABPO-HI [74, 76, 86]. The reason is that swimming is force free and no Stokeslet is present. Within the approximation  $a^2(s, s') \approx a^2(s - s')$ , Eq. (3.32) yields

$$\Omega_{00} = \frac{8}{3\sqrt{6}\pi^3\eta a_0}. \quad (3.44)$$

Hence, for  $3\pi\eta\Omega_{00} \gg 1$ , the thermal center-of-mass diffusion coefficient  $D_0 = k_B T \Omega_{00}/L$  increases somewhat due to activity in the range  $1 \lesssim Pe \lesssim 50$ , and decreases for higher  $Pe$  (cf. Fig. B.1).

In the asymptotic limit  $Pe \rightarrow \infty$ , the active polymer is stretched, and the hydrodynamic contribution to thermal diffusion decreases (cf. Fig. App.B). As for a passive, rodlike polymer [91, 132, 155], asymptotically hydrodynamic interactions yield only small corrections with respect to the polymer-length dependence of a non-hydrodynamic (free-draining) polymer.

Figure 3.10 displays the average site mean square displacement for various Péclet numbers. For a passive flexible polymer, we recover the well-known Zimm behavior, with  $\langle \overline{\Delta \mathbf{r}_0^2(t)} \rangle \sim t^{2/3}$  for  $t/\tau_Z \ll 1$ , and a crossover to free diffusion for  $t/\tau_Z \gg 1$  [131, 132, 156].

In the presence of activity, four time regimes can be identified,

- $t \rightarrow \infty$  — The MSD is dominated by the linear time dependence of the center-of-mass dynamics, with the diffusion coefficient

$$D = \frac{k_B T H_{00}}{L} + \frac{v_0^2 l}{3\gamma_R L}. \quad (3.45)$$

The other terms approach a constant value equal to  $2\langle \mathbf{r}_g^2 \rangle$ , where  $\langle \mathbf{r}_g^2 \rangle$  is the active-polymer radius of gyration. The simulations results are in agreement with the active contribution to  $D$ .

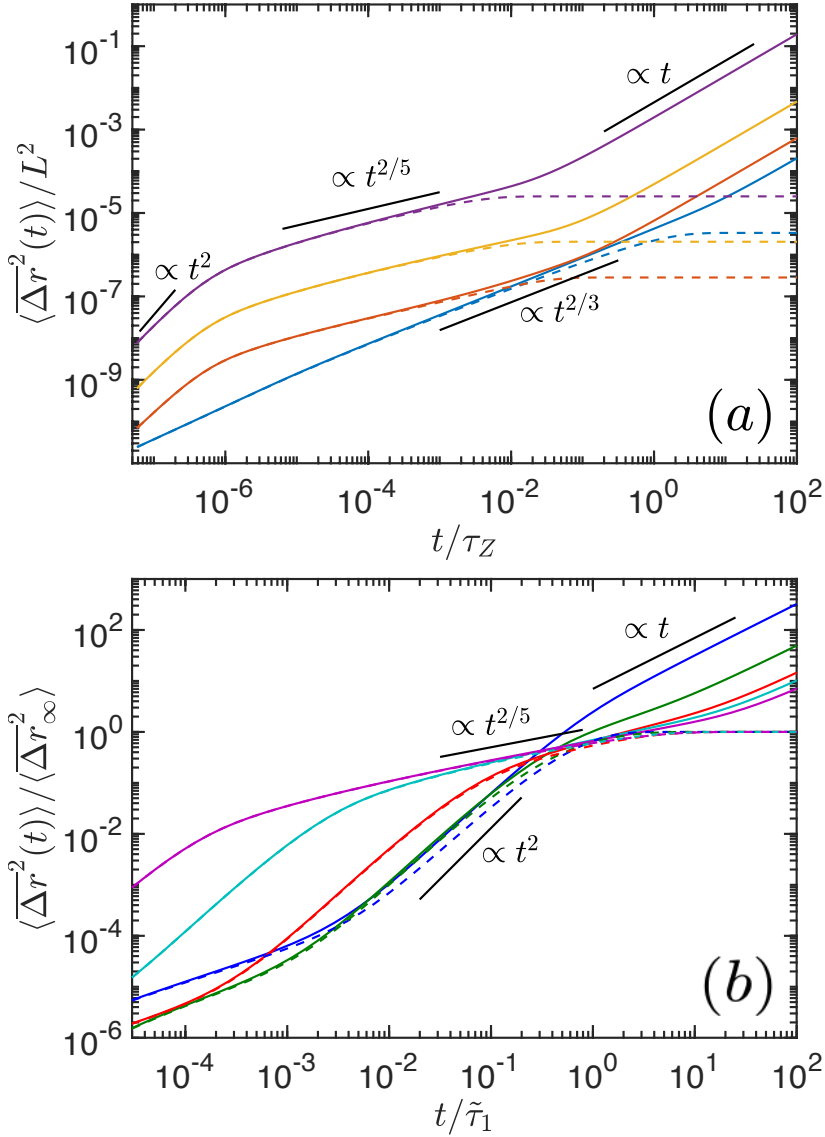


Fig. 3.10 Mean square displacement of flexible ABPO+HI, Eq. (3.40). (a) MSDs for the Péclet numbers  $Pe = 10^{-2}$  (blue),  $Pe = 2 \times 10^1$  (orange),  $Pe = 1.5 \times 10^2$  (yellow), and  $Pe = 10^3$  (purple); the polymer length is  $pL = 10^5$ . The time is scaled by the Zimm time  $\tau_Z$  of a passive polymer. (b) MSDs for the polymer lengths  $pL = 5 \times 10^1$  (blue),  $2 \times 10^2$  (green),  $10^3$  (red),  $10^4$  (cyan), and  $10^5$  (purple) and  $Pe = 10^2$ .  $\langle \overline{\Delta r^2}_\infty \rangle = 2\langle r_g^2 \rangle$  denotes the asymptotic value of the MSD in the center-of-mass reference. The dashed lines correspond to the MSD in the polymer center-of-mass reference frame, Eqs. (3.42) + (3.43), and the solid lines to the overall MSD, Eq. (3.40). The black lines indicate power laws in the respective regimes.

- $t / \tilde{\tau}_1 \ll 1 \ll \gamma_R t$  — The active contribution to the MSD is dominated by ( $\gamma_R \tilde{\tau}_1 \gg 1$ )

$$\langle \overline{\Delta r_a^2}(t) \rangle = \frac{2v_0^2 l}{\gamma_R L} \sum_{n=1}^{\infty} \tilde{\tau}_n (1 - e^{-t/\tilde{\tau}_n}). \quad (3.46)$$

### 3.2 Analytical model of active Brownian polymer in solution

---

With the power-law dependence  $\tilde{\tau}_n = \tilde{\tau}_1/n^{\tilde{\alpha}}$  of the relaxation time and by replacing the sum by an integral, we find

$$\langle \overline{\Delta \mathbf{r}_a^2(t)} \rangle = \frac{2v_0^2 l \tilde{\tau}_1}{\gamma_R L} \left( \frac{t}{\tilde{\tau}_1} \right)^{1-1/\tilde{\alpha}} \int_0^\infty dx \frac{1 - e^{-x\tilde{\alpha}}}{x^{\tilde{\alpha}}}. \quad (3.47)$$

With the assumption  $3\pi\eta\Omega_{11} \gg 1$  and Eq. (3.33), which corresponds to the exponent  $\tilde{\alpha} = 3/2$ , Eq. (3.47) yields

$$\langle \overline{\Delta \mathbf{r}_a^2(t)} \rangle \sim \frac{L^2 P e^{5/3}}{(pL)^2} t^{1/3}, \quad (3.48)$$

i.e., a site sub-diffusive MSD dominated by the internal polymer dynamics. The exponent  $\alpha' = 1 - 1/\tilde{\alpha} = 1/3$  of Eq. (3.48) approximately agrees with the full numerical result  $2/5$  (cf. Fig. 3.10). Note that the exponent  $\tilde{\alpha}$  ( $\tilde{\tau}_n \sim 1/n^{\tilde{\alpha}}$ ) is in fact larger than  $\tilde{\alpha} = 3/2$  for most  $Pe$  (cf. mode-number dependence of relaxations in Fig. C.1), which leads to an exponent  $\alpha'$  somewhat larger than  $\alpha' = 1/3$ , consistent with the results of Fig. 3.10, where we find  $\alpha' \approx 2/5$ . Figure 3.10(b) emphasizes the universality of the internal dynamics with increasing  $pL$ . The various curves, especially for the MSD in the center-of-mass reference frame, asymptotically approach a power-law regime with an exponent close to the predicted value. This polymer specific regime is evidently only pronounced for  $pL \gtrsim 10^3$ . Hence, it is not clearly visible in Fig. 3.5 of the MSD obtained from simulations.

- $t/\tilde{\tau}_1, \gamma_R t \ll 1$  — Taylor expansion of the exponential functions in Eq. (3.43) yields

$$\langle \overline{\Delta \mathbf{r}_a^2(t)} \rangle = \frac{v_0^2 l \gamma_R}{L} \sum_{n=1}^{\infty} \frac{\tilde{\tau}_n}{1 + \gamma_R \tilde{\tau}_n} t^2, \quad (3.49)$$

consistent with the observed ballistic regime in Fig. 3.10. This regime and its dependence on activity and polymer properties is in quantitative agreement with the simulation results of Fig. 3.5.

- $t \rightarrow 0$  — The MSD is dominated by Eq. (3.42), and all modes contribute. Setting  $\tilde{\tau}_n = \tilde{\tau}_1/n^{3/2}$  and replacing the sum by an integral yields

$$\langle \overline{\Delta \mathbf{r}_0^2(t)} \rangle = \frac{2L}{\pi^2 p \mu} \left( \frac{t}{\tilde{\tau}_1} \right)^{2/3} \int_0^\infty dx \frac{1 - e^{-x^{3/2}}}{x^2}. \quad (3.50)$$

This is the same relation as obtained for a passive system, except that  $\mu$  and  $\tilde{\tau}_1$  depend on activity. With Eq. (3.34), we find the Péclet-number dependence  $\langle \overline{\Delta \mathbf{r}_0^2(t)} \rangle \sim Pe^{-2/3} (t/\tau_Z)^{2/3}$  for  $Pe \gtrsim 50$  and  $pL \gg 1$ .

### 3.3 Conclusions and discussion

Two stochastic processes determine the size and shape of an ABPO+HI—thermal and active fluctuations. Due to the linearity of the analytical equations of motion and the additivity of the noise, the fluctuations lead to additive contributions to the mean square end-to-end distance, which are, however, coupled by the inextensibility of the polymer. The active fluctuations yield a contribution quadratic in the propulsion velocity (or Péclet number), similar to the quadratic dependence of the MSD of an ABP [1, 2], which leads to a swelling of the polymer, however, with a  $Pe$  dependence smaller than quadratic due to the increase of the stretching coefficient with increasing  $Pe$ . The polymer inextensibility implies enhanced fluctuations of the thermal part of  $\langle \mathbf{r}_e^2 \rangle$  by the active noise—expressed by the factor  $\mu$ —corresponding to a decreasing persistence length with increasing activity associated with a shrinkage of the polymer size.

Qualitatively, the behavior can be understood as follows. An increasing activity yields an increasing persistent displacement  $l_m/l = v_0/\gamma_R l = Pe/2$  of a monomer before it changes its propulsion direction. Hence, any disparity in the propulsion direction is amplified by an increasing  $Pe$  and leads to, in average, divergent monomer trajectories and an increasing intramolecular tension reflected in the increasing stretching coefficient  $\mu$ . For an ABPO-HI, the competing shrinkage of the thermal part and swelling of the active contribution leads to an overall swelling, since swelling exceeds shrinkage. In case of an ABPO+HI, the reduced swelling can descriptively be understood by fluid-induced collective motions compared to random motions in absence of HI (cf. Fig. 3.1). Mathematically, this is reflected by the shorter relaxation times  $\tilde{\tau}_n$  compared to  $\tau_n$ . To achieve a swelling of an ABPO+HI comparable to that of an ABPO-HI requires larger Péclet numbers. As a consequence,  $\langle \mathbf{r}_e^2 \rangle$  of an ABPO+HI assumes a minimum at intermediate  $Pe$ .

As mentioned several times, we do not take into account swimmer-specific flow fields of individual monomers. Nonetheless, the intramolecular forces create complex flow fields—from single monomers to the full filament. Already for a pair of monomers, forces along their bond vector constitutes a force dipole, aside from a potential Stokeslet. In fact, such a force-dipole field could also exist for a passive polymer, but the stronger forces of active monomers increase the dipole field and its relevance for the polymer dynamics significantly. Hence, on larger length scales, embracing more monomers, the overall flow field is rather complex and a large number of hydrodynamic multipoles contribute. This dynamically emerging multipoles are a particular feature of ABPOs+HI and, in their sum, lead to the observed polymer shrinkage.

To unravel the influence higher-order multipole flow fields, we currently perform mesoscale hydrodynamic simulations of short linear chains of connected squirmers

(monomers).[85] Preliminary results of squirmers without active stress (neutral squirmers) reveal a weak influence of higher-order multipoles on the polymer conformations and dynamics. A markedly stronger effect appears for monomers with finite active stress (puller/pusher), where polymer conformational and dynamical properties depend on the strength of higher-order multipoles. In general, the individual multipolar contributions depend on the particular propulsion mechanism, and, thus, their inclusion can be essential to capture the relevant hydrodynamic flow fields for an adequate description of the polymer properties.

The polymer dynamics is determined by two relaxation processes, the orientational relaxation of an active site/monomer, and the polymer relaxation. This leads to distinct time regimes in the polymer mean square displacement. At short times  $t/\tilde{\tau}_1, \gamma_R t \ll 1$ , activity leads to a ballistic regime, with an enhanced dynamics compared to a passive polymer. For  $t/\tilde{\tau}_1 \ll 1 \ll \gamma_R t$ , the MSD is dominated by the internal dynamics, and a polymer-characteristic subdiffusive regime appears. Again, activity and hydrodynamics play a decisive role, leading to a power-law dependence with an exponent,  $\alpha' \approx 2/5$ , smaller than that of a passive hydrodynamic polymer. In the asymptotic limit of long times, the enhanced diffusive dynamics is no longer affected by the fluid motion, but rather becomes identical to that of an ABPO-III.



## Chapter 4

# Characteristics of active polymers in solution by external colored noise

In this article, we explore the effect of external colored noise, resembling an active environment, on the properties of semiflexible polymers in dilute solution by hydrodynamic simulations and analytical theory. The active polymer is specific in so far as the polymer is not force free, as it would be the case for a polymer with self-propelled monomers [54, 116], and the active forces give rise to a Stokeslet flow. We analyze the influence of the additional flow field, in comparison to a self-propelled polymer, on the conformational and dynamical polymer properties in presence of HI. We like to emphasize that for an active polymer in absence of HI, their properties for externally driven and self-propelled monomers are identical [74]. In the presence of hydrodynamic interactions, the behavior of polymers with self-propelled, active Brownian particle-type monomers differs qualitatively from that of polymers with externally, by colored noise forces, driven monomers. Here, simulation and theoretical results for polymers in solution in the presence of external active noise are presented. In simulations, a semiflexible bead-spring polymer chain is considered, analytically, a continuous linear semiflexible polymer. Activity is taken into account by independent site velocities, with orientations changing in a diffusive manner. In simulations, hydrodynamic interactions (HI) are taken into account by the Rotne-Prager-Yamakawa tensor or an implementation of the active polymer in the multiparticle collision dynamics approach for fluids. To arrive at an analytical solution, the preaveraged Oseen tensor is used. The active process implies a dependence of the stationary-state properties on HI via polymer relaxation times.

We will show how our studies reveal a decisive influence of hydrodynamic interactions and their origin on the polymer conformations and dynamics. With increasing activity, HI lead to an enhanced swelling of flexible polymers, and the conformational properties differ substantially from those of polymers with self-propelled monomers in

presence of HI or free-draining polymers. The polymer mean square displacement is enhanced by HI. Over a wide range of time scales, hydrodynamics leads to a subdiffusive regime for flexible active polymers, with an exponent larger than that of the Rouse and Zimm models of passive polymers.

## 4.1 Computer simulations

### 4.1.1 Model of active polymer

The semiflexible polymer is composed of  $N_m$  active Brownian particles ( $i = 1, \dots, N_m$ ), which are linearly connected by a harmonic bond potential  $U_l$ , given by Eq. (1.86), experiencing bond-orientational restrictions by the bending potential  $U_b$  given by Eq. (1.87), and excluded-volume interactions are taken into account by the purely repulsive Lennard-Jones potential  $U_{LJ}$  given by Eq. (1.88).

In addition, every monomer experience an active force

$$\mathbf{F}_i^a = F^a \mathbf{e}_i(t) \quad (4.1)$$

of constant magnitude  $F^a$ . We consider this as an external force in contrast to the self-propulsion force of Ref. [116]. As a consequence, an individual monomer in a fluid is no longer force free, but the active force gives rise to a Stokeslet [1]. As for an active Brownian particle, we set  $F^a = \gamma v_0$ , with the friction coefficient  $\gamma = 3\pi\eta d_H$  of the surrounding fluid— $\eta$  is the fluid viscosity and  $d_H$  the monomer hydrodynamic diameter—and the active velocity  $v_0$ . The orientation  $\mathbf{e}_i$  changes in a diffusive manner according to Eq. (1.76), where  $\hat{\boldsymbol{\eta}}_i$  is Gaussian and Markovian stochastic processes with zero mean and the second moments given by Eq.(1.77).

Fluid mediated interactions are incorporated implicitly by the Rotne-Prager-Yamakawa (RPY) hydrodynamic tensor [124, 153, 154] or explicitly by modeling the fluid via the MPC approach [104, 165, 166].

### 4.1.2 Brownian dynamics with the RPY tensor

In Brownian dynamics simulations in presence of hydrodynamic interactions, the overdamped equation of motion

$$\dot{\mathbf{r}}_i(t) = \sum_{j=1}^{N_m} \mathbf{H}_{ij} [\mathbf{F}_i^a + \mathbf{F}_i + \boldsymbol{\Gamma}_i(t)] \quad (4.2)$$

is considered. The forces  $\mathbf{F}_i = -\nabla_{\mathbf{r}_i}(U_l + U_b + U_{LJ})$  follow from the potentials (1.86)-(1.88), and  $\boldsymbol{\Gamma}_i$  accounts for thermal fluctuations.  $\boldsymbol{\Gamma}_i$  is a Gaussian and Markovian

stochastic processes with zero mean and the second moments

$$\langle \mathbf{\Gamma}_i(t) \mathbf{\Gamma}_j^T(t') \rangle = 2k_B T \mathbf{H}_{ij}^{-1} \delta(t - t'), \quad (4.3)$$

where  $\mathbf{\Gamma}_i^T$  denotes the transpose of  $\mathbf{\Gamma}_i$  and  $\mathbf{H}_{ij}^{-1}$  the inverse of  $\mathbf{H}_{ij}$ . The hydrodynamic tensor,  $\mathbf{H}_{ij}(\mathbf{r}_{ij})$ , is given by

$$\mathbf{H}_{ij}(\mathbf{r}_{ij}) = \frac{\delta_{ij}}{3\pi\eta d_H} \mathbf{I} + (1 - \delta_{ij}) \mathbf{\Omega}(\mathbf{r}_{ij}), \quad (4.4)$$

where the first term on the right-hand side accounts for local friction and the RPY tensor  $\mathbf{\Omega}(\mathbf{r}_{ij})$  for inter-particle interactions [116, 132, 155]. The RPY tensor ensures the positive definiteness of the hydrodynamic tensor even at small distances. The translational equations of motion (4.2) are solved via the Ermark-McCammon algorithm [101, 102]. The procedure to solve the equations of motion (1.76) for the orientation vector is described in Ref. [122].

The active noise, quantified by the dimensionless Péclet number [74, 125] and the ratio between translational,  $D_T = k_B T / 3\pi\eta d_H$ , and rotational diffusion,  $D_R$ , of a single monomer are denoted as

$$Pe = \frac{v_0}{l D_R}, \quad \Delta = \frac{D_T}{d_H^2 D_R}. \quad (4.5)$$

As for the self-propelled polymers, we choose the coefficient (Eq. (1.86)) for the bond strength  $\kappa_b l^2 / k_B T = (10 + 2Pe) 10^3$ , in order to avoid bond stretching with increasing activity. Thus, we keep bond-length variations are smaller than 3% of the equilibrium value  $l$ . Also, the scaled bending force coefficient  $\tilde{\kappa}_b = \kappa_b l^2 / k_B T$  (Eq. (1.87)) is related to the polymer persistence length,  $l_p = 1/(2p)$ , given by Eq. (1.90), and  $\sigma = 0.8l$  and  $\epsilon = k_B T$  are the truncated and shifted Lennard-Jones potential parameters, respectively.

### 4.1.3 Active polymer in MPC fluid

#### Polymer dynamics

Every monomer bead is exposed to an active forces  $\mathbf{F}_i^a = v_0 \mathbf{e}_i(t)$ , hence, a polymer experiences the total external force

$$\mathbf{F}^a = \sum_{i=1}^{N_m} \gamma v_0 \mathbf{e}_i(t) = \frac{Pe}{d_H \Delta} \sum_{i=1}^{N_m} \mathbf{e}_i(t), \quad (4.6)$$

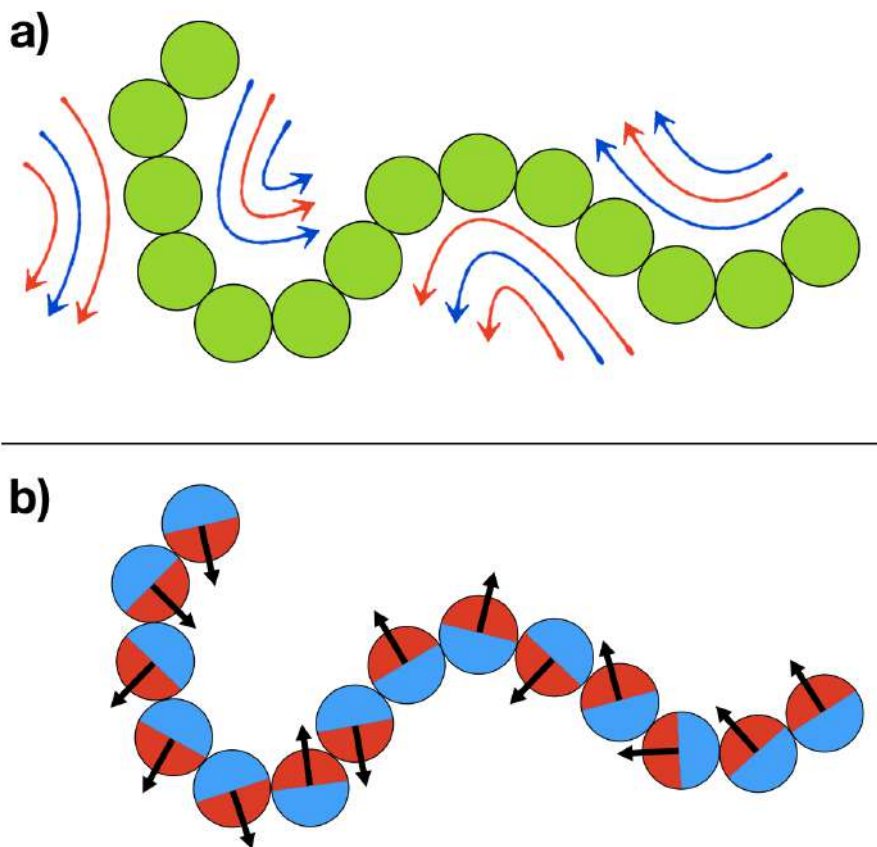


Fig. 4.1 a) Illustration of a passive polymer made out of monomers (green) surrounded by an active fluid (flow field lines shown in blue). ABPs push the polymer with a certain persistence and induce active correlations that decay exponentially with time to the monomers velocities. b) Illustration of an active polymer (ABPO), in which the monomers are represented by ABPs, in a passive fluid.

which drags along fluid and induces an overall fluid flow [167]. In a confined systems with walls, the fluid is reflected at a wall and gives rise to fluid backflow. To prevent a net fluid flow in our system with periodic boundary conditions, we modify the equations of motion of the fluid (and the embedded polymer) in such a way that the total momentum of the system (fluid plus polymer) is zero. This implies the backflow force on a monomer:

$$\mathbf{F}_i^b = -\frac{M}{mN + MN_m} \mathbf{F}^a, \quad (4.7)$$

where  $m$  is the mass of the fluid particle,  $N$  is the total number of fluid particles, and  $M$  is the mass of a monomer. The dynamics of a monomer is then described by the

equations of motion

$$M\ddot{\mathbf{r}}_i = \mathbf{F}_i + \mathbf{F}_i^a + \mathbf{F}_i^b, \quad (4.8)$$

with the force  $\mathbf{F}_i$  following from the potentials (1.86)-(1.88). Equation (4.8) is solved by applying the velocity Verlet algorithm.

### Fluid dynamics and fluid-polymer coupling

The dynamics of the MPC fluid proceeds in two steps—streaming and collision [165, 166]. In the steaming step, Newton’s equations of a motion for fluid particles are solved in the presence of the backflow force  $\mathbf{F}_i^{bf} = m\mathbf{F}_i^b/M$  over a time interval  $h$ , denote as collision time. Since  $\mathbf{e}_i(t)$  changes very slowly in the time interval  $h$ , we apply the integration scheme

$$\mathbf{v}_k(t+h) = \mathbf{v}_k(t) - \frac{h}{mN + MN_m} \mathbf{F}^a(t), \quad (4.9)$$

$$\mathbf{r}_k(t+h) = \mathbf{r}_k(t) + h\mathbf{v}_k(t) - \frac{h^2}{2(mN + MN_m)} \mathbf{F}^a(t) \quad (4.10)$$

where  $\mathbf{r}_k(t)$  and  $\mathbf{v}_k(t)$  are the position and velocity of the MPC particle  $k$  at time  $t$ , respectively. In the collision step, particles are sorted into cubic cells of side length  $a$  of a cubic, periodic systems of volume  $V = Na^3/\langle N_c \rangle$  to define the collision environment;  $\langle N_c \rangle$  is the mean number of fluid particles in a collision cell. Subsequently, the relative velocity of each particle, with respect to the center-of-mass velocity of all the particles within the corresponding collision cell, is rotated by a constant angle  $\alpha$  around a randomly orientated axis. The orientation of the rotation axis is chosen randomly and independently for every cell and collision step. Hence, the final velocity after a MPC step is

$$\mathbf{v}_i(t+h) = \mathbf{v}_{cm}(t+h) + \mathbf{R}(\alpha) [\mathbf{v}_i(t+h) - \mathbf{v}_{cm}(t+h)], \quad (4.11)$$

where  $\mathbf{R}(\alpha)$  is the rotation matrix, and

$$\mathbf{v}_{cm} = \frac{\sum_{j=1}^{N_c} m\mathbf{v}_j + \sum_{k=1}^{N_m^c} M\mathbf{v}_k}{mN_c + MN_m^c} \quad (4.12)$$

the center-of-mass velocity of the  $N_c$  fluid particles and the  $N_m^c$  monomers within the cell of particle  $i$ . Similarly to Eq. (4.11), the velocities of the monomers are rotated, which yields the fluid-monomer coupling by MPC collisions.

Partitioning of space in collision cell implies violation of Galilean invariance, which is reinstalled by a random shift of the collision lattice at every collision step [107, 166].

In order to maintain locally a constant temperature, the Maxwell-Boltzmann scaling method is applied [114].

We measure energies in units of  $k_B T$ , lengths in units of the collision cell  $a$ , and time in units of  $\tau = \sqrt{ma^2/k_B T}$ . The MPC particle mass is set to  $m = 1$ , the monomer mass to  $M = 10m$ , and the average number of particles in a collision cell to  $\langle N_c \rangle = 10$ . A time step  $h = 0.01\sqrt{ma^2/k_B T}$  is used, which corresponds to the viscosity  $\eta = 82.14\sqrt{mk_B T/a^4}$  [107, 111, 144]. MPC is an ideal gas and, hence, its isothermal velocity of sound is  $c_T = \sqrt{k_B T/m}$ , which is unity in the units of the simulation. To realize low Mach numbers, the transport velocity of an active monomer has to be small compared to  $c_T$ . All simulations are performed in a cubic periodic box of linear size  $L = 100a$ .

In order to compare simulation results obtained via the MPC approach with the Brownian dynamics simulations using the RPY tensor, several parameters have to be adjusted. In particular, MPC simulations yield the hydrodynamic diameter  $d_H = 0.6a$  of a monomer [168, 169], which yields  $\Delta = k_B T/3\pi\eta d_H^3 D_R \approx 0.6$ .

## 4.2 Computer simulations: Results

### 4.2.1 Conformational properties

The average shape of a polymer is characterized by its the mean square end-to-end distance. Figure 4.2 displays results for phantom and self-avoiding polymers of lengths  $L = (N_m - 1)l = 49l, 149l$  and various persistence lengths  $l_p$ , where  $p = 1/2l_p$ . Evidently, flexible polymers,  $pL \gtrsim 15$ , swell monotonic with increasing Péclet number, whereas semiflexible polymers shrink at moderate  $Pe$  and swell for large  $Pe$  similarly as flexible polymers. In the asymptotic limit  $Pe \rightarrow \infty$ , the value  $\langle \mathbf{r}_e^2 \rangle \approx 2L^2/5$  is assumed. Excluded-volume interactions change the behavior in so far as  $\langle \mathbf{r}_e^2/l^2 \rangle$  starts at a larger equilibrium value. For higher  $Pe$  and swollen polymers, self avoidance becomes irrelevant.

The mean square end-to-end distances obtained for polymers embedded in a MPC solvent is compared with the simulation results applying the RPY tensor in Fig. 4.3. Evidently, we obtain quantitative agreement of the polymer conformations for the two simulation approaches, which confirms their suitability for these simulation studies. For the hybrid MPC approach, the deviations from the RPY tensor simulations appear for  $Pe \gtrsim 10^2$ . This is attribute to limitations of the MPC approach in terms of Mach and Reynolds numbers.

The structural properties of the polymer in presence of hydrodynamic interactions strongly depends on the nature of the active process. As discussed in Sec. 4.1.1,

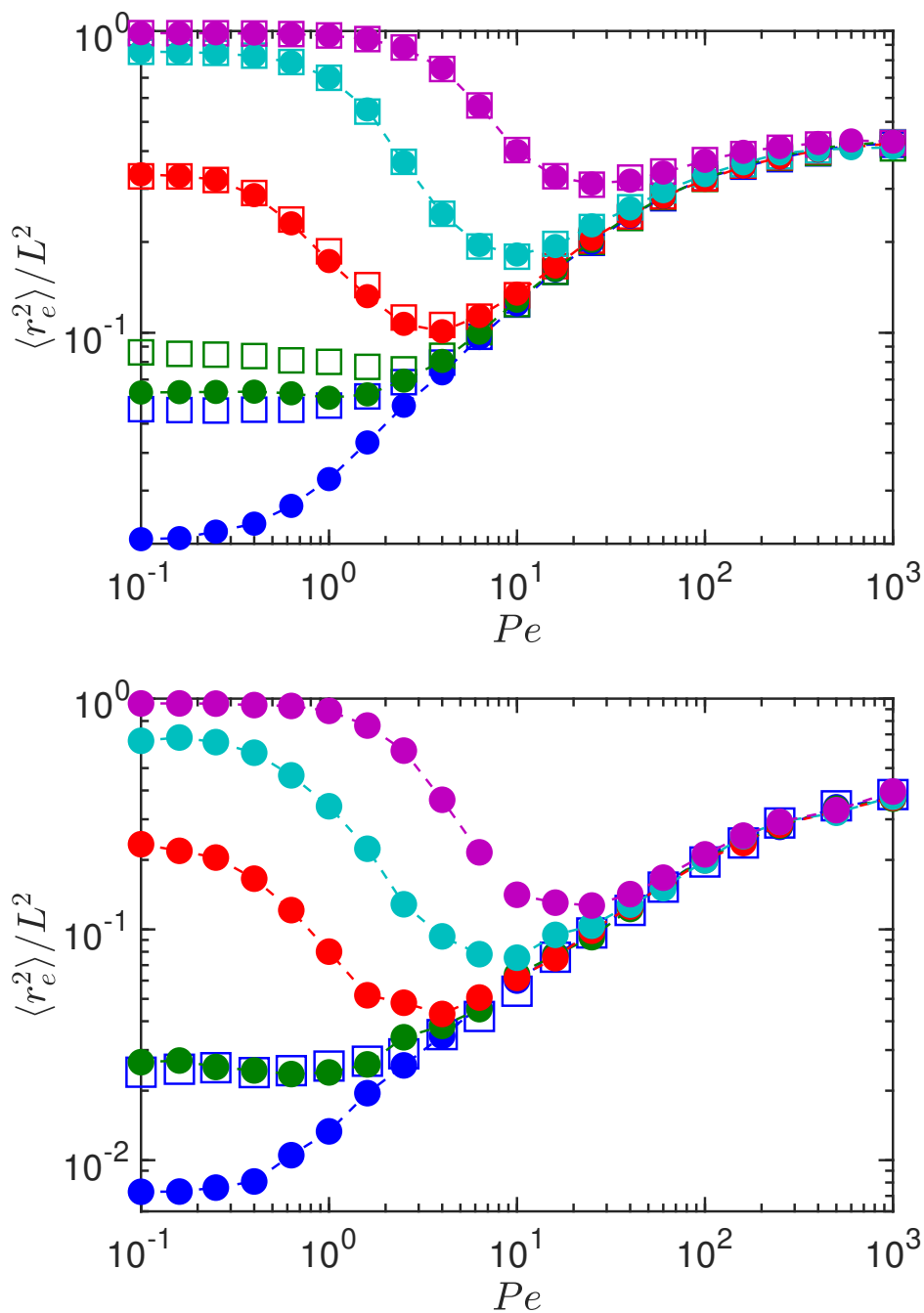


Fig. 4.2 Polymer mean square end-to-end distance as a function of the Péclet number for semiflexible polymers with (a)  $N_m = 50$  ( $L = 49l$ ) and (b)  $N_m = 150$  ( $L = 149l$ ) monomers. Bullets are results of phantom polymers and squares results of self-avoiding polymers in (a) for  $pL = 5 \times 10^1$  (blue),  $1.5 \times 10^1$  (green), 2.6 (red),  $2.5 \times 10^{-1}$  (cyan), and  $2.5 \times 10^{-2}$  (purple), and in (b) for  $pL = 1.5 \times 10^2$  (blue),  $4.5 \times 10^1$  (green), 7.5 (red),  $7.5 \times 10^{-1}$  (cyan), and  $7.5 \times 10^{-2}$  (purple). The dashed lines are guides for the eye. Hydrodynamics is taken into account by the RPY hydrodynamic tensor.

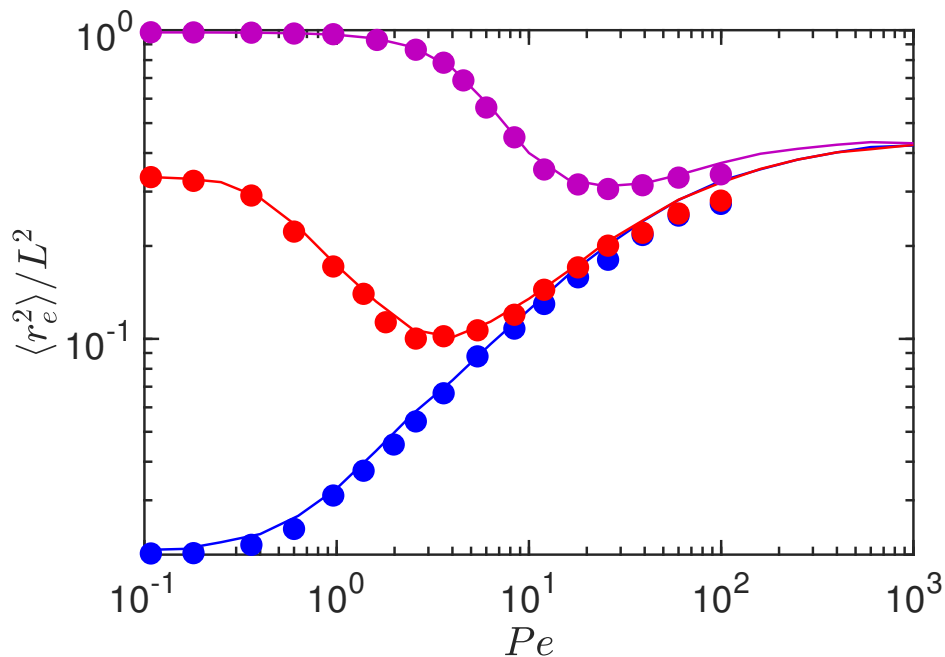


Fig. 4.3 Polymer mean square end-to-end distance as a function of the Péclet number of semiflexible polymers with  $N_m = 50$  ( $L = 49l$ ) monomers for  $pL = 5 \times 10^1$  (blue), 2.6 (red), and  $2.5 \times 10^{-2}$  (purple). Solid lines are results applying the RPY tensor and bullets are results of hybrid simulations using the MPC approach.

here, the active force is considered as an external force. Figure 4.4 shows that such an external active force leads to a significant stronger polymer swelling than intrinsic self-propulsion as discussed in Ref. [116]. Remarkably, hydrodynamic interactions lead to a shrinkage of flexible active polymers with self-propelled monomers (ABPO+HI) over a range of Péclet numbers. This is in contrast to externally driven active polymers, where flexible polymers always swell. Moreover, the externally driven active polymers assume a larger asymptotic mean square end-to-end distance for  $Pe \rightarrow \infty$  than an ABPO+HI, i.e., intrinsically active Brownian polymers in presence of hydrodynamic interactions are always more compact.

## 4.2.2 Dynamical properties

The dynamics of the polymers can be calculated from the monomer mean square displacement (MSD) averaged over all monomers  $\langle \overline{\Delta \mathbf{r}^2}(t) \rangle = \sum_i \langle (\mathbf{r}_i(t) - \mathbf{r}_i(0))^2 \rangle / N_m$ . From figure 4.5 we have the MSDs of a polymer with  $N_m = 150$  monomers for various Péclet numbers.

The passive polymer ( $Pe = 0$ ) exhibits a time dependence  $\langle \overline{\Delta \mathbf{r}^2} \rangle \sim t^{0.6}$ , very close to the well-known Zimm behavior, with the time dependence  $t^{2/3}$  of the MSD in the

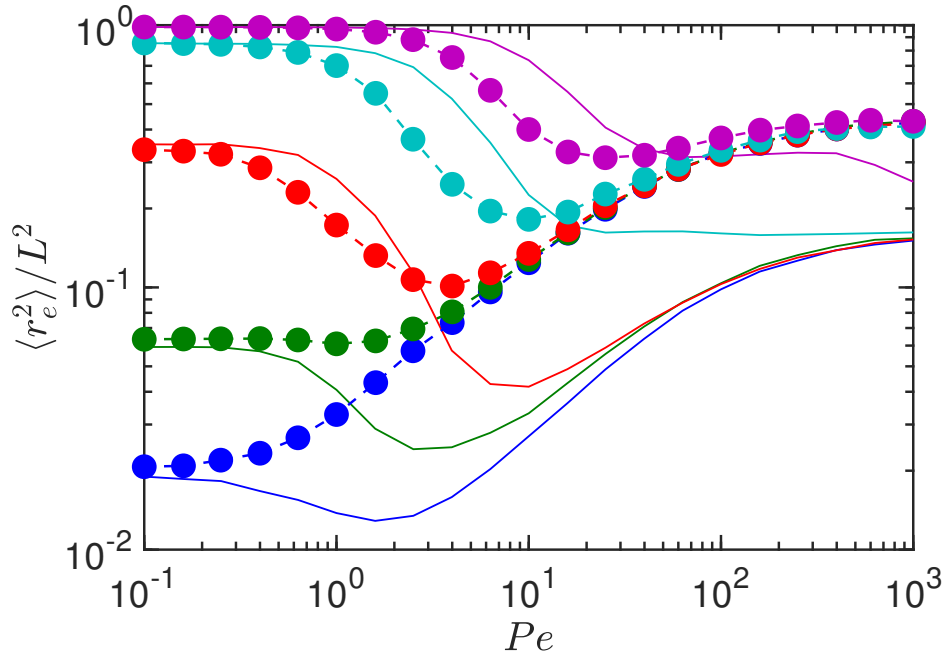


Fig. 4.4 Polymer mean square end-to-end distance as a function of the Péclet number of semiflexible polymers of length  $N_m = 50$  ( $L = 49l$ ) and  $pL = 5 \times 10^1$  (blue),  $1.5 \times 10^1$  (green), 2.6 (red),  $2.5 \times 10^{-1}$  (cyan), and  $2.5 \times 10^{-2}$  (purple). Bullets indicate results for the external active process and lines the respective results for self-propelled monomers (ABPO+HI [116]).

center-of-mass reference frame for  $t/\tau_Z \ll 1$ . At long times  $t/\tilde{\tau}_1 \gg 1$ , the center-of-mass displacement dominates the monomer MSD for all Péclet number. In contrast with the HI-independent MSD of the active Brownian polymers from Eq. (3.41), we get a HI-dependent MSD  $\langle \mathbf{r}_{cm}^2 \rangle = 2v_0^2 l H_{00} t / \gamma_R L$  following from Eq. (4.46). Here, the active ballistic regime,  $\langle \Delta \mathbf{r}^2 \rangle \sim t^2$ , appears at short times ( $\gamma_R t, t/\tilde{\tau}_1 < 1$ ) and becomes more relevant with increasing Péclet.

### 4.3 Analytical approach

Insight into the qualitative differences between an externally driven active polymer and a polymer composed of self-propelled monomers is achieved by an analytical model, where the polymer is described as a continuous Gaussian semiflexible chain. This model has previously been applied to linear and ring active Brownian free-draining polymers, ABPO-HI, [74, 76, 77, 117, 121], as well as to linear self-propelled polymers with hydrodynamic interactions, ABPO+HI, [116].

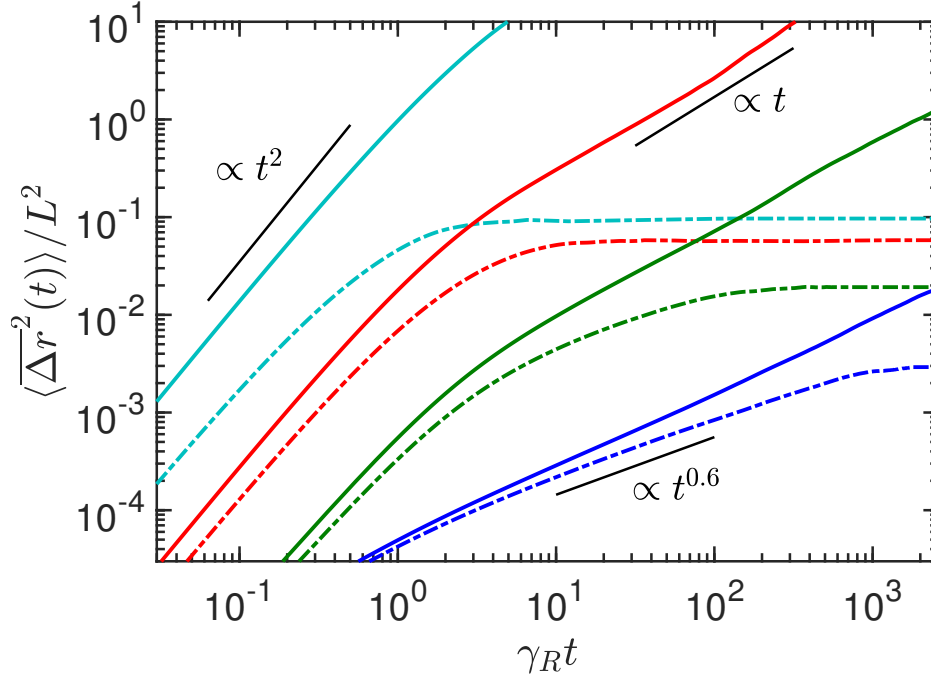


Fig. 4.5 Mean square displacement of a flexible phantom polymer with  $Nm = 150$  ( $pL = 150$ ) monomers for the Péclet numbers  $Pe = 0$  (blue), 10 (green),  $10^2$  (red), and  $10^3$  (cyan). The time is scaled by the factor  $\gamma_R = 2D_R$ . The solid lines indicate the monomer MSD and the dashed lines the MSD in the polymer center-of-mass reference frame. The black lines are guides for the eye correspond to a power-law fit of the data in the respective regime.

### 4.3.1 Model and equations of motion

The polymer is considered as a differentiable space curve  $\mathbf{r}(s, t)$  of total length  $L$ , with contour coordinate  $s$  ( $-L/2 \leq s \leq L/2$ ), and its conformations change with time  $t$ . The external active process is introduced by assigning an independent velocity  $\mathbf{v}(s, t)$  to every point  $\mathbf{r}(s, t)$ . The corresponding Langevin equation is [120, 131]

$$\frac{\partial \mathbf{r}(s, t)}{\partial t} = \int_{-L/2}^{L/2} ds' \mathbf{H}(\mathbf{r}(s), \mathbf{r}(s')) \left[ 3\pi\eta \mathbf{v}(s', t) + 2\nu k_B T \frac{\partial^2 \mathbf{r}(s', t)}{\partial s'^2} - \epsilon k_B T \frac{\partial^4 \mathbf{r}(s', t)}{\partial s'^4} + \mathbf{\Gamma}(s', t) \right]. \quad (4.13)$$

Free end boundary conditions are applied as described in Refs. [74, 76, 88]. Moreover, the constraint on the contour length

$$\int_{-L/2}^{L/2} ds \left\langle \left( \frac{\partial \mathbf{r}(s, t)}{\partial s} \right)^2 \right\rangle = L \quad (4.14)$$

is taken into account, which is elementary to achieve the correct polymer properties [74, 76, 88, 121]. The tensor  $\mathbf{H}(\mathbf{r}(s), \mathbf{r}(s')) = \boldsymbol{\Omega}(\mathbf{r}(s) - \mathbf{r}(s')) + \mathbf{I}\delta(s - s')/3\pi\eta$  captures the hydrodynamic interactions, where the term with the  $\delta$  function describes the local friction, and

$$\boldsymbol{\Omega}(\Delta \mathbf{r}) = \frac{1}{8\pi\eta|\Delta \mathbf{r}|} \left( \mathbf{I} + \frac{\Delta \mathbf{r} \otimes \Delta \mathbf{r}}{|\Delta \mathbf{r}|^2} \right) \quad (4.15)$$

is the Oseen tensor [116, 132, 155]. The terms in Eq. (4.13) with the second and fourth derivative capture chain flexibility, i.e., chain entropy, and bending forces, respectively. The Lagrangian multiplier  $\nu$  accounts for the inextensibility of the polymer (we will denote  $\nu$  as stretching coefficient in the following) and  $\epsilon$  characterizes the bending stiffness [87, 90]. For a polymer in three dimensions, previous studies yield  $\epsilon = 3/4p$ , where  $p = 1/2l_p$  and  $l_p$  is the persistence length [87, 90].

For the velocity  $\mathbf{v}(s, t)$ , we adopt a non-Markovian Gaussian stochastic process with zero mean and the correlation function (colored noise)

$$\langle \mathbf{v}(s, t) \cdot \mathbf{v}(s', t') \rangle = v_0^2 l e^{-\gamma_R |t-t'|} \delta(s - s') . \quad (4.16)$$

This correlation function follows from Eq. (1.76) or, similarly, by considering a monomer as an active Ornstein-Uhlenbeck particle (AOUP) [1, 73, 74, 86, 125].

As outlined in Sec. 4.1.1,  $\mathbf{v}(s, t)$  is a consequence of an external force, hence,  $\mathbf{v}(s, t)$  appears under the integral in Eq. (4.13) and implies a Stokeslet flow. Possibly higher order multipole flow fields, such as force-dipole and source-dipole contributions are neglected since they decay as  $\mathcal{O}(r^{-2})$  with distance compared to a  $1/r$  decay of the Stokeslet flow field [79].

### 4.3.2 Solution of the equations of motion

#### Hydrodynamic tensor: Preaveraging approximation

In order to find an, at least, approximate analytical solution of the nonlinear and nonlocal equation of motion (4.13), we apply the preaveraging approximation proposed by Zimm [132, 156], where the hydrodynamic tensor  $\mathbf{H}(\mathbf{r}(s) - \mathbf{r}(s'))$  is replaced by its stationary-state average, i.e.,  $\mathbf{H}(\mathbf{r}(s) - \mathbf{r}(s')) \rightarrow \langle \mathbf{H}(\mathbf{r}(s) - \mathbf{r}(s')) \rangle = \mathbf{H}(s, s')$ . Hence, Eq. (4.13) turns into a linear equation (Ornstein-Uhlenbeck process) with a Gaussian

stationary-state distribution function for the distance  $\Delta\mathbf{r}(s, s') = \mathbf{r}(s) - \mathbf{r}(s')$  of the form [95, 116, 120, 125, 132]

$$\Psi(\Delta\mathbf{r}) = \left(\frac{3}{2\pi a^2(s, s')}\right)^{3/2} \exp\left(-\frac{3\Delta\mathbf{r}^2}{2a^2(s, s')}\right), \quad (4.17)$$

with  $a^2(s, s') = \langle(\mathbf{r}(s) - \mathbf{r}(s'))^2\rangle$ . Then, the hydrodynamic tensor becomes

$$\mathbf{H}(s, s') = \left[\frac{\delta(s - s')}{3\pi\eta} + \Omega(s, s')\right] \mathbf{I} = H(s, s')\mathbf{I}, \quad (4.18)$$

with the preaveraged Oseen tensor

$$\Omega(s, s') = \frac{\Theta(|s - s'| - d_H)}{3\pi\eta} \sqrt{\frac{3}{2\pi a^2}} \mathbf{I} = \Omega(s, s')\mathbf{I}. \quad (4.19)$$

The Heaviside step function  $\Theta(x)$  introduces  $d_H$  as a lower cut-off for the hydrodynamic interactions, which can be identified with the thickness of the polymer.

The preaveraging approximation has very successfully been applied to describe the dynamics of DNA [131] and semiflexible polymers [116, 120]. Even quantitative agreement between analytical theory and simulations of the full hydrodynamic contribution of rather stiff polymers is achieved [157], as well as with measurements on DNA [131, 158]. This demonstrates the suitability of preaveraging even for stretched polymers. However, the preaveraging approximation overestimates the hydrodynamics of rodlike objects [91].

### Eigenfunction expansion

The linearized equation of motion is solved by the eigenfunction expansion

$$\mathbf{r}(s, t) = \sum_{n=0}^{\infty} \boldsymbol{\chi}_n(t) \varphi_n(s), \quad (4.20)$$

in terms of the eigenfunctions  $\varphi_n$  of the equation

$$\epsilon k_B T \frac{d^4}{ds^4} \varphi_n(s) - 2\nu k_B T \frac{d^2}{ds^2} \varphi_n(s) = \xi_n \varphi_n(s), \quad (4.21)$$

with the eigenvalues ( $n \in \mathbb{N}_0$ )

$$\xi_n = k_B T (\epsilon \zeta_n^4 + 2\nu \zeta_n^2). \quad (4.22)$$

The wave numbers  $\zeta_n$  follow from the boundary conditions. For a passive flexible polymer,  $pL \gg 1$ , the wave numbers are  $\zeta_n = n\pi/L$  and the eigenvalues  $\xi_n = 2\nu k_B T \pi^2 n^2 / L^2$ . The stiffness dependence of  $\zeta_n$  and  $\xi_n$  of passive semiflexible polymers is discussed in Ref. [88] and for free draining active polymers in Ref. [76].

Insertion of the expansion (4.20) into the Eq. (4.13) yields the equation

$$\frac{d\boldsymbol{\chi}_m(t)}{dt} = \sum_{n=0}^{\infty} H_{mn} [\gamma \mathbf{v}_m(t) + \boldsymbol{\Gamma}_n(t) - \xi_n \boldsymbol{\chi}_n(t)] \quad (4.23)$$

for the mode amplitudes  $\boldsymbol{\chi}_n$ , where  $H_{nm} = (\delta_{nm} + 3\pi\eta\Omega_{nm})/3\pi\eta$  is the hydrodynamic tensor in mode representation [120]. The second moments of the stochastic-force amplitudes  $\boldsymbol{\Gamma}_n(t)$  are given by

$$\langle \Gamma_{n\alpha}(t) \Gamma_{m\beta}(t') \rangle = 2k_B T \delta_{\alpha\beta} \delta(t-t') H_{nm}^{-1}. \quad (4.24)$$

The mode representation of the correlation function (4.16) of the active velocity is [74]

$$\langle \mathbf{v}_n(t) \cdot \mathbf{v}_m(t') \rangle = v_0^2 l e^{-\gamma_R |t-t'|} \delta_{nm}. \quad (4.25)$$

In Eq. (4.23), all modes couple in general and the set of equations can only be solved numerically. To arrive at an analytical solution, we neglect the off-diagonal terms of the hydrodynamic mode tensor  $H_{nm}$ , which yields [120, 131, 132] ( $n > 0$ )

$$\frac{d\boldsymbol{\chi}_n(t)}{dt} = -\frac{1}{\tilde{\tau}_n} \boldsymbol{\chi}_n + H_{nn} [\boldsymbol{\Gamma}_n(t) + \gamma \mathbf{v}_n(t)], \quad (4.26)$$

with the relaxation times

$$\tilde{\tau}_n = \frac{1}{H_{nn}\xi_n} = \frac{\tau_n}{1 + 3\pi\eta\Omega_{nn}} \quad (4.27)$$

and  $\tau_n = 3\pi\eta/\xi_n$  the relaxation times in absence of hydrodynamic interactions. For passive flexible polymers [76, 88]

$$\tau_n = \frac{3\eta L^2}{2\nu k_B T \pi n^2}. \quad (4.28)$$

The stationary-state solution of Eq. (4.26) is ( $n > 0$ )

$$\boldsymbol{\chi}_n(t) = H_{nn} \int_{-\infty}^t dt' e^{-(t-t')/\tilde{\tau}_n} [\gamma \mathbf{v}_n(t') + \boldsymbol{\Gamma}_n(t')], \quad (4.29)$$

and for  $n = 0$

$$\boldsymbol{\chi}_0(t) = \boldsymbol{\chi}_0(0) + \int_0^t dt' H_{00} [\gamma \mathbf{v}_{(0)}(t') + \boldsymbol{\Gamma}_0(t')]. \quad (4.30)$$

### Correlation functions

The correlation functions of the mode amplitudes are given by ( $n > 0$ )

$$\begin{aligned} \langle \boldsymbol{\chi}_n(t) \cdot \boldsymbol{\chi}_m(t') \rangle &= \delta_{nm} \left( \frac{k_B T \tau_n}{\pi \eta} e^{-|t-t'|/\tilde{\tau}_n} \right. \\ &\quad \left. + \frac{v_0^2 l \tau_n^2}{1 - (\gamma_R \tilde{\tau}_n)^2} \left[ e^{-\gamma_R |t-t'|} - \gamma_R \tilde{\tau}_n e^{-|t-t'|/\tilde{\tau}_n} \right] \right), \end{aligned} \quad (4.31)$$

and for  $n = 0$

$$\begin{aligned} \langle \boldsymbol{\chi}_0(t) \cdot \boldsymbol{\chi}_0(t') \rangle &= \langle \boldsymbol{\chi}_0^2(0) \rangle + 6k_B T H_{00} t' \\ &\quad + \gamma H_{00} \frac{v_0^2 l}{\gamma_R^2} \left[ 2\gamma_R t' - 1 - e^{\gamma_R(t'-t)} + e^{-\gamma_R t} + e^{-\gamma_R t'} \right]. \end{aligned} \quad (4.32)$$

Inserting the eigenfunction expansion (4.20) into the mean square distance  $a^2(s, s')$ , we obtain

$$a^2(s, s') = \sum_{n=1}^{\infty} \langle \boldsymbol{\chi}_n^2 \rangle (\varphi_n(s) - \varphi_n(s'))^2, \quad (4.33)$$

with the stationary-state correlation functions (4.31)

$$\langle \boldsymbol{\chi}_n^2 \rangle = \frac{k_B T \tau_n}{\pi \eta} + \frac{v_0^2 l \tau_n^2}{1 + \gamma_R \tilde{\tau}_n}, \quad (4.34)$$

which depend on the hydrodynamic interactions via  $\tilde{\tau}_n$ . The active term with  $v_0^2$  leads to enhanced fluctuations, which are more significant at small mode numbers [121], and reflects the violation of the fluctuation-dissipation relation [159]. Notably, hydrodynamic interactions affect the dynamics as well as the stationary-state conformational properties of an active polymer, in contrast to passive systems, where conformational properties are independent of hydrodynamic interactions.

### Mean square distance and hydrodynamic tensor: Mode representation

The exact analytical expression of the mean square distance  $a^2$  (4.33) for the flexible active polymer can be calculated by (numerically) performing the sum in Eq. (4.33). For a semiflexible polymer in a passive system,  $a^2(s, s')$  is only a function of the

difference  $|s - s'|$  [89, 120]. A priori,  $a^2(s, s')$  of an active polymer depends on  $s$  and  $s'$  individually. As a first approximation, we replace the difference of the eigenfunctions in Eq. (4.33) by the expression valid for a passive polymer which only depends on  $|s - s'|$ , and  $\varphi_n(s) - \varphi_n(s') = 2 \sin(n\pi(s - s')/2L)$  for  $n$  odd, and  $\varphi_n(s) - \varphi_n(s') = 0$  for  $n$  even.

As a result, we obtain the expression

$$a^2(s) = \frac{8}{L} \sum_{n, \text{odd}} \left( \frac{k_B T \tau_n}{\pi \eta} + \frac{v_0^2 l \tau_n^2}{1 + \gamma_R \tilde{\tau}_n} \right) \sin^2 \left( \frac{n\pi}{2L} s \right). \quad (4.35)$$

In order to determine the relaxation times  $\tilde{\tau}_n$ , which depend via  $a^2(s, s')$  on the Oseen tensor, the double integral

$$\Omega_{nn} = \sqrt{\frac{1}{6\pi^3 \eta^2}} \int_{-L/2}^{L/2} \int_{-L/2}^{L/2} \Theta(|s - s'| - d_H) \frac{\varphi_n(s) \varphi_n(s')}{\sqrt{a^2(s, s')}} ds' ds \quad (4.36)$$

has to be calculated. As a consequence, Eq. (4.33) and (4.36) have to be evaluated in an iterative and self-consistent manner, where the double integration, combined with the summation of Eq. (4.33), constitutes a major computational challenge. A more easily tractable expression with a single integral follows by apply a standard approximation for the integrals over the functions  $\varphi_n$  in Eq. (4.36) as, e.g., described in Ref. [132] for a flexible polymer, which yields

$$\Omega_{nn} = \sqrt{\frac{2}{3\pi^3 \eta L}} \int_{d_H}^L \frac{L - s}{\sqrt{a^2(s)}} \cos \left( \frac{n\pi}{L} s \right) ds. \quad (4.37)$$

This expression is identical with that of a passive polymer aside from the distance  $a^2(s - s')$ , which depends here on activity via the relaxation times [120]. As shown in Fig. 4.6, the approximations resulting in Eq. (4.35) capture the dependence of  $a^2(s, s')$  on the contour coordinate well, the better the larger the Péclet number. Assuming a linear dependence of  $a^2(s - s')$  on  $|s - s'|$ , i.e.,  $a^2(s) = a_0^2 |s| L$ , as for a passive flexible polymer [120], we obtain the analytical solution of Eq. (4.37)

$$\Omega_{nn} = \frac{1}{\sqrt{3\pi^3 \eta a_0}} \frac{1}{\sqrt{n}}, \quad (4.38)$$

in analogy to the Zimm approach [120, 132, 156]. Choosing for  $a_0^2$  the result of a flexible ABPO-III, namely  $a_0^2 = 1/\mu p L + P e^2 / 6 \mu p L \Delta$ , where the Péclet number  $Pe$  and  $\Delta$  are defined in Eq. (4.5), and  $\mu$  is given by  $\mu = 2\nu/(3p)$  [74], we obtain for

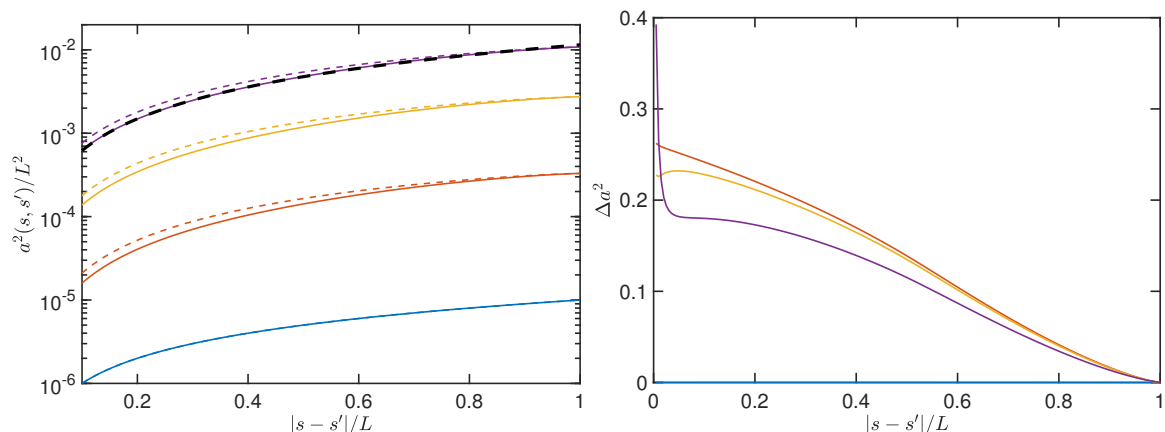


Fig. 4.6 (a) Mean square distance between two points along the polymer contour as a function of their distance for  $pL = 10^3$  and the Péclet numbers  $Pe = 10^{-2}$  (blue),  $Pe = 1$  (orange),  $Pe = 50$  (yellow) and  $Pe = 10^3$  (purple). The solid lines are obtained from Eq. (4.33), where  $s' = -L/2$ , and the dashed lines from the approximation (4.35). The long-dashed line is a power-law fit, which yields  $a^2(s) = 0.11s^{1.27}$ . (b) Ratio  $\Delta a^2 = |a^2(s, s') - a^2(s - s')|/a^2(s, s')$  [Eqs. (4.33), (4.35)]. The colors correspond to the same Péclet numbers as in (a).

$Pe \gg 1$

$$\Omega_{mn} \sim \frac{\sqrt{pL\mu}}{Pe\sqrt{n}}. \quad (4.39)$$

In the following, when not indicated otherwise, the approximate expressions (4.35) and (4.37) are used for the calculation of the Oseen tensor. Moreover, we use  $\Delta = 1/3$ , the value of a spherical colloid of diameter  $l$  in solution.

### Stretching coefficient and relaxation times

Considering flexible polymers,  $pL \gg 1$ , setting  $L/l = pL$ , and inserting the eigenfunction expansion (4.20), the constraint (4.14) for the stretching coefficient  $\mu = 2\nu/3p$  turns into

$$\sum_{n=1}^{\infty} \left[ \frac{k_B T \tau_n}{\pi \eta} + \frac{v_0^2 l \tau_n^2}{1 + \gamma_R \tilde{\tau}_n} \right] \zeta_n^2 = L, \quad (4.40)$$

with the relaxation times (Eq. (4.27))

$$\tilde{\tau}_n = \frac{\tau_R}{\mu n^2 (1 + 3\pi \eta \Omega_{nn})}, \quad (4.41)$$

where  $\tau_R = \eta L^2 / (\pi k_B T p)$  is the Rouse relaxation time [88, 132]. Due to nonlinear terms, specifically in  $\Omega_{nn}$ , we solve the required equations and expressions numerically.

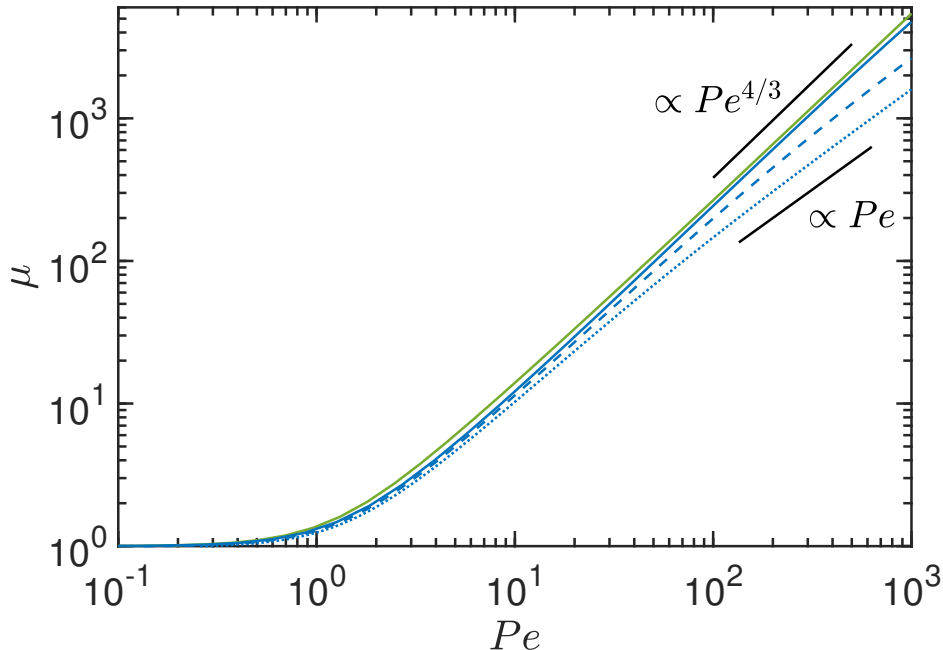


Fig. 4.7 Normalized stretching coefficient  $\mu = 2\nu/(3p)$ , solution of Eq. (4.40), as function of the Péclet number  $Pe$  for flexible polymers with  $pL = 50$  (dotted),  $1.5 \times 10^2$  (dashed), and  $10^3$  (solid) in blue color. The green line shows the result of an active polymer in absence of HI for  $pL = 10^3$  (solid). The black lines denote the power laws in the respective regimes.

The scaled stretching coefficient,  $\mu = 2\nu/(3p)$ , is presented in Fig. 4.7 as a function of the Péclet number. For short polymers or larger stiffness ( $pL = 50$ ),  $\mu$  increases linearly with increasing  $Pe$  in the limit  $1 \ll pL \ll Pe$  (cf. Eq. (D.2)). In case of more flexible polymers ( $pL \gtrsim 10^3$ ),  $\mu \sim Pe^{4/3}$  in the range  $1 \ll Pe \ll pL$  (cf. Eq. (D.3)). The overall dependence of  $\mu$  on  $Pe$  resembles that of a polymer in the absence of hydrodynamic interactions in this limit [74]. Yet, hydrodynamics affects  $\mu$  particularly for Péclet numbers in the vicinity of  $Pe \approx 10$ . In Appendix D, a more detailed discussion of the asymptotic dependencies are provided.

Figure 4.8 depicts the dependence of the preaveraged Oseen tensor on the mode number for flexible polymers. For a passive polymer, we obtained the dependence  $\Omega_{nn} \sim n^{-1/2}$  of the Zimm model[132] over a range of mode numbers, which depends on  $pL$ . With increasing Péclet number, both the values of  $\Omega_{nn}$  and the magnitude of the slope decrease substantially. As a consequence, at high Péclet numbers,  $\Omega_{nn}$  does not contribute to the mode-number dependence of the relaxation time anymore, as is reflected in Fig. 4.8. Again, we obtain the Zimm behavior with  $\tilde{\tau}_n \sim n^{-3/2}$  for

the passive polymer. With increasing Péclet number, the slope changes to  $\tilde{\tau}_n \sim n^{-7/4}$  for  $Pe = 10^3$ , a dependence very close to that of a free-draining, non-hydrodynamic Rouse polymer. This emphasizes the diminishing effect of hydrodynamic interactions with increasing activity.

The activity-dependence of the longest polymer relaxation time is displayed in Fig 4.9(b). The drop of  $\tilde{\tau}_1$  with increasing  $Pe$  is determined by the stretching coefficient  $\mu$  and the implicit dependence of  $\Omega_{11}$  on  $\mu(Pe)$ . The shift to larger  $Pe$  of the curves in presence of HI compared to that in its absence reflects the influence of HI on the relaxation times, specifically the influence of  $\Omega_{11}$ . The latter is also responsible for values  $\tilde{\tau}_1/\tilde{\tau}_1^0 > 1$  ( $Pe \approx 1$ ), because  $\Omega_{11}$  decreases with increasing  $Pe$  (Fig. 4.8). As discussed in App. D,  $\mu$  is essentially independent of hydrodynamic interactions for  $pL \ll Pe$ , hence, the drop of  $\tilde{\tau}_1$  for  $pL = 50$  ( $Pe \gg 1$ ) is solely determined by  $\mu$  and  $\tilde{\tau}_1 \sim 1/Pe$ . Similar, the asymptotic behavior for  $pL = 10^3$  is determined by the  $\mu$ , with  $\tilde{\tau}_1 \sim 1/Pe^{4/3}$ , the dependence of a polymer in absence of hydrodynamic interactions. However, for very flexible polymers,  $pL \gtrsim 10^3$ , HI gives rise to an intermediate regime,  $10 < Pe < 10^3$ , where  $\tilde{\tau}_1 \sim Pe^{-7/6}$ . The difference to a decay with  $Pe^{-1}$  seems subtle, but is essential, as will be discussed in Sec. 4.3.3

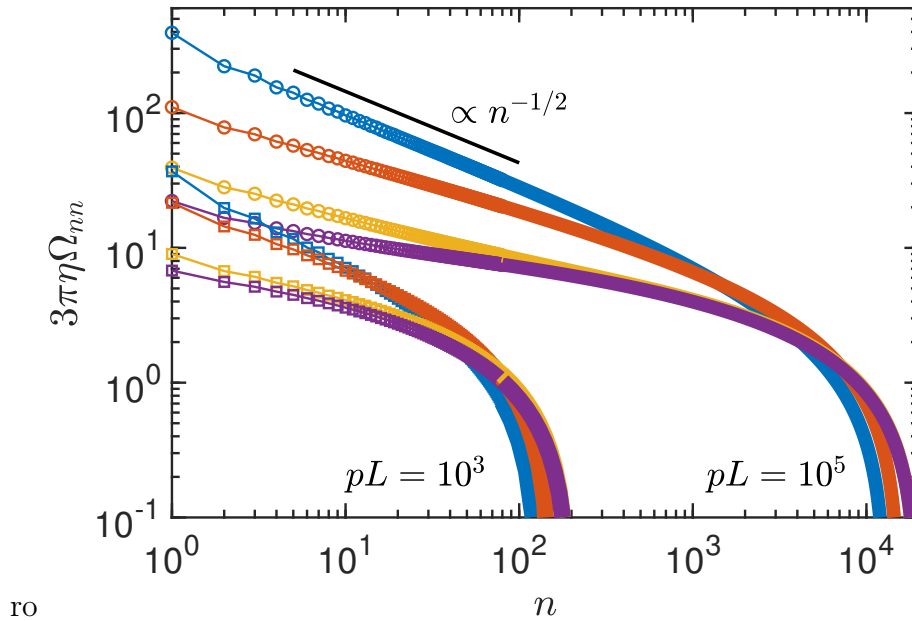


Fig. 4.8 (a) Mode-number dependence of the Oseen tensor  $\Omega_{nn}$  for polymers of length  $pL = 10^3$  (squares) and  $pL = 10^5$  (circles) and the Péclet numbers  $Pe = 10^{-2}$  (blue),  $Pe = 1$  (orange),  $Pe = 50$  (yellow), and  $Pe = 10^3$  (purple). The black line indicates the power law  $\Omega_{nn} \propto n^{-1/2}$  in the respective regime.

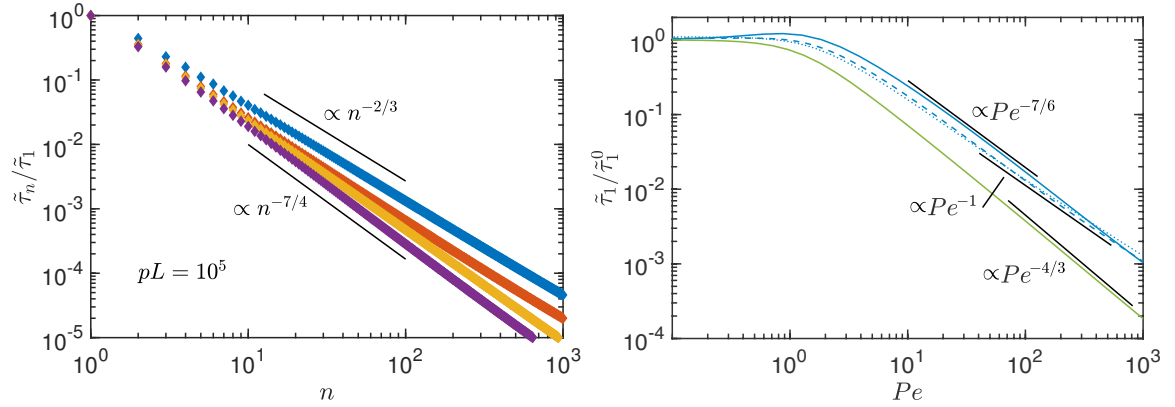


Fig. 4.9 (a) Mode-number dependence of the relaxation times  $\tilde{\tau}_n$  for flexible polymers of length  $pL = 10^5$  and the Péclet numbers  $Pe = 0$  (blue),  $Pe = 1$  (orange),  $Pe = 50$  (yellow), and  $Pe = 10^3$  (purple). The black line indicates the power law in the respective regime. (b) Longest polymer relaxation time  $\tilde{\tau}_1$ , Eq. (4.41), normalized by the corresponding passive value  $\tilde{\tau}_1^0$  as function of the Péclet number  $Pe$  for flexible polymers with  $pL = 50$  (dotted),  $1.5 \times 10^2$  (dashed), and  $10^3$  (solid) in blue color. The green solid curve corresponds to an active polymer in absence of HI for  $pL = 10^3$ , where  $\tau_1 \sim Pe^{-4/3}$ .

### 4.3.3 Conformational properties

The conformational properties of a polymer are characterized by its mean square end-to-end distance  $\langle \mathbf{r}_e^2 \rangle = \langle (\mathbf{r}(L/2) - \mathbf{r}(-L/2))^2 \rangle$ , which is

$$\langle \mathbf{r}_e^2 \rangle = \frac{8}{L} \sum_{n, \text{odd}} \left( \frac{k_B T \tau_n}{\pi \eta} + \frac{v_0^2 l \tau_n^2}{1 + \gamma_R \tilde{\tau}_n} \right) \quad (4.42)$$

in terms of the mode amplitudes of Eq. (4.34). Numerical results for  $\langle \mathbf{r}_e^2 \rangle$  are displayed in Fig. 4.10. As in simulations (cf. Fig. 4.2), polymers swell with increasing activity and saturate for  $Pe \rightarrow \infty$ . The swelling behavior is distinctly different from that of free draining polymers or polymers with self-propelled monomers by the dependence on the relaxation times  $\tilde{\tau}_n$ . Comparing the active terms (with  $v_0$ ) for a free-draining polymer [74], a polymer with self-propelled monomers [116], and Eq. (4.42), we find

$$\frac{\tau_n^2}{1 + \gamma_R \tilde{\tau}_n} \geq \frac{\tau_n^2}{1 + \gamma_R \tau_n} \geq \frac{\tilde{\tau}_n^2}{1 + \gamma_R \tilde{\tau}_n}, \quad (4.43)$$

because  $\tilde{\tau}_n \leq \tau_n$ . Hence, the externally driven polymer swells strongest with increasing Péclet number, and swelling sets in at smaller  $Pe$ . This is reflected in the shift of the dashed-dotted lines in Fig. 4.10 to smaller  $Pe$  with increasing  $pL$ , whereas respective curves shift to larger  $Pe$  in case of polymers with self-propelled monomers, associated

with polymer shrinkage [116]. This reflects the distinct influence of the character of the active noise on the polymer conformations in presence of hydrodynamic interactions.

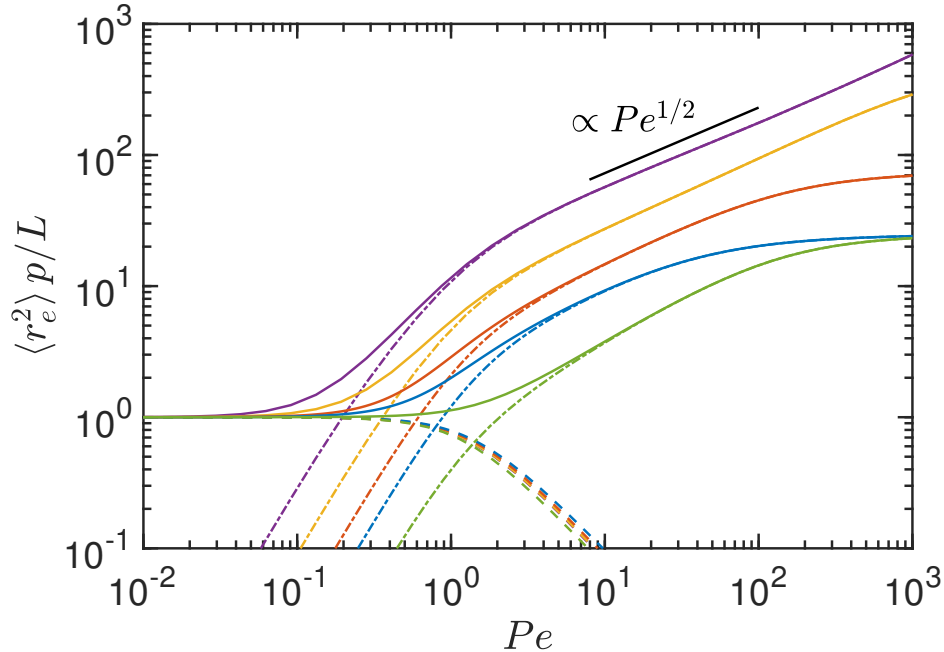


Fig. 4.10 Polymer mean square end-to-end distance  $\langle r_e^2 \rangle$  scaled by the equilibrium value  $L/p$  in the presence of HI as a function of the Péclet number  $Pe$  for flexible polymers of length  $pL = 50$  (blue),  $pL = 1.5 \times 10^2$  (orange),  $pL = 10^3$  (yellow), and  $pL = 10^4$  (purple). The green curve corresponds to the free-draining flexible polymer with  $pL = 50$ . The dashed curves represent the passive contribution with the relaxation times  $\tau_n$  and the dashed-dotted curves the active part with  $v_0^2$  in Eq. (4.42).

The asymptotic limit for  $Pe \rightarrow \infty$  can be obtained analytically. The term  $\gamma_R \tilde{\tau}_n \ll 1$  for  $Pe \rightarrow \infty$  (cf. App. D) and, thus, can be neglected in Eq. (4.42). Evaluation of the sum over modes with the relaxation times (4.28) and insertion of Eq. (D.2) yields then  $\langle r_e^2 \rangle = L^2/2$ . This result is in close agreement with simulations, which yield a somewhat smaller value, as shown in Fig. 4.11. Moreover, the asymptotic limit is identical with that of a free-draining polymer [74], in contrast to a polymer of self-propelled monomers [116].

Simulations (Fig. 4.2) and analytical calculations (Fig. 4.10) predict the swelling behavior  $\langle r_e^2 \rangle \sim Pe^{1/2}$  over a range of Péclet numbers, which increases with increasing  $pL$ . This dependence on  $Pe$  is markedly different from that of free-draining polymers and those with self-propelled monomers, where the exponent is larger than unity. This difference rests upon a particular dependence of the dynamics on hydrodynamic interactions, reflected in the  $Pe$  dependence of the relaxation time  $\tilde{\tau}_1$  (Fig. 4.9)(b).

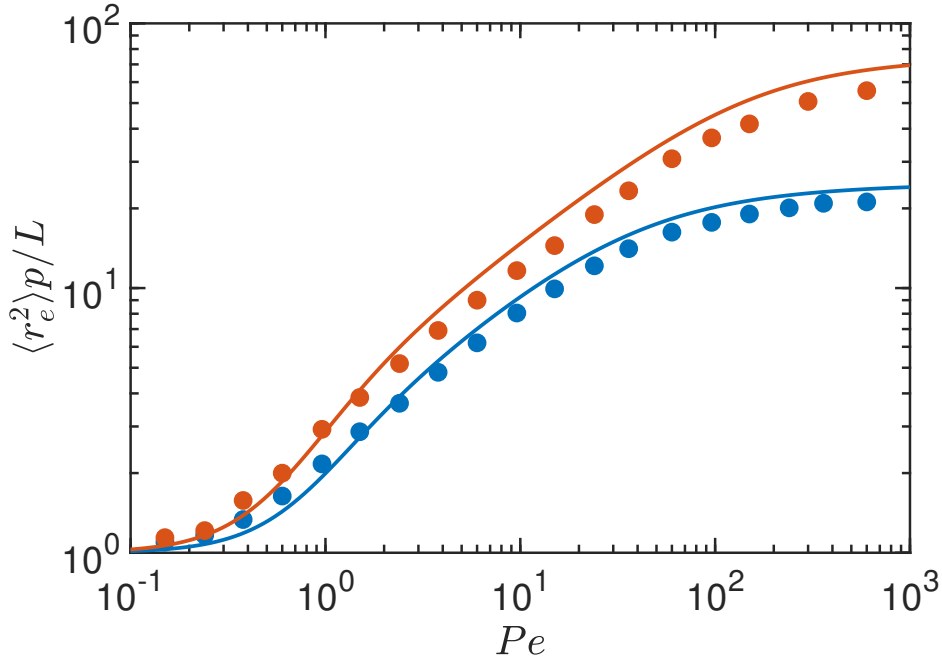


Fig. 4.11 Comparison of the dependence of polymer mean square end-to-end-distance on the Péclet number obtained from analytical theory (lines) and BD simulations (bullets) for polymers with  $pL = 50$  (blue) and  $pL = 1.5 \times 10^2$  (orange).

Analytically, the square-root dependence is obtained as follows. First, the relaxation times  $\tilde{\tau}_n$  are well described by a power law, specifically for  $pL = 10^3$   $\tilde{\tau}_n \approx \tilde{\tau}_1/n^2$  (Fig. 4.9)(a). Secondly, in the relevant  $Pe$  regime,  $\gamma_R \tilde{\tau}_n \gg 1$ , hence, Eq. (4.42) yields

$$\langle r_e^2 \rangle \sim \frac{Pe^2}{\mu^2 \tilde{\tau}_1} \sim \sqrt{Pe}, \quad (4.44)$$

with  $\mu \sim Pe^{4/3}$  (Eq. D.3) and  $\tilde{\tau}_1 \sim Pe^{7/6}$  (Fig. 4.9)(b)), relations appropriate for  $pL = 10^3$ . It is the  $Pe$  dependence of the relaxation time  $\tilde{\tau}_1$  which is decisive for the relation (4.44). In the absence of HI,  $\tau \sim 1/\mu \sim Pe^{-4/3}$  and  $\langle r_e^2 \rangle \sim P^{2/3}$  [74], which is a substantially stronger  $Pe$  dependence. However, the seemingly rather small difference between  $4/3 = 8/6$  and  $7/6$  of the exponent of the relaxation time is decisive and leads to a considerably different swelling behavior of the polymer with increasing  $Pe$ .

The theoretical approach very well reproduces the simulation data, as shown in Fig. 4.11. Merely, the analytical theory overestimates the asymptotic value as a consequence of the mean-field-type constraint for the bond length (Eq. (4.14)).

We like to emphasize that the swelling of active polymers is determined by their inextensibility, as is evident from the results of this section. Only by suitably includ-

ing an inextensibility condition, e.g., Eq. (4.14), the qualitative correct behavior is obtained theoretically [74, 76, 77, 116, 121]. Approaches neglecting such a condition predict swelling, which quantitatively disagrees with simulation results.

## 4.4 Dynamical properties

The polymers dynamics is analyzing in terms of the monomer mean square displacement (MSD) averaged over the polymer contour

$$\begin{aligned}\overline{\langle \Delta \mathbf{r}^2(t) \rangle} &= \frac{1}{L} \int \langle (\mathbf{r}(s, t) - \mathbf{r}(s, 0))^2 \rangle ds \\ &= \langle \Delta \mathbf{r}_{cm}^2(t) \rangle + \langle \Delta \mathbf{r}_0^2(t) \rangle + \langle \Delta \mathbf{r}_a^2(t) \rangle,\end{aligned}\quad (4.45)$$

with the center-of-mass mean square displacement

$$\begin{aligned}\langle \Delta \mathbf{r}_{cm}^2(t) \rangle &= H_{00} \frac{6k_B T}{L} t \\ &\quad + (1 + \Omega_{00}) \frac{2v_0^2 l}{\gamma_R^2 L} (\gamma_R t - 1 + e^{-\gamma_R t}),\end{aligned}\quad (4.46)$$

$H_{00} = (1 + 3\pi\eta\Omega_{00})/(3\pi\eta)$ , the activity-modified equilibrium-like internal-dynamics contribution

$$\langle \Delta \mathbf{r}_0^2(t) \rangle = \frac{1}{L} \sum_{n=1}^{\infty} \frac{2k_B T \tau_n}{\pi\eta} (1 - e^{-t/\tilde{\tau}_n}), \quad (4.47)$$

and the active contribution

$$\langle \Delta \mathbf{r}_a^2(t) \rangle = \frac{1}{L} \sum_{n=1}^{\infty} \frac{2v_0^2 l \tau_n^2}{1 + \gamma_R \tilde{\tau}_n} \left( 1 - \frac{e^{-\gamma_R t} - \gamma_R \tilde{\tau}_n e^{-t/\tilde{\tau}_n}}{1 - \gamma_R \tilde{\tau}_n} \right). \quad (4.48)$$

The passive parts of  $\overline{\langle \Delta \mathbf{r}^2(t) \rangle}$ —in  $\langle \Delta \mathbf{r}_{cm}^2(t) \rangle$  and  $\langle \Delta \mathbf{r}_0^2(t) \rangle$ —, are, aside of the  $\mu$ -dependence of the relaxation times, identical with the dynamics of the Zimm model, or a semiflexible polymer in presence of HI [91, 116, 132, 140].

The center-of-mass MSD exhibits the same time-dependent terms as an active polymer without HI and a polymer with self-propelled monomers. For  $t \rightarrow \infty$ ,  $\langle \Delta \mathbf{r}_{cm}^2(t) \rangle$  dominates the total MSD, increasing linearly with time with the diffusion coefficient

$$D = H_{00} \frac{k_B T}{L} + (1 + \Omega_{00}) \frac{v_0^2 l}{3\gamma_R L}. \quad (4.49)$$

However,  $\Omega_{00}$  depends on polymer length and Péclet number. Figure 4.8 suggests a substantial increase of  $\Omega_{00}$  with polymer length, and a decrease with increasing  $Pe$ , and seems to approach a  $Pe$ -independent value for  $Pe \gg 1$ .

The average MSD of a point  $\mathbf{r}(s, t)$  in the center-of-mass reference frame, Eqs. (4.47), (4.48), exhibits three distinct regimes:

- $t \rightarrow 0$  — The MSD is dominated by Eq. (4.47), and all modes contribute. With  $\tau_n = \tau_R/(\mu n^2)$  for a flexible polymer, and conversion of the sum to an integral yields

$$\langle \overline{\Delta \mathbf{r}_0^2}(t) \rangle = \frac{2L}{\pi^2 p \mu} \left( \frac{t}{\tilde{\tau}_1} \right)^{2/3} \int_0^\infty dx \frac{1 - e^{-x^{3/2}}}{x^2}. \quad (4.50)$$

This is the same relation as obtained for a passive system, except that  $\mu$  and  $\tilde{\tau}_1$  depend on activity, and a polymer with self-propelled monomers [116].

- $t/\tilde{\tau}_1, \gamma_R t \ll 1$  — Taylor expansion of the exponential functions in Eq. (4.48) yields

$$\langle \Delta \mathbf{r}_a^2(t) \rangle = \frac{v_0^2 l \gamma_R}{L} \sum_{n=1}^{\infty} \frac{\tilde{\tau}_n^2}{\tau_n (1 + \gamma_R \tilde{\tau}_n)} t^2, \quad (4.51)$$

consistent with the observed ballistic regime in Fig. 4.12. This regime and its dependence on activity and polymer properties is in quantitative agreement with the simulation results of Fig. 4.5 .

- $t/\tilde{\tau}_1 \ll 1 \ll \gamma_R t$  — With  $\gamma_R \tilde{\tau}_1 \gg 1$ , the MSD is given by

$$\langle \Delta \mathbf{r}_a^2(t) \rangle = \frac{2v_0^2 l}{\gamma_R L} \sum_{n=1}^{\infty} \frac{\tau_n^2}{\tilde{\tau}_n} (1 - e^{-t/\tilde{\tau}_n}). \quad (4.52)$$

The relaxation times  $\tilde{\tau}_n$  are well described by the power-law  $\tilde{\tau}_n = \tilde{\tau}_1/n^\gamma$  (cf. Fig. 4.9). Inserting this relation and replacing the sum by an integral, Eq. (4.52) yields

$$\langle \Delta \mathbf{r}_a^2(t) \rangle = \frac{2v_0^2 l \tau_R^2}{\mu^2 \gamma_R L} \left( \frac{t}{\tilde{\tau}_1} \right)^{3/\gamma-1} \int_0^\infty dx \frac{1 - e^{-x^\gamma}}{x^{4-\gamma}}. \quad (4.53)$$

For  $Pe > 50$ , the power-law exponent is close to  $\gamma = 7/4$ , hence,

$$\langle \Delta \mathbf{r}_a^2(t) \rangle \sim t^{5/7}. \quad (4.54)$$

This time dependence is in close agreement with the numerical result displayed in Fig. 4.12. By the interplay between activity and hydrodynamic interactions, a new power-law regime emerges for the inter-molecular MSD. The seemingly small difference between the exponent  $\gamma = 7/4$  and the value two for a Rouse polymer,

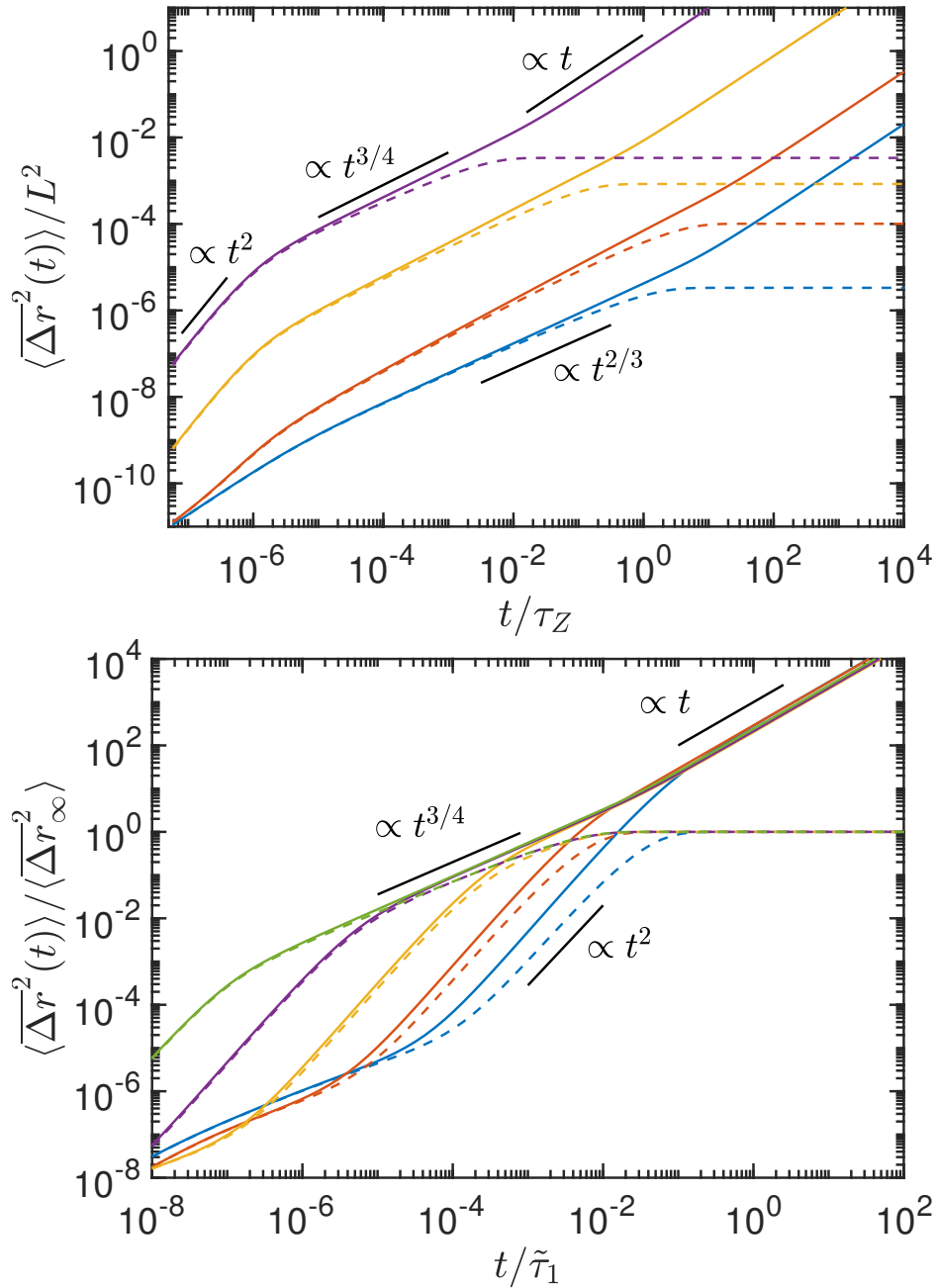


Fig. 4.12 Mean square displacement of flexible polymers for  $pL = 10^5$  and the Péclet numbers  $Pe = 0$  (blue), 1 (orange), 50 (yellow), and  $10^3$  (purple). (b) The Péclet number is  $Pe = 115$  and  $pL = 50$  (blue),  $1.5 \times 10^2$  (orange),  $10^3$  (yellow),  $10^4$  (purple), and  $10^5$  (green). The dashed lines correspond to the MSD in the polymer center-of-mass reference frame, and the solid lines are the overall MSD. The black lines denote the power laws in the respective regimes.

implies a significantly different power-law MSD, namely an exponent  $7/5$  vs.  $1/2$  for Rouse polymer [76]. Moreover, the type of active force matters—calculations for self-propelled monomers yield the exponent  $2/5$  [116], which is even smaller than the value for the free-draining polymers. This emphasizes the strong and determining influence of hydrodynamic interactions on the dynamics of active polymers.

The overall monomer MSD (4.45), exhibits even a different power-law regime  $\overline{\langle \Delta \mathbf{r}^2(t) \rangle} \sim t^{3/4}$  for  $pl \gtrsim 10^3$ , by an additional contribution of the center-of-mass MSD. Evidently, a separation of the MSD in the center-of-mass reference frame from the overall MSD is not possible, even for very long polymers.



# Chapter 5

## Multiparticle collision dynamics approach with self-propelled polymers

### 5.1 Self-propelled monomer in MPC fluid

An essential aspect of a self-propelled monomer is that active forces do not give rise to a Stokeslet or other higher hydrodynamic multipoles. This is captured and reflected by Eq. (3.1). To account for this specificity of an active particle, the MPC algorithm has to be suitably adapted. Specifically, in the collision step no explicit contributions of the active velocity have to be included.

As for the ABP of Sec. 3.1.1, we consider independent equations of motion for the monomer translation, taking intramolecular forces Eqs. (1.87)- (1.88) into account, and the active velocity  $\mathbf{v}^{act} = v_0 \mathbf{e}$ ; the latter is given by Eq. (3.2).

The integration scheme

$$\mathbf{r}_i(t + dt) = \mathbf{r}_i(t) + \frac{dt^2}{2M} \sum_{i=1}^{N_m} \mathbf{F}_i(t) + dt [\mathbf{v}_i(t) + \mathbf{v}_i^{act}(t)], \quad (5.1)$$

$$\mathbf{v}_i(t + dt) = \mathbf{v}_i(t) + \frac{dt}{2M} [\mathbf{F}_i(t) + \mathbf{F}_i(t + dt)], \quad (5.2)$$

$$\mathbf{v}_i^{act}(t + dt) = \mathbf{v}_i^{act}(t) + v_0 [\mathbf{e}_i(t + dt) - \mathbf{e}_i(t)], \quad (5.3)$$

for the streaming of the monomers are consistent with the dynamics of the self-propelled ABP-type monomers of Sec. 3.1.1. The discretization of the equations of motion (5.1)- (5.3) follows from the Strömer-Verlet algorithm, extensively used for second order differential equation [170]. Equation (5.2) accounts for the velocity contribution of the passive intramolecular forces, Eq. (5.1) for the positions and Eq. (5.3) for the independent change of the active velocity. These equations assume a particular propulsion mechanism.

## 5.2 Fluid-polymer coupling

The streaming of the MPC particles is given by Eq.(1.63). The coupling between the active monomers and the MPC fluid occurs in the collision step as described in Sec. 1.3.2. Here, both the MPC particles as well as the monomers perform a collision. Importantly, the active velocity contribution of the active force has to be taken into account. Thus, the total velocities after streaming (Eq. (5.3) ) are used in the rotation process and the calculation of collision-cell center-of-mass velocity, which is then given by

$$\mathbf{v}_i(t+h) = \mathbf{v}_i^{act}(t+h) + \bar{\mathbf{v}}_{cm}(t+h) + \mathbf{R}(\alpha) [\mathbf{v}_i(t+h) - \bar{\mathbf{v}}_{cm}(t+h)]. \quad (5.4)$$

By considering solely the passive monomer velocity,  $\mathbf{v}_i(t)$ , in the rotation step, we assume the activity of a monomer as an internal source of energy, which must be (explicitly) independent from the fluid. In other words, we avoid the appearance of any Stokeslet of active nature into the system.

The center-of-mass velocity of the  $N_c + N_m^c$  particles, including fluid particles and monomers, within the cell of particle  $i$  is

$$\bar{\mathbf{v}}_{cm} = \frac{\sum_{j=1}^{n_c} m \hat{\mathbf{v}}_j + \sum_{j=1}^{N_m^c} M \mathbf{v}_j}{m N_c + M N_m^c}, \quad (5.5)$$

and  $\mathbf{R}(\alpha)$  is the rotation matrix. Temperature is not conserved for systems far from equilib-

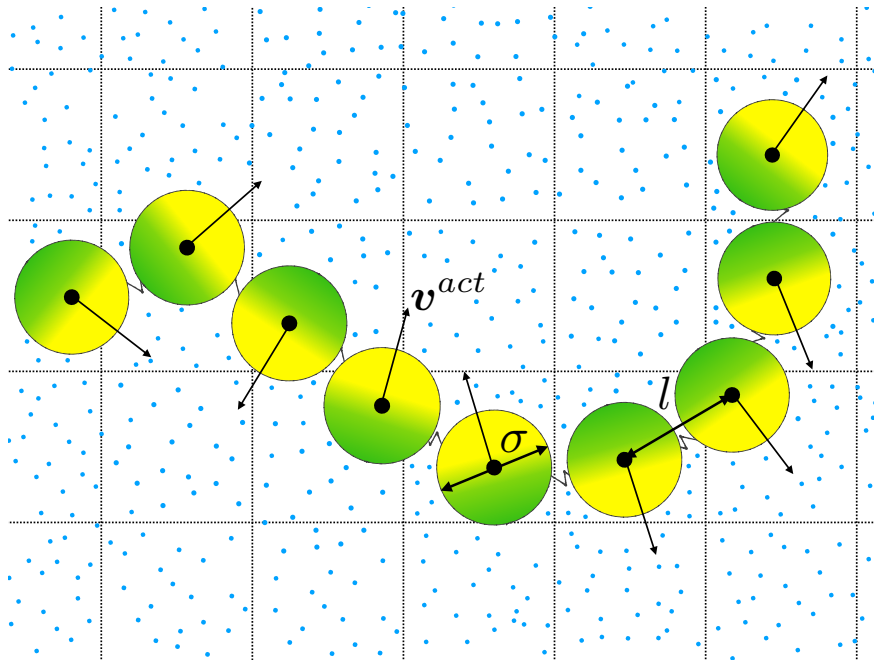


Fig. 5.1 Illustration of an active polymer made out of monomers (yellow-green) surrounded by MPC fluid particles (blue dots). Both monomers and fluid particles inside a collision cell of size  $a$  are involved in the same rotation algorithm.

rium, hence, a thermostat is imposed after each step over the fluid particles and monomers velocities. We apply the Maxwell-Boltzmann scaling method, which picks randomly a new kinetic energy from the gamma distribution in order to rescale the particles velocities after every collision step [114]. This ensures the local momentum conservation and yields a Maxwellian velocity distribution.

We set the energy in units of  $k_B T = 1$ , length in units of the collision cell  $a = 1$ , and time in units of  $\tau = \sqrt{ma^2/k_B T}$ . The mass is measured in units of the fluid particle mass  $m = 1$ . To avoid high monomer velocities, we set a relatively high average number of particles per collision cell of  $\langle N_c \rangle = \rho = 50$ . Accordingly, a single monomer has a mass of  $M = 50$ . Considering a time-step  $h = 0.01\sqrt{ma^2/k_B T}$  gives a viscosity of  $\eta = 447.4$ , according to the theoretical formula [107, 111, 144]. A cubic periodic box of linear size  $L = 32a$  is considered.

Again, we keep the coefficient  $\kappa_l$  (Eq. (1.86)) as  $\kappa_l l^2/k_B T = (10 + 2Pe) \times 10^3$ , to ensure bond-length variations smaller than 3% of the equilibrium value  $l$ . The scaled bending force coefficient  $\tilde{\kappa}_b = \kappa_b l^2/k_B T$  (Eq. (1.87)) is related to the polymer persistence length,  $l_p = 1/(2p)$ , by Eq. (1.90). Finally, we keep  $\sigma = 0.8l$  and  $\epsilon = k_B T$  as the parameters of the truncated and shifted Lennard-Jones potential.

### 5.3 Results: Comparison RPY with MPC

In Fig. 5.2, we show the comparison of the mean square end-to-end distances obtained for the self-propelled polymers in a MPC solvent with the simulation results applying the RPY tensor.

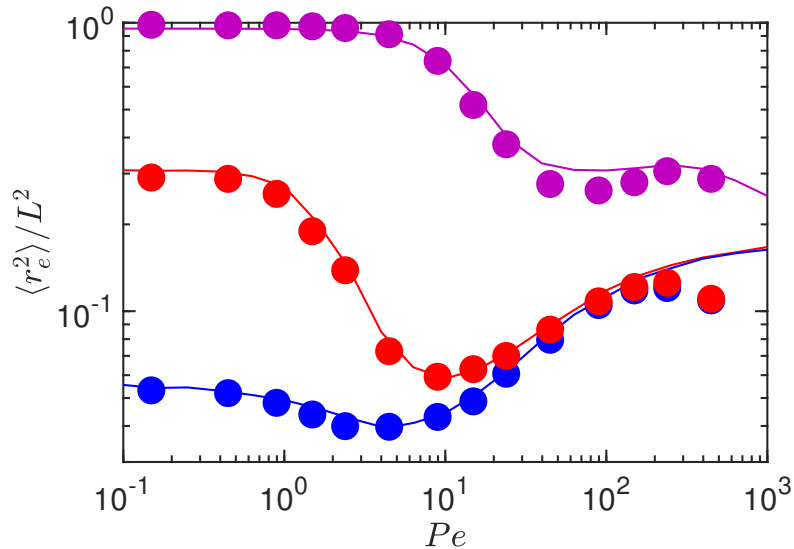


Fig. 5.2 Polymer mean square end-to-end distance as a function of the Péclet number of semiflexible polymers with  $N_m = 50$  ( $L = 49l$ ) monomers for  $pL = 5 \times 10^1$  (blue),  $2.6$  (red), and  $2.5 \times 10^{-2}$  (purple). Solid lines are results applying the RPY tensor and bullets are results of hybrid simulations using the MPC approach.

## Multiparticle collision dynamics approach with self-propelled polymers

---

Comparing the polymer mean square end-to-end distance obtained from the MPC approach with the results derived from the RPY tensor simulations, we find quantitative and qualitative agreement, validating the proper implementation of both approaches. Similarly to the case for active polymers by external colored noise in MPC (cf. Fig. 4.3), the deviations from the RPY tensor simulations also appear for  $Pe \gtrsim 10^2$ , due to limitations from the fluid model in terms of Mach and Reynolds numbers. Nonetheless, we want to stress the advantage of using the MPC approach compared to RPY tensor approach. Namely, it allows to treat more sophisticated problems where no tensor can easily be obtained such as active objects in confinement, or in complex geometries. Here, MPC can provide the correct hydrodynamic behavior.

# Chapter 6

## Conclusions and outlook

Analytical results for active semiflexible polymers under shear flow have been presented. The Gaussian semiflexible polymer model is adopted, which takes into account the polymer inextensibility in a mean-field manner by a constraint for the contour length [89, 90, 130]. Activity is modeled as a colored noise force with an exponential temporal correlation. The linearity of the equation of motion, even in the presence of shear flow, allows for its analytical solution. Relaxation times, deformation, alignment, and viscosity as a function of shear rate have been calculated. Each of these quantities shows a strong dependence on shear rate. Thereby, activity affects the shear response. An important aspect of a polymer in shear flow is its stretching and alignment along the flow direction, and its shrinkage transverse to it [142, 144, 150]. Activity enhances these aspects for flexible polymers. Semiflexible polymers show a nonmonotonic deformation behavior as a result of an activity-induced shrinkage at moderate Péclet numbers and a swelling at larger  $Pe$ , where the latter is similar to that of flexible polymers at the same  $Pe$  [74]. The activity-induced preference in alignment leads to a more pronounced shear thinning of highly active polymers, i.e., activity enhances shear thinning. All polymers exhibit the same shear-rate dependence in the limit  $Pe \rightarrow \infty$ , and, consequently, a universal behavior is obtained.

In addition, we analyzed how the active polymer relaxation behavior is governed by two processes, namely the diffusive dynamics of the active velocity, characterized by  $\gamma_R$ , and the relaxation times of the polymer. Following this direction, remains to be analyzed how these competing processes determine the overall relaxation dynamics, e.g., of the end-to-end vector, and diffusion of the ABPO in the presence of shear flow.

We have presented analytical, numerical, and computer simulation results for the conformational and dynamical properties of active semiflexible polymers in the presence of hydrodynamic interactions. In the simulations, the overdamped dynamics of a bead-spring polymer composed of ABP monomers is studied, with hydrodynamic interactions captured by the Rotne-Prager-Yamakawa hydrodynamic tensor. For the analytical treatment, the Gaussian semiflexible polymer model is adopted, which takes into account the polymer inextensibility in a mean-field manner by a constraint for the contour length. Here, activity is modeled as

## Conclusions and outlook

---

a Gaussian colored noise process with an exponential temporal correlation. Hydrodynamic interactions are taken into account by the preaveraged Oseen tensor. The linearity of the equation of motion allows for its analytical solution. In any case, our active forces do not generate a Stokeslet, higher-order active multipole flow fields, which decay spatial as  $1/r^2$  or faster with distance from the self-propelled active site, are neglected, and only the presumably dominant Stokeslet field resulting from intramolecular forces are taken into account.

Most remarkably, we find a strong influence of hydrodynamics on the polymer conformational properties. In absence of hydrodynamics, active flexible polymers (ABPOs-HI), with  $pL > 10$ , monotonically swell with increasing activity,  $Pe$ , whereas semiflexible polymers, with  $pL < 10$ , shrink at moderate  $Pe$  (the actual  $Pe$ -range depends on the polymer length) and swell for higher  $Pe$ , similar to flexible polymers [74, 76]. In contrast, active polymers in the presence of hydrodynamic interactions (ABPOs+HI) always shrink for moderate  $Pe$  independent of stiffness, and swell again for high activities, where the asymptotic extension for  $Pe \rightarrow \infty$  of an ABPO+HI is significantly smaller than that of an ABPO-HI. The observed strong influence of hydrodynamics appears over a Péclet-number range well covered by synthetic active colloids, where typically  $Pe \lesssim 150$ . [2]

Our studies predict a substantial effect of hydrodynamic interactions on the properties of active polymers. The shrinkage, even in the presence of excluded-volume interactions, results in an enhanced packing, which might be important for DNA organization within the cell nucleus [160, 161]. The actual mechanism of DNA packing is unresolved so far, however, DNA transcription or other local enzymatic processes, e.g., active-loop extrusion [162], provide a continuous local energy influx, and, hence, a source of nonthermal active noise. Moreover, hydrodynamic interactions could be involved in the observed subdiffusive dynamics of chromosomal loci [43, 163], which is typically related to a viscoelastic [94] or a fractal environment [164]. Further experimental studies are necessary to resolve the relevance of the various possible mechanisms affecting the dynamics, such as hydrodynamics, confinement, and viscoelasticity.

We have studied the conformational and dynamical properties of flexible and semiflexible polymers in presence of an external active bath and hydrodynamic interactions by simulations and analytical theory. In the simulations, we consider the overdamped dynamics of a bead-spring polymer, including hydrodynamic interactions via the Rotne–Prager–Yamakawa hydrodynamic tensor. Moreover, we present an implementation of the active polymer in the multiparticle collision dynamics approach. Comparison of the polymer conformational properties at various Péclet numbers and polymer stiffness yields quantitative agreement between simulations employing the hydrodynamic tensor and the MPC method, respectively. The MPC approach opens possibilities to study active polymers in situations, where a tensor description is extremely difficult and demanding, as for polymers confined in channels. In the analytical treatment, the Gaussian semiflexible polymer model is adopted, taking into account the polymer inextensibility in a mean-field manner by a constraint for the contour length. Here, hydrodynamic interactions are taken into account by the preaveraged Oseen tensor. In any case, activity is modeled as a Gaussian colored noise process with an expo-

---

nenial temporal correlation. This activity is assumed to be imposed externally onto the monomers by interactions with their environment. As a consequence, the active force gives rise to a Stokeslet flow field, in contrast to self-propelled monomers which are force free [116].

Our studies reveal a strong effect of hydrodynamics on both conformations and dynamics. Hydrodynamic interactions lead to a swelling of flexible externally driven active polymers, in contrast to flexible active polymers with self-propelled monomers (ABPO+HI) which show shrinkage over a range of moderate Péclet numbers. In addition, the externally driven active polymers reach a larger asymptotic plateau value for the mean square end-to-end distance for  $Pe \rightarrow \text{inf}$  than an ABPO+HI, which are typically more compact.

Similar as for the polymer dynamics of ABPO+HI, at short times,  $t/\tilde{\tau}_1$ ,  $\gamma_R \ll 1$ , activity leads to a ballistic regime, with an enhanced dynamics compared to a passive system. For intermediate time regimes,  $t/t/\tilde{\tau}_1 \ll 1 \ll \gamma_R t$ , in which activity and polymer properties govern the dynamics of the polymer, a subdiffusive regime  $\sim t^{5/7}$  (or  $3/4$  with the numerical results), a higher exponent than the  $2/3$  from the Zimm model and the  $1/2$  for Rouse polymers. For the limit  $t \rightarrow \text{inf}$ , the center-of-mass of the polymer controls the dynamics of the system, which leads to a diffusive regime ( $\sim t$ ) for all Péclet numbers with the diffusion coefficient of Eq. (4.49).

Further experimental investigations in the matter are essential to understand the interplay between hydrodynamics, out-of-equilibrium fluctuations, polymer conformations, and emerging activity-driven self-organized structures. Luckily, further studies and experiments of molecular/polymeric active matter will reveal original physical phenomena. Moreover, thinking about future application based on the properties of these systems, valuable design guidelines for tasks in the microscopic level such as directed transport and controlling assembly pathways of dissipative materials and structures can be provided. Such a fundamental understanding, opens a world of possibilities for creating soft functional materials that could implement responses impossible to reproduce with passive materials.



# Appendix A

## Intermolecular distance

Figure A.1(a) displays the mean square distance  $a^2(s, s')$  (Eq. (4.33)). It increases nonlinearly with the separation  $|s - s'|$ . There is a quantitative difference between the exact expression (4.33) and the approximation (4.35), but the later captures the essence of the distance and Péclet-number dependence. The difference between the two expressions vanishes for  $Pe \rightarrow 0$  and is small for  $Pe \gg 1$ , as illustrated in Fig. A.1(b). There,  $\Delta a^2$  is the ratio of the magnitude of the difference between  $a^2$  determined via Eq. (4.33) and (4.35), respectively, divided by the expression Eq. (4.33). Within the applied simplified theoretical approach, the quantitative agreement between the  $a^2(s, s')$  of Eq. (4.33) and (4.35) suffices and justifies the use of Eq. (4.35).

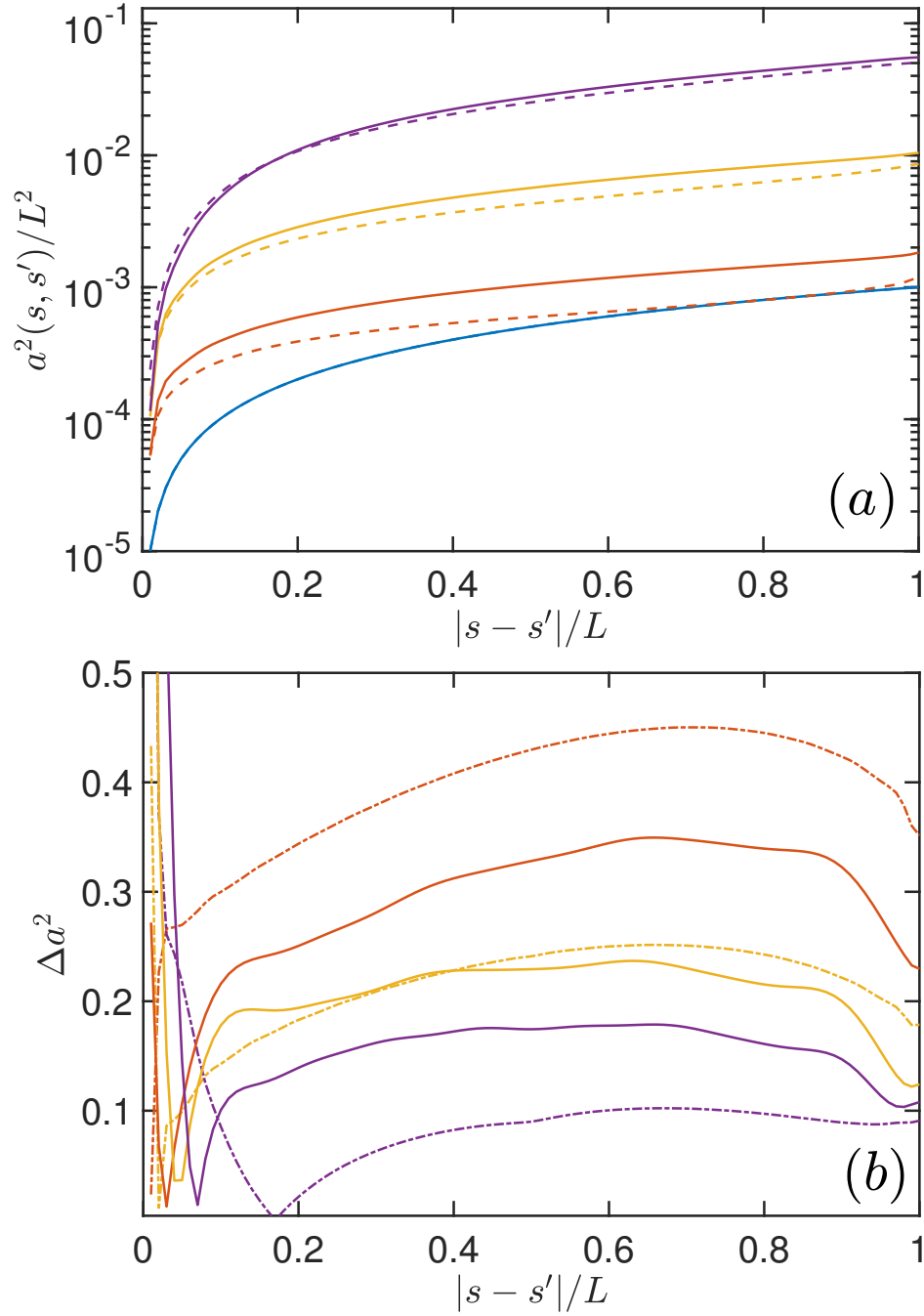


Fig. A.1 (a) Mean square distance between two points along the polymer contour as a function of their separation for  $pL = 10^2$  and the Péclet numbers  $Pe = 10^{-2}$  (blue),  $2 \times 10^1$  (orange),  $1.5 \times 10^2$  (yellow), and  $10^3$  (purple). The solid line is obtained by Eq. (4.33) and the dashed line by the approximation (4.35). In the valuation of Eq. (4.33),  $s' = -L/2$ . (b) Ratio  $\Delta a^2$  of the magnitude of the difference between  $a^2$  determined via Eq. (4.33) and (4.35) divided by the expression Eq. (4.33) for  $pL = 2 \times 10^2$  (solid) and  $pL = 5 \times 10^1$  (dashed-dotted). The colors correspond to the same Péclet numbers as in (a).

## Appendix B

# Mode-number dependence of Oseen tensor

The mode-number dependence of the Oseen tensor  $\Omega_{nn}$  (4.37), with the approximation (4.35) for  $a^2(s)$ , is illustrated in Fig. B.1 for various Péclet numbers and  $pL = 10^3$  and  $10^5$ . In the limit  $Pe \rightarrow 0$ , our approach is equivalent with the Zimm model for  $pL \rightarrow \infty$ , and we correspondingly find  $\Omega_{nn} \sim 1/\sqrt{n}$  [120, 132, 156]. The Oseen tensor  $\Omega_{nn}$  drops abruptly

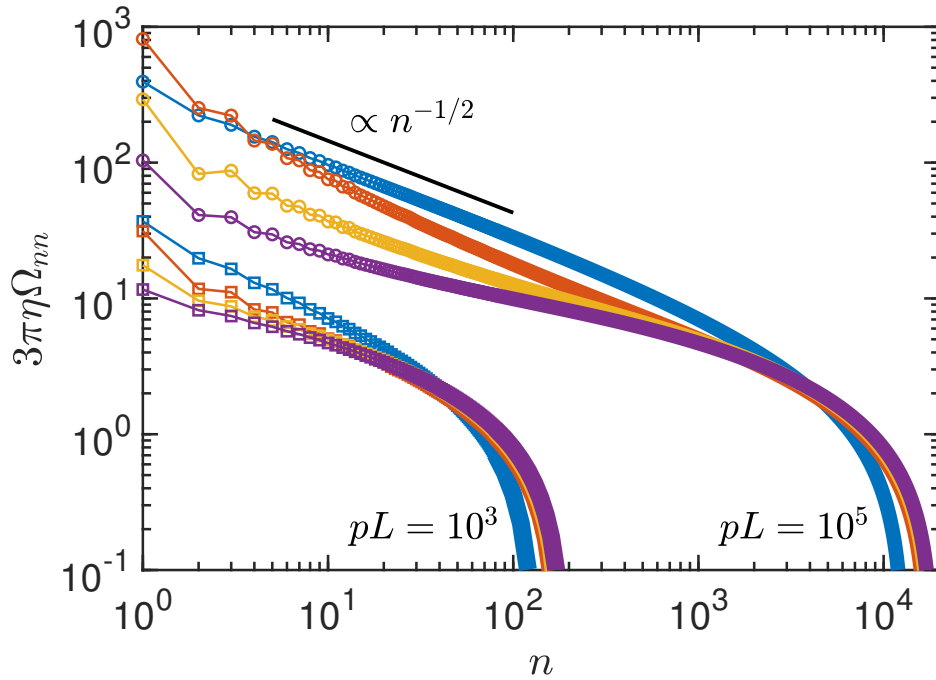


Fig. B.1 Mode-number dependence of the Oseen tensor  $\Omega_{nn}$  (Eq. (4.37)) for polymers of length  $pL = 10^5$  (circles) and  $pL = 10^3$  (squares) and the Péclet numbers  $Pe = 10^{-2}$  (blue),  $2 \times 10^1$  (orange),  $1.5 \times 10^2$  (yellow), and  $10^3$  (purple). The black line indicates the power law  $\Omega_{nn} \sim 1/\sqrt{n}$ .

## Mode-number dependence of Ossen tensor

---

below unity above a length-dependent mode number  $n_m$ , where  $\zeta_{n_m}/p = n_m\pi/pL \lesssim 1$ . Hence, the hydrodynamic contribution  $1 + 3\pi\eta\Omega_{nn}$  becomes irrelevant for modes  $n \gtrsim n_m$  and the relaxation times are equal to those of an ABPO-HI.

Activity changes the mode-number dependence of  $\Omega_{nn}$  in a non-monotonic manner, and the values of  $\Omega_{11}$  at nonzero  $Pe$  can be larger than those of the passive polymer. However, with increasing  $Pe$ ,  $\Omega_{11}$  is reduced and also  $\Omega_{nn}$  decrease more slowly with increasing  $n$  compared to the passive polymer. Together, this leads to a weaker dependence of the polymer dynamics on hydrodynamics with increasing activity. The length-dependence of  $\Omega_{nn}$  at small mode numbers is roughly given by Eq. (3.34). Moreover, also the Péclet-number dependence is approximately captured by Eq. (3.34) for  $pL = 10^5$  and  $Pe \gtrsim 10$ .

# Appendix C

## Relaxation times

Figure C.1 presents the mode-number dependence of the relaxation times  $\tilde{\tau}_n$  (3.36). The passive polymer exhibits the Zimm behavior  $\tilde{\tau}_n \sim n^{-3/2}$ . A similar power law is obtained for higher Péclet numbers over a more or less wide range of mode numbers. However, at higher  $Pe$ , a faster drop is obtained due to the slower decay of  $\Omega_{nn}$  with increasing mode number.

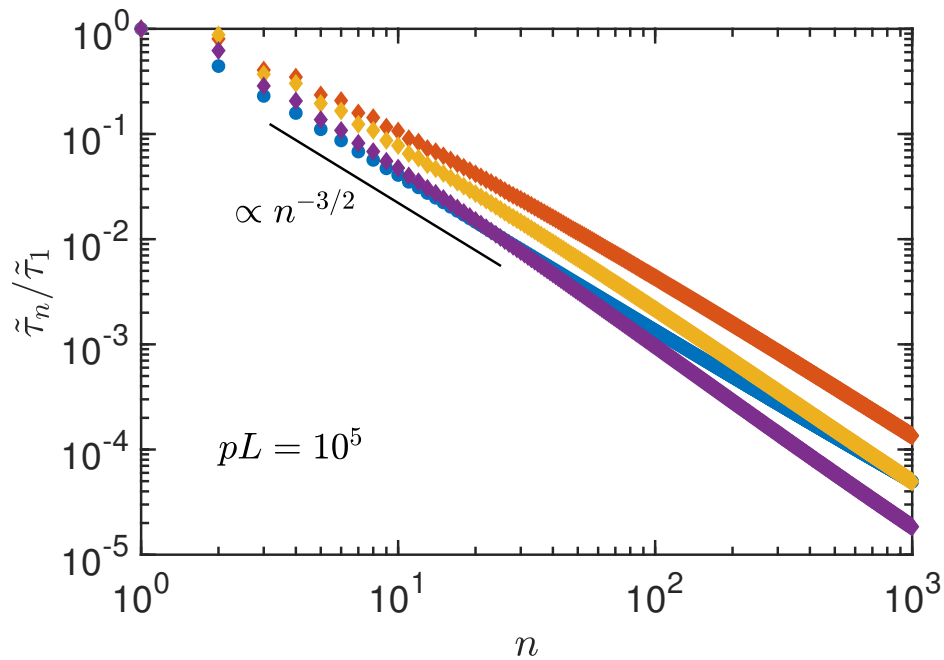


Fig. C.1 Mode-number dependence of the relaxation times  $\tilde{\tau}_n$  for a flexible polymer with  $pL = 10^5$  and the Péclet numbers  $Pe = 10^{-2}$  (blue),  $2 \times 10^1$  (orange),  $1.5 \times 10^2$  (yellow), and  $10^3$  (purple).  $\tilde{\tau}_1$  is the longest relaxation time. The black line indicates the power law  $\tilde{\tau}_n \sim n^{-3/2}$ .



# Appendix D

## Asymptotic stretching coefficient

The active contribution in the Eq. (4.40) can be written as

$$\sum_{i=1}^{\infty} \frac{v_0^2 l \tau_n^2}{1 + \gamma_R \tilde{\tau}_n} \zeta_n^2 = \frac{Pe^2 pL^2}{9\mu^2 \Delta^2 \pi^2} \quad (D.1)$$
$$\times \sum_{i=1}^{\infty} \left[ n^2 + \frac{2(pL)^2}{3\mu\Delta\pi^2(1 + 3\pi\eta\Omega_{nn})} \right]^{-1},$$

when we set  $d_H \equiv l$ . The stretching coefficient,  $\mu$ , increasing with increasing  $Pe$ . Hence, for  $(pL)^2 \ll \mu$ , the second term in the brackets can be neglected. Then, we obtain from Eq. (4.40)

$$\mu = \sqrt{\frac{pL}{6}} \frac{Pe}{3\Delta}. \quad (D.2)$$

In the opposite limit,  $pL \gg Pe$ , the sum over  $n$  is dominated by the second term in the bracket for small  $n$ , and the mode-number dependence is determined by the preaveraged Oseen tensor. With increasing Péclet number, higher modes become important, at the same time  $\Omega_{nn}$  becomes less relevant. Neglecting the hydrodynamic contribution, the sum over modes can be evaluated, and Eq. (4.40) yields [74]

$$\mu = \frac{Pe^{4/3}}{6\Delta}. \quad (D.3)$$



# Bibliography

- [1] J. Elgeti, R. G. Winkler, and G. Gompper, Rep. Prog. Phys. **78**, 056601 (2015).
- [2] C. Bechinger, R. Di Leonardo, H. Löwen, C. Reichhardt, G. Volpe, and G. Volpe, Rev. Mod. Phys. **88**, 045006 (2016).
- [3] E. Lauga and T. R. Powers, Rep. Prog. Phys. **72**, 096601 (2009).
- [4] S. Ramaswamy, Annu. Rev. Cond. Mat. Phys. **1**, 323 (2010).
- [5] T. Vicsek and A. Zafeiris, Phys. Rep. **517**, 71 (2012).
- [6] P. Romanczuk, M. Bär, W. Ebeling, B. Lindner, and L. Schimansky-Geier, Eur. Phys. J. Spec. Top. **202**, 1 (2012).
- [7] M. C. Marchetti, J. F. Joanny, S. Ramaswamy, T. B. Liverpool, J. Prost, M. Rao, and R. A. Simha, Rev. Mod. Phys. **85**, 1143 (2013).
- [8] M. C. Marchetti, Y. Fily, S. Henkes, A. Patch, and D. Yllanes, Curr. Opin. Colloid Interface Sci. **21**, 34 (2016).
- [9] A. Zöttl and H. Stark, J. Phys.: Condens. Matter **28**, 253001 (2016).
- [10] R. G. Winkler, J. Elgeti, and G. Gompper, J. Phys. Soc. Jpn. **86**, 101014 (2017).
- [11] O. Duman, R. E. Isele-Holder, J. Elgeti, and G. Gompper, Soft Matter **14**, 4483 (2018).
- [12] H. S. Muddana, S. Sengupta, T. E. Mallouk, A. Sen, and P. J. Butler, J. Am. Chem. Soc. **132**, 2110 (2010).
- [13] K. K. Dey, S. Das, M. F. Poyton, S. Sengupta, P. J. Butler, P. S. Cremer, and A. Sen, ACS Nano **8**, 11941 (2014).
- [14] F. J. Nédélec, T. Surrey, A. C. Maggs, and S. Leibler, Nature **389**, 305 (1997).
- [15] J. Howard, *Mechanics of motor proteins and the cytoskeleton* (Sinauer Associates Sunderland, MA, 2001).
- [16] K. Kruse, J. F. Joanny, F. Jülicher, J. Prost, and K. Sekimoto, Phys. Rev. Lett. **92**, 078101 (2004).
- [17] A. R. Bausch and K. Kroy, Nat. Phys. **2**, 231 (2006).
- [18] F. Jülicher, K. Kruse, J. Prost, and J.-F. Joanny, Phys. Rep. **449**, 3 (2007).

## Bibliography

---

- [19] Y. Harada, A. Noguchi, A. Kishino, and T. Yanagida, *Nature* **326**, 805 (1987).
- [20] V. Schaller, C. Weber, C. Semmrich, E. Frey, and A. R. Bausch, *Nature* **467**, 73 (2010).
- [21] J. Prost, F. Jülicher, and J.-F. Joanny, *Nat. Phys.* **11**, 111 (2015).
- [22] H. C. Berg, *E. Coli in Motion*, Biological and Medical Physics Series (Springer, New York, 2004).
- [23] J. S. Guasto, R. Rusconi, and R. Stocker, *Ann. Rev. Fluid Mech.* **44**, 373 (2011).
- [24] R. G. Winkler and G. Gompper, *Hydrodynamics in Motile Active Matter* (Springer International Publishing, Cham, 2018).
- [25] G. Saggiorato, L. Alvarez, J. F. Jikeli, U. B. Kaupp, G. Gompper, and J. Elgeti, *Nat. Commun.* **8**, 1415 (2017).
- [26] S. Rode, J. Elgeti, and G. Gompper, *New J. Phys.* **21**, 013016 (2019).
- [27] T. Ishikawa and M. Hota, *J. Exp. Biol.* **209**, 4452 (2006).
- [28] N. Watari and R. G. Larson, *Biophys. J.* **98**, 12 (2010).
- [29] N. C. Darnton, L. Turner, S. Rojevsky, and H. C. Berg, *Biophys. J.* **98**, 2082 (2010).
- [30] A. Cordoba, J. D. Schieber, and T. Indei, *RSC Adv.* **4**, 17935 (2014).
- [31] S. C. Weber, A. J. Spakowitz, and J. A. Theriot, *Proc. Natl. Acad. Sci. USA* **109**, 7338 (2012).
- [32] E. Selander, H. H. Jakobsen, F. Lombard, and T. Kiørboe, *Proc. Natl. Acad. Sci. USA* **108**, 4030 (2011).
- [33] M. H. Sohn, K. W. Seo, Y. S. Choi, S. J. Lee, Y. S. Kang, and Y. S. Kang, *Mar. Biol. Biology* **158**, 561 (2011).
- [34] M. F. Copeland and D. B. Weibel, *Soft Matter* **5**, 1174 (2009).
- [35] S. Ganguly, L. S. Williams, I. M. Palacios, and R. E. Goldstein, *Proc. Natl. Acad. Sci. USA* **109**, 15109 (2012).
- [36] M. E. Cates and F. C. MacKintosh, *Soft Matter* **7**, 3050 (2011).
- [37] D. Needleman and Z. Dogic, *Nat. Rev. Mater.* **2**, 201748 (2017).
- [38] A. J. Ridley, M. A. Schwartz, K. Burridge, R. A. Firtel, M. H. Ginsberg, G. Borisy, J. T. Parsons, and A. R. Horwitz, *Science* **302**, 1704 (2003).
- [39] Y. Sumino, K. H. Nagai, Y. Shitaka, D. Tanaka, K. Yoshikawa, H. Chate, and K. Oiwa, *Nature* **483**, 448 (2012).
- [40] A. Doostmohammadi, T. N. Shendruk, K. Thijssen, and J. M. Yeomans, *Nat. Commun.* **8**, 15326 (2017).
- [41] C. P. Brangwynne, G. H. Koenderink, F. C. MacKintosh, and D. A. Weitz, *Phys. Rev. Lett.* **100**, 118104 (2008).

- 
- [42] C. A. Weber, R. Suzuki, V. Schaller, I. S. Aranson, A. R. Bausch, and E. Frey, *Proc. Natl. Acad. Sci. USA* **112**, 10703 (2015).
- [43] A. Javer, Z. Long, E. Nugent, M. Grisi, K. Siritwatwetchakul, K. D. Dorfman, P. Cicuta, and M. Cosentino Lagomarsino, *Nat. Commun.* **4**, 3003 (2013).
- [44] A. Zidovska, D. A. Weitz, and T. J. Mitchison, *Proc. Natl. Acad. Sci. USA* **110**, 15555 (2013).
- [45] J. R. Howse, R. A. L. Jones, A. J. Ryan, T. Gough, R. Vafabakhsh, and R. Golestanian, *Phys. Rev. Lett.* **99**, 048102 (2007).
- [46] G. Volpe, I. Buttinoni, D. Vogt, H. J. Kümmerer, and C. Bechinger, *Soft Matter* **7**, 8810 (2011).
- [47] S. Thutupalli, R. Seemann, and S. Herminghaus, *New J. Phys.* **13**, 073021 (2011).
- [48] I. Buttinoni, J. Bialké, F. Kümmel, H. Löwen, C. Bechinger, and T. Speck, *Phys. Rev. Lett.* **110**, 238301 (2013).
- [49] B. ten Hagen, F. Kümmel, R. Wittkowski, D. Takagi, H. Löwen, and C. Bechinger, *Nat. Commun.* **5**, 4829 (2014).
- [50] C. C. Maass, C. Krüger, S. Herminghaus, and C. Bahr, *Annu. Rev. Cond. Mat. Phys.* **7**, 171 (2016).
- [51] H. C. Andersen, *J. Chem. Phys.* **72**, 2384 (1980).
- [52] F. Guzmán-Lastra, A. Kaiser, and H. Löwen, *Nature Communications* **7**, 13519 EP (2016).
- [53] R. Dreyfus, J. Baudry, M. L. Roper, M. Fermigier, H. A. Stone, and J. Bibette, *Nature* **437**, 862 (2005).
- [54] H. Löwen, *EPL* **121**, 58001 (2018).
- [55] J. Yan, M. Han, J. Zhang, C. Xu, E. Luijten, and S. Granick, *Nat. Mat.* **15**, 1095 (2016).
- [56] R. Di Leonardo, *Nat. Mat.* **15**, 1057 (2016).
- [57] D. Nishiguchi, J. Iwasawa, H.-R. Jiang, and M. Sano, *New J. Phys.* **20**, 015002 (2018).
- [58] Y. Sasaki, Y. Takikawa, V. S. R. Jampani, H. Hoshikawa, T. Seto, C. Bahr, S. Herminghaus, Y. Hidaka, and H. Orihara, *Soft Matter* **10**, 8813 (2014).
- [59] B. Biswas, R. K. Manna, A. Laskar, P. B. S. Kumar, R. Adhikari, and G. Kumaraswamy, *ACS Nano* **11**, 10025 (2017).
- [60] R. Chelakkot, A. Gopinath, L. Mahadevan, and M. F. Hagan, *J. R. Soc. Interf.* **11**, 20130884 (2014).
- [61] H. Jiang and Z. Hou, *Soft Matter* **10**, 1012 (2014).
- [62] H. Jiang and Z. Hou, *Soft Matter* **10**, 9248 (2014).

## Bibliography

---

- [63] R. E. Isele-Holder, J. Elgeti, and G. Gompper, *Soft Matter* **11**, 7181 (2015).
- [64] K. R. Prathyusha, S. Henkes, and R. Sknepnek, *Phys. Rev. E* **97**, 022606 (2018).
- [65] V. Bianco, E. Locatelli, and P. Maggaretti, *Phys. Rev. Lett.* **121**, 217802 (2018).
- [66] D. Loi, S. Mossa, and L. F. Cugliandolo, *Soft Matter* **7**, 10193 (2011).
- [67] A. Kaiser and H. Löwen, *J. Chem. Phys.* **141**, 044903 (2014).
- [68] J. Harder, C. Valeriani, and A. Cacciuto, *Phys. Rev. E* **90**, 062312 (2014).
- [69] A. Ghosh and N. S. Gov, *Biophys. J.* **107**, 1065 (2014).
- [70] D. Sarkar, S. Thakur, Y.-G. Tao, and R. Kapral, *Soft Matter* **10**, 9577 (2014).
- [71] J. Shin, A. G. Cherstvy, W. K. Kim, and R. Metzler, *New J. Phys.* **17**, 113008 (2015).
- [72] A. Kaiser, S. Babel, B. ten Hagen, C. von Ferber, and H. Löwen, *J. Chem. Phys.* **142**, 124905 (2015).
- [73] N. Samanta and R. Chakrabarti, *J. Phys. A: Math. Theor.* **49**, 195601 (2016).
- [74] T. Eisenstecken, G. Gompper, and R. G. Winkler, *Polymers* **8**, 304 (2016).
- [75] D. Osmanovic and Y. Rabin, *Soft Matter* **13**, 963 (2017).
- [76] T. Eisenstecken, G. Gompper, and R. G. Winkler, *J. Chem. Phys.* **146**, 154903 (2017).
- [77] A. Martín-Gómez, G. Gompper, and R. G. Winkler, *Polymers* **10**, 837 (2018).
- [78] G. Jayaraman, S. Ramachandran, S. Ghose, A. Laskar, M. S. Bhamla, P. B. S. Kumar, and R. Adhikari, *Phys. Rev. Lett.* **109**, 158302 (2012).
- [79] A. Laskar and R. Adhikari, *Soft Matter* **11**, 9073 (2015).
- [80] A. Pandey, P. B. Sunil Kumar, and R. Adhikari, *Soft Matter* **12**, 9068 (2016).
- [81] T. C. Adhyapak and H. Stark, *Phys. Rev. E* **92**, 052701 (2015).
- [82] I. O. Götze and G. Gompper, *Phys. Rev. E* **82**, 041921 (2010).
- [83] I. Llopis and I. Pagonabarraga, *J. Non-Newtonian Fluid Mech.* **165**, 946 (2010).
- [84] J. M. Yeomans, D. O. Pushkin, and H. Shum, *Eur. Phys. J. Spec. Top.* **223**, 1771 (2014).
- [85] M. Theers, E. Westphal, G. Gompper, and R. G. Winkler, *Soft Matter* **12**, 7372 (2016).
- [86] R. G. Winkler, *Soft Matter* **12**, 3737 (2016).
- [87] R. G. Winkler and P. Reineker, *Macromolecules* **25**, 6891 (1992).
- [88] L. Harnau, R. G. Winkler, and P. Reineker, *J. Chem. Phys.* **102**, 7750 (1995).
- [89] R. G. Winkler, P. Reineker, and L. Harnau, *J. Chem. Phys.* **101**, 8119 (1994).

- 
- [90] R. G. Winkler, *J. Chem. Phys.* **118**, 2919 (2003).
- [91] R. G. Winkler, *J. Chem. Phys.* **127**, 054904 (2007).
- [92] R. G. Winkler, *Phys. Rev. Lett.* **97**, 128301 (2006).
- [93] R. G. Winkler, L. Harnau, and P. Reineker, *Macromol. Theory Simul.* **6**, 1007 (1997).
- [94] H. Vandebroek and C. Vanderzande, *Phys. Rev. E* **92**, 060601 (2015).
- [95] H. Risken, *The Fokker-Planck Equation* (Springer, Berlin, 1989).
- [96] C. W. Gardener, *Handbook of Stochastic Methods* (Springer, Berlin, 1983).
- [97] R. Kubo, *Rep. Prog. Phys.* **29**, 255 (1966).
- [98] G. K. Batchelor, *An Introduction to Fluid Mechanics* (Cambridge University Press, Cambridge, 1990).
- [99] J. H. Irving and J. G. Kirkwood, *J. Chem. Phys.* **18**, 817 (1950).
- [100] S. Kim and S. J. Karrila, *Microhydrodynamics: principles and selected applications* (Butterworth-Heinemann, Boston, 1991), ISBN 0486317676.
- [101] D. L. Ermak and J. McCammon, *J. Chem. Phys.* **69**, 1352 (1978).
- [102] M. P. Allen and D. J. Tildesley, *Computer Simulation of Liquids* (Clarendon Press, Oxford, 1987).
- [103] J. Platzer, W. Sterr, M. Hausmann, and R. Schmitt, *J. Bacteriol.* **179**, 6391 (1997).
- [104] A. Malevanets and R. Kapral, *J. Chem. Phys.* **110**, 8605 (1999).
- [105] A. Malevanets and J. M. Yeomans, *Europhys. Lett.* **52**, 231 (2000).
- [106] T. Ihle, *Phys. Chem. Chem. Phys.* **11**, 9667 (2009).
- [107] T. Ihle and D. M. Kroll, *Phys. Rev. E* **67**, 066705 (2003).
- [108] R. G. Winkler, M. O. Steinhauser, and P. Reineker, *Phys. Rev. E* **66**, 021802 (2002).
- [109] R. G. Winkler, K. Mussawisade, M. Ripoll, and G. Gompper, *J. Phys.: Condens. Matter* **16**, S3941 (2004).
- [110] M. Ripoll, K. Mussawisade, R. G. Winkler, and G. Gompper, *Europhys. Lett.* **68**, 106 (2004).
- [111] M. Ripoll, K. Mussawisade, R. G. Winkler, and G. Gompper, *Phys. Rev. E* **72**, 016701 (2005).
- [112] E. Westphal, S. P. Singh, C.-C. Huang, G. Gompper, and R. G. Winkler, *Comput. Phys. Comm.* **185**, 495 (2014).
- [113] K. Mussawisade, M. Ripoll, R. G. Winkler, and G. Gompper, *J. Chem. Phys.* **123**, 144905 (2005).

## Bibliography

---

- [114] C.-C. Huang, A. Chatterji, G. Sutmann, G. Gompper, and R. G. Winkler, *J. Comput. Phys.* **229**, 168 (2010).
- [115] C.-C. Huang, G. Sutmann, G. Gompper, and R. G. Winkler, *EPL* **93**, 54004 (2011).
- [116] A. Martín-Gómez, T. Eisenstecken, G. Gompper, and R. G. Winkler, *Soft Matter* pp. – (2019).
- [117] T. Eisenstecken, A. Ghavami, A. Mair, G. Gompper, and R. G. Winkler, *AIP Conf. Proc.* **1871**, 050001 (2017).
- [118] A. Wysocki, R. G. Winkler, and G. Gompper, *EPL* **105**, 48004 (2014).
- [119] W. Ebeling, F. Schweitzer, and B. Tilch, *Biosystems* **49**, 17 (1999).
- [120] L. Harnau, R. G. Winkler, and P. Reineker, *J. Chem. Phys.* **104**, 6355 (1996).
- [121] S. M. Mousavi, G. Gompper, and R. G. Winkler, *J. Chem. Phys.* **150**, 064913 (2019).
- [122] R. G. Winkler, A. Wysocki, and G. Gompper, *Soft Matter* **11**, 6680 (2015).
- [123] É. Fodor, C. Nardini, M. E. Cates, J. Tailleur, P. Visco, and F. van Wijland, *Phys. Rev. Lett.* **117**, 038103 (2016).
- [124] A. Jain, P. Sunthar, B. Dünweg, and J. R. Prakash, *Phys. Rev. E* **85**, 066703 (2012).
- [125] S. Das, G. Gompper, and R. G. Winkler, *New J. Phys.* **20**, 015001 (2018).
- [126] S. Das, G. Gompper, and R. G. Winkler, *Sci. Rep.*, submitted (2018).
- [127] M. G. Bawendi and K. F. Freed, *J. Chem. Phys.* **83**, 2491 (1985).
- [128] S. M. Battacharjee and M. Muthukumar, *J. Chem. Phys.* **86**, 411 (1987).
- [129] J. B. Langowski, J. Noolandi, and B. Nickel, *J. Chem. Phys.* **95**, 1266 (1991).
- [130] B. Y. Ha and D. Thirumalai, *J. Chem. Phys.* **103**, 9408 (1995).
- [131] E. P. Petrov, T. Ohrt, R. G. Winkler, and P. Schwille, *Phys. Rev. Lett.* **97**, 258101 (2006).
- [132] M. Doi and S. F. Edwards, *The Theory of Polymer Dynamics* (Clarendon Press, Oxford, 1986).
- [133] J. Bialké, T. Speck, and H. Löwen, *Phys. Rev. Lett.* **108**, 168301 (2012).
- [134] Y. Fily and M. C. Marchetti, *Phys. Rev. Lett.* **108**, 235702 (2012).
- [135] F. Peruani, L. Schimansky-Geier, and M. Bär, *Eur. Phys. J. Spec. Top.* **191**, 173 (2010).
- [136] G. S. Redner, M. F. Hagan, and A. Baskaran, *Phys. Rev. Lett.* **110**, 055701 (2013).
- [137] B. ten Hagen, R. Wittkowski, D. Takagi, F. Kümmel, C. Bechinger, and H. Löwen, *J. Phys.: Condens. Matter* **27**, 194110 (2015).
- [138] P. J. Flory, *Statistical Mechanics of Polymer Chains* (John Wiley & Sons, New York, 1989).

- 
- [139] M. Rubinstein and R. C. Colby, *Polymer Physics* (Oxford University Press, Oxford, 2003).
- [140] R. G. Winkler, S. Keller, and J. O. Rädler, *Phys. Rev. E* **73**, 041919 (2006).
- [141] P. E. Rouse, *J. Chem. Phys.* **21**, 1272 (1953).
- [142] R. G. Winkler, *J. Chem. Phys.* **133**, 164905 (2010).
- [143] T. B. Liverpool, A. C. Maggs, and A. Ajdari, *Phys. Rev. Lett.* **86**, 4171 (2001).
- [144] C.-C. Huang, R. G. Winkler, G. Sutmann, and G. Gompper, *Macromolecules* **43**, 10107 (2010).
- [145] R. B. Bird, R. C. Armstrong, and O. Hassager, *Dynamics of Polymer Liquids*, vol. 1 (John Wiley & Sons, New York, 1987).
- [146] C. M. Schroeder, R. E. Teixeira, E. S. G. Shaqfeh, and S. Chu, *Macromolecules* **38**, 1967 (2005).
- [147] A. V. Lyulin, D. B. Adolf, and G. R. Davies, *J. Chem. Phys.* **111**, 758 (1999).
- [148] R. M. Jendrejack, J. J. de Pablo, and M. D. Graham, *J. Chem. Phys.* **116**, 7752 (2002).
- [149] S. Liu, B. Ashok, and M. Muthukumar, *Polymer* **45**, 1383 (2004).
- [150] C. Aust, M. Kröger, and S. Hess, *Macromolecules* **32**, 5660 (1999).
- [151] H. Eslami and F. Müller-Plathe, *J. Phys. Chem. B* **114**, 387 (2010).
- [152] S. P. Singh, A. Chatterji, G. Gompper, and R. G. Winkler, *Macromolecules* **46**, 8026 (2013).
- [153] J. Rotne and S. Prager, *J. Chem. Phys.* **50**, 4831 (1969).
- [154] H. Yamakawa, *J. Chem. Phys.* **53**, 436 (1970).
- [155] J. K. G. Dhont, *An Introduction to Dynamics of Colloids* (Elsevier, Amsterdam, 1996).
- [156] B. H. Zimm, *J. Chem. Phys.* **24**, 269 (1956).
- [157] M. Hinczewski, X. Schlagberger, M. Rubinstein, O. Krichevsky, and R. R. Netz, *Macromolecules* **42**, 860 (2009).
- [158] M. Hinczewski and R. Netz, *EPL* **88**, 18001 (2009).
- [159] F. S. Gnesotto, F. Mura, J. Gladrow, and C. P. Broedersz, *Rep. Prog. Phys.* **81**, 066601 (2018).
- [160] J. Smrek and K. Kremer, *Phys. Rev. Lett.* **118**, 098002 (2017).
- [161] N. Ganai, S. Sengupta, and G. I. Menon, *Nucleic Acids Res.* **42**, 4145 (2014).
- [162] A. Goloborodko, J. F. Marko, and L. A. Mirny, *Biophys. J.* **110**, 2162 (2016).
- [163] S. C. Weber, A. J. Spakowitz, and J. A. Theriot, *Phys. Rev. Lett.* **104**, 238102 (2010).

## Bibliography

---

- [164] M. V. Tamm, L. I. Nazarov, A. A. Gavrilov, and A. V. Chertovich, *Phys. Rev. Lett.* **114**, 178102 (2015).
- [165] R. Kapral, *Adv. Chem. Phys.* **140**, 89 (2008).
- [166] G. Gompper, T. Ihle, D. M. Kroll, and R. G. Winkler, *Adv. Polym. Sci.* **221**, 1 (2009).
- [167] S. P. Singh, G. Gompper, and R. G. Winkler, *J. Chem. Phys.* **148**, 084901 (2018).
- [168] S. Poblete, A. Wysocki, G. Gompper, and R. G. Winkler, *Phys. Rev. E* **90**, 033314 (2014).
- [169] S. P. Singh, C.-C. Huang, E. Westphal, G. Gompper, and R. G. Winkler, *J. Chem. Phys.* **141**, 084901 (2014).
- [170] N. Grønbech-Jensen and O. Farago, *Mol. Phys.* **111**, 983 (2013).

# Erklärung

Ich versichere, daß ich die von mir vorgelegte Dissertation selbständig angefertigt, die benutzten Quellen und Hilfsmittel vollständig angegeben und die Stellen der Arbeit einschließlich Tabellen, Karten und Abbildungen, die anderen Werken im Wortlaut oder dem Sinn nach entnommen sind, in jedem Einzelfall als Entlehnung kenntlich gemacht habe; daß diese Dissertation noch keiner anderen Fakultät oder Universität zur Prüfung vorgelegen hat; daß sie abgesehen von unten angegebenen Teilpublikationen noch nicht veröffentlicht worden ist sowie, daß ich eine solche Veröffentlichung vor Abschluß des Promotionsverfahrens nicht vornehmen werde. Die Bestimmungen dieser Promotionsordnung sind mir bekannt. Die von mir vorgelegte Dissertation ist von Prof. Dr. Gerhard Gompper betreut worden.

Köln, 20 Januar 2020

Aitor Martin-Gomez

## Publikationen

*Characteristics of active polymers in solution by external colored noise*, A. Martin-Gomez, T. Eisenstecken, G. Gompper and R. G. Winkler, (2020)

*Active Brownian filaments with hydrodynamic interactions: conformations and dynamics*, A. Martin-Gomez, T. Eisenstecken, G. Gompper and R. G. Winkler, *Soft Matter*, **15**, 3957 (2019)

*Active brownian filamentous polymers under shear flow*, A. Martin-Gomez, G. Gompper, R. G. Winkler, *Polymers*, **8**, 304 (2018)

*Collective motion of active Brownian particles with polar alignment*, A. Martin-Gomez, D. Levis, A. Diaz-Guilera, I. Pagonabarraga, *Soft Matter*, **14**, 2610 (2018)



# CV

## Aitor Martin-Gomez

Eschenweg 15  
Jülich, 52428 Germany  
0034 684 03 76 99  
aitormg93@gmail.com

Born: May 31, 1993—Barcelona, Spain

### Education

**2009 – 2011** Preparation Years for University at Col·legi Sant Josep Obrer, L'Hospitalet de Llobregat

**2005 – 2009** High School at Col·legi Sant Josep Obrer, L'Hospitalet de Llobregat

### Academic Record

**2016 – 2020** Ph.D. student at Universität zu Köln and Forschungszentrum Jülich  
Advisors: Prof. Dr. Gerhard Gompper, Prof. Dr. Roland G. Winkler

**2015 – 2016** Master of Science in Computational Modeling for Physicists at University of Barcelona

**2011 – 2015** Bachelor of Science in Physics with major in Theoretical Physics at University of Barcelona